

UC Berkeley

UC Berkeley Electronic Theses and Dissertations

Title

TEM Investigation of Alignment, Morphology, Strain, and Rotation Phenomena in the Epitaxial Au-MoS₂ System: Process and Insights

Permalink

<https://escholarship.org/uc/item/72j6942j>

Author

Bhargava, Clarissa May

Publication Date

2021

Peer reviewed|Thesis/dissertation

TEM Investigation of Alignment, Morphology, Strain, and Rotation Phenomena in
the Epitaxial Au-MoS₂ System: Process and Insights

by

Clarissa May Bhargava

A dissertation submitted in partial satisfaction of the
requirements for the degree of

Doctor of Philosophy

in

Engineering – Materials Science and Engineering

in the

Graduate Division

of the

University of California, Berkeley

Committee in charge:

Professor Joel W. Ager, Co-Chair

Professor Oscar D. Dubon, Co-Chair

Professor Mary C. Scott

Professor Hayden K. Taylor

Fall 2021

© 2021
Clarissa May Bhargava
All Rights Reserved

Abstract

TEM Investigation of Alignment, Morphology, Strain, and Rotation Phenomena in
the Epitaxial Au-MoS₂ System: Process and Insights

by

Clarissa May Bhargava

Doctor of Philosophy in Materials Science and Engineering

University of California, Berkeley

Professor Joel W. Ager, Co-Chair / Professor Oscar D. Dubon, Co-Chair

MoS₂ is one of a class of layered, semiconducting materials known as the transition metal dichalcogenides (TMDCs). When a monolayer is isolated from the multilayer crystal, the electronic properties of the TMDC can undergo a dramatic shift. In MoS₂, the energy band gap changes from an indirect gap of 1.2 eV in the bulk to a direct gap of 1.8 eV in the monolayer. This intriguing feature has driven, in part, the recent surge in investigations into MoS₂ as a candidate for atomically thin electronic and photonic devices. The last fifteen years have seen an accelerating effort to exfoliate large, high-quality monolayers of MoS₂ and the other TMDCs, both from their natural crystalline forms and from lab-grown multilayers. The broader context of this dissertation is this effort to grow, exfoliate, characterize, and construct simple devices from MoS₂ and WS₂, including both natural and engineered bi-layers and heterostructures. Motivating the close study of Au on MoS₂, it is noted that significant advances in selective monolayer TMDC exfoliation were achieved utilizing a Au ‘handle’ layer and a compliant temporary ‘superstrate.’

The gold-assisted high-yield exfoliation of lithographically defined features motivates the study of the mechanical and structural relationship between Au layers and few-layer MoS₂. Using a 100-nm layer of deposited Au as a handle layer, large areas of monolayer MoS₂ are successfully exfoliated from a multilayer stack and characterized using photoluminescence spectroscopy and atomic force microscopy. STEM characterization identifies the preferred (111) rotational alignment of epitaxially grown Au on the (0001) basal plane of MoS₂. While Au nuclei that form on the surface of MoS₂ could be initially strained to form a coherent interface when they remain below a

critical size, in Au crystallites with an approximate thickness of 1-10 nm and a median diameter of 15 nm, the underlying MoS₂ substrate is not found to be strained when measured using nanobeam electron diffraction.

The deformation phenomena of the epitaxial Au-MoS₂ system, and approaches to elucidating them, are explored in this dissertation using transmission electron microscopy techniques, particularly, 4D Scanning Transmission Electron Microscopy (4D-STEM). 4D-STEM involves recording a grid of nanobeam electron diffraction (NBED) patterns over a two-dimensional sample area, and the result is a 2D array of 2D diffraction patterns, comprising a 4D dataset. MoS₂ diffraction patterns are compared to their corresponding patterns in a generated database of diffraction patterns simulated using the PRISM multislice algorithm. The thickness of deposited Au is approximated using high-angle annular dark field (HAADF) images of the Au-MoS₂ system. Using the Z-contrast mechanism of the HAADF images, the thickness of a nanoporous Au film is estimated to be between 1-10 nm, slightly lower than the intended mean thickness of 15 nm of Au calibrated during e-beam deposition using quartz crystal microbalancing (QCM). Accordingly, variations in Au thickness are discussed in the context of the e-beam evaporation of Au onto MoS₂. Finally, a workflow is outlined for examining the Moiré fringes and patterns in experimental HAADF images in order to identify rotational and lattice alignments.

These analyses reveal the dearth of measurable strains in the epitaxial Au-MoS₂ system, the presence of rippling in ultra-thin MoS₂ with an approximate radius of curvature of 50 nm, the self-avoiding growth morphology of thin-film Au, and the rotation of up to 3° between these materials. Data from nanobeam electron diffraction and dark-field STEM imaging show that gold typically grows on MoS₂(0001) with its [111] vector normal to the interface. However, symmetric axial rotations about this vector direction with typical magnitudes of 1-2° can occasionally arise in Au domains, which range from 5-15 nm in diameter. The use of evaporated Au as a compliant handle layer in TMDC exfoliation processes is confirmed to be empirically useful for increasing the size and selectivity of single layers. Exfoliated mono- and bi-layers produced using this method are evaluated using photoluminescence spectroscopy, and sulfur vacancies are repaired using a TFSI superacid treatment which improves the photoluminescence quantum yield by a factor of 25 and 100 for MoS₂ and WS₂, respectively. These results have implications for future architectures and processes for nanoelectronics based on monolayer TMDCs.

Contents

Acknowledgments	iv
List of Figures	vii
1 Introduction	1
1.1 Two-dimensional transition metal dichalcogenides	2
1.2 Prediction of strain and motivation for selective exfoliation	4
1.3 Thin film epitaxy: definitions, paradigms, and relevance	6
1.4 History of the relationship of Au grown on MoS ₂	6
1.5 Interfacial rotations in 2D materials and epitaxial metals	7
1.6 TEM methods for studying 2D materials	8
1.7 Diffraction: Reciprocal space	12
1.8 Chapter 1 Summary	17
2 4D Scanning Transmission Electron Microscopy	24
2.1 Introduction to 4D STEM	24
2.2 Instrumentation	26
2.2.1 The right electron detector is critical for 4D STEM	27
2.3 Data analysis and simulation	31
2.3.1 Pre-processing in Mathematica	31
2.3.2 py4DSTEM	32
2.3.3 Using Matlab to build a virtual crystal system and generate multislice STEM simulations	33
2.4 Open access database archive	35
2.5 Chapter 2 Summary	37
3 Detailed Methodology	40
3.1 Sample preparation	40
3.2 TEM Workflow: EDS, HAADF, 4D STEM	42
3.3 How to approximate MoS ₂ thickness using STEM	46
3.3.1 Z-contrast for direct thickness measurement	47

3.3.2	Attenuation of the direct beam in diffraction mode	48
3.3.3	Comparative density of EDS signal	49
3.3.4	Diffraction tilt series	49
3.4	Multislice simulations of MoS ₂ and the Au-MoS ₂ system	49
3.4.1	Generating simulations of rippling and tilting in MoS ₂	50
3.5	Forbidden reflections of Au in electron diffraction	52
3.6	Calibration approaches for measuring strain using diffraction data	54
3.7	Estimating Au morphology from HAADF images	59
3.8	Moiré analysis	64
3.9	Chapter 3 Summary	67
4	STEM studies of MoS₂ and evaporated Au	70
4.1	Epitaxial alignment of Au on MoS ₂	70
4.1.1	Epitaxial alignment of Au: Moiré analysis	72
4.2	Presence of strain	75
4.3	MoS ₂ rippling	80
4.4	Self-organization and growth of nanoporous Au	82
4.5	Rotation of epitaxial Au: Diffraction analysis	83
4.5.1	Rotation: Moiré analysis	89
4.6	Chapter 4 Summary	94
5	Photoluminescence Characterization of MoS₂ and WS₂ Prepared by Gold-Assisted Exfoliation	98
5.1	Applicability of photoluminescence spectroscopy (PL) for MoS ₂ and WS ₂ layer characterization	99
5.2	Discussion of photoluminescence spectroscopy characterization	100
5.3	Experimental methods	104
5.3.1	Sample preparation: Exfoliation using thermal release tape as adhesive layer	104
5.3.2	Sample preparation: Exfoliation using unbaked photoresist as adhesive layer	108
5.3.3	TFSI superacid treatment steps	109
5.3.4	Photoluminescence spectroscopy instrumentation and analysis methods	109
5.4	Chapter 5 Summary	110
6	Summary: the Complex Au-MoS₂ landscape	114
6.1	Current opportunities and pitfalls in 4D STEM	114
6.2	Synopsis of discoveries	115

6.2.1	Au-MoS ₂ epitaxy and rotation	115
6.2.2	On searching for Au-MoS ₂ epitaxial strain in a TEM	118
6.3	Looking to the future	119
Appendices		125
A.	Computer vision for 4D STEM data analysis	125
B.	Atomic-resolution STEM microscope instrumentation	127
C.	E-beam evaporation deposition parameters	130
D.	Additional figures	131
Acronym Index		137
Glossary		139

Acknowledgments

*Dicebat Bernardus Carnotensis nos esse quasi **nanos gigantium humeris insidentes**, ut possimus plura eis et remotiora videre, non utique proprii visus acumine, aut eminentia corporis, sed quia in altum subvenimur et extollimur magnitudine gigantea.*

– John of Salisbury

I have only breathless words of thanks for the multitude of people who have lit my path all these years. If I have seen a little further, it is because I have stood on the shoulders of giants.

My first and deepest thanks go to my family, both in the U.S. and India, who have provided an unwavering foundation of tenacity, support, and optimism on which to stand and face each new challenge. Thank you, Mom and Dad, for inspiring my curiosity, enabling my ambitions, and leaving me the freedom to chart my own course while sharing your wisdom along the way. Thank you for planning one and a half weddings with me from across the country while I worked on my PhD, and for always keeping a place for me at home. Samantha, my phenomenal sister, has kept me grounded with a listening ear, solid advice, and good humor. I am thankful for her unrivaled ability to broaden my perspective beyond this small slice of academia and remind me of my whole self. You were right. And to my brother Nicholas and sister-in-law Heather: thank you for flying around the world for multiple weddings and for your advice on finance and pillow fights.

I am eternally grateful for my husband Rishabh, who came into my life a week before my first-ever class in Materials Science and Engineering, and who has since been a steadfast partner, coach, sounding board, motivational speaker, counselor, and respite throughout my entire undergraduate and graduate careers. You brewed countless mugs of coffee and tea, absorbed my frustration when I hit roadblocks in my experiments, and was always willing to look over a paragraph or figure or email

to check my sanity. A fond memory from this endeavor is the poster and conference presentation we co-authored together. Thank you, my love.

Ma and Papa, your guidance and support as Rishabh and I navigate this fast-changing phase of life has been invaluable. Thank you for welcoming me into the family, for celebrating each and every milestone, and for lending your wisdom in the face of any obstacle. And of course, you have given me not only a life partner but a little sister. Richa, I am so lucky to have you in my life and so excited to see how you will make the whole world shine as brightly as you do.

I would like to acknowledge my advisor, Prof. Joel Ager, for his boundless enthusiasm for ideas, his optimism in the face of the unknown, and his spirited willingness to see the world in new ways.

To my co-advisor, Prof. Oscar Dubon: your group has been a haven for its members. Your deep compassion helped me rise to meet the most difficult moments of this endeavor. Thank you for seeing the journey in each of us.

Thank you to my qualifying exam committee, Prof. Andrew Minor, Prof. Mark Asta, and Prof. Michael Crommie, for your advice and encouragement, even as I took my exam virtually, just two weeks into quarantine.

I'd like to thank Prof. Daryl Chrzan, Prof. Hayden Taylor, and the students and postdocs of the Nanomeeting collaboration for illuminating discussions, support, friendship, and shared research endeavors. Dr. Hannah Gramling, I will fondly remember our all-hours discussions of the challenges of grad school and working on your exfoliation paper over many meetups in Berkeley Espresso and Yali's. Thank you to Dr. Vu Nguyen, Eric Sirott, Humberto Batiz Guerrero, Haoye Sun, Dr. Ji Guo, and the rest of the team.

My heartfelt thanks to the invaluable staff of the National Center for Electron Microscopy (NCEM). Dr. Karen Bustillo, your dedication to student training and your technical mastery are legendary. Dr. Chengdu Song, thank you for training me on microscopes from two different centuries. Dr. Peter Ercius and Dr. Colin Ophus, you continue to astound me with your drop-everything dedication to user research. Dr. Benjamin Savitzky and Steven Zeltmann, I dearly appreciate your help in understanding my data using py4DSTEM. Prof. Mary Scott and Catherine Groschner, you are rock stars, and your collaboration launched this intriguing, all-consuming

project into the world of microscopy.

Special thanks go to the leadership and operations teams of the Molecular Foundry. Dr. Laurie Chong and Dr. Branden Brough, you took a chance on me and as a result, have changed the direction of my career, and I am so grateful. Dr. Shannon Ciston, there are few things as fun as creating something from nothing with a great team by one's side. It has been a profound pleasure to work with you all.

I'd also like to acknowledge Dr. Mark Hettick, Dr. Der-Hsien (Danny) Lien, Dr. Martin Amani, Aiden Kim, Shiekh Uddin, and the rest of the Electronic Materials Program (EMAT) students and safety officers who trained me on the photoluminescence setup, the e-beam evaporator, the superacid protocol, and the AFM, and who troubleshooted with me when the laser was out of alignment, the band-pass filters were missing, or any of the other myriad mishaps that characterize an experimental PhD. With kindness, sarcasm, and ingenuity, we could always figure it out.

Many thanks to my friends and roommates, particularly my cohort-mates in Materials Science: Julia Yang, Zhen Lin, Dr. Rebecca Stern, and Dr. Edy Cardona. I am deeply glad that we shared so much of this experience, supporting one other from our preliminary exams and coursework to our qualifying exams and dissertation drafting sessions. Dr. Rachel Woods-Robinson, your fellow students have benefited immeasurably from your exuberance, resilience, and knack for community-building. You will all do the most incredible things.

Finally, I'd like to extend my gratitude to the funding agencies and grants which allowed me to learn, work, and teach at UC Berkeley and Berkeley Lab for the past five years: the Materials Science and Engineering Department of UC Berkeley; the National Science Foundation Graduate Research Fellowship Program; NSF Award 1636256: SNM: Scalable Nanomanufacturing of 2D Electronic Materials and Devices Using Automated Exfoliation; the Electronic Materials Program, funded by the Office of Science, Office of Basic Energy Sciences (Materials Sciences and Engineering Division), of the U.S. Department of Energy, under contract no. DE-AC02-05CH11231; and the Molecular Foundry, supported by the Office of Science, Office of Basic Energy Sciences (Scientific User Facilities Division), of the U.S. Department of Energy under Contract No. DE-AC02-05CH11231.

It's been an honor. Thank you.

List of Figures

1.1	Schematic of the three known polytypes, or phases, of MoS ₂ . a,d,g) The 1T octahedral phase. b,e,h) The 2H hexagonal phase. c,f,i) The 3R rhombohedral phase. The top row (a-c) shows a unit cell view, the middle row (d-f) shows a profile view along the <i>-a</i> direction, and the bottom row (g-i) shows a top view.	3
1.2	The most commonly-reported epitaxial alignment of Au grown on MoS ₂ . The (111) plane of Au is parallel to the (0001) basal plane of MoS ₂ , and the [11 $\bar{2}$ 0] direction of MoS ₂ is parallel to the [110] direction in Au.	5
1.3	Simplified diagram depicting the two basic operations of the TEM imaging system: a) diffraction mode, which projects a diffraction pattern onto the viewing screen or camera and b) imaging mode, which projects an image of the sample onto the screen or camera. In diffraction mode, a selected-area (SA) aperture may be used, the objective aperture is removed, and the intermediate lens selects the back focal plane of the objective lens as its object. In imaging mode, the objective aperture is inserted, the SA aperture is removed, the intermediate lens selects the image plane of the objective lens as its object. <i>Figure reprinted with permission from Springer Science+Business Media: David B. Williams and C. Barry Carter. "The Instrument". In: Transmission Electron Microscopy. Boston, MA: Springer US, 2009, pp. 141–171. Copyright Springer US.</i>	10

1.4	Schematics of TEM diffraction in STEM mode. a) Ray diagram of a converged STEM probe. b) Scanning the convergent probe for STEM image formation using two pairs of scan coils to ensure that the probe remains parallel to the optic axis as it scans across the specimen. c) Schematic of converged probe STEM diffraction disks, whose width is proportional to the beam convergence angle, α . d) Ray diagram depicting the creation of a convergent-beam diffraction pattern in the back focal plane of the objective lens. <i>Figures adapted with permission from Springer Science+Business Media: David B. Williams and C. Barry Carter. Transmission Electron Microscopy. Boston, MA: Springer US, 2009. Copyright Springer US.</i>	11
1.5	Intersections of the Ewald sphere with the reciprocal lattice of a simple cubic crystal, and two zones of bright diffraction spots. <i>Figure and caption adapted with permission from Springer Nature: Brent Fultz and James Howe. "Diffraction from Crystals". In: Transmission Electron Microscopy and Diffractometry of Materials. pp. 279. Copyright Springer-Verlag Berlin Heidelberg 2013.</i>	14
1.6	Schematic of the intersection of reciprocal lattice rods with the Ewald sphere. The incident beam is diffracted by a Bragg plane at point C . k_0 is the unscattered wavevector; k_D is the diffracted wavevector. Accordingly, K is the scattering vector. g is the reciprocal lattice vector between points O and G . s is the difference between K and g . Scattered intensity is highest when $ K = g $	16
2.1	Schematic of 4D STEM data collection across a sample of epitaxial Au on MoS ₂ . A molecular ball-and-stick model is shown above a representative diffraction pattern, color-scaled to illustrate the high dynamic range.	25
2.2	Diagram of a TEM column set up in selected-area diffraction mode.	28
2.3	Schematic comparison between SAED (a,d), NBED (b,e), and CBED methods (c,f). The top row shows a representative spot pattern, and the bottom row shows a simulated diffraction pattern generated using the PRISM method, based on the multislice method (see section 2.3.3).	29
2.4	Screenshot of Mathematica tool that shows the corresponding diffraction pattern for the location where the user hovers their mouse pointer on the HAADF image.	32

2.5	Workflow chart for generating a virtual crystal and generating simulated STEM diffraction patterns using the plane-wave reciprocal-space interpolated scattering matrix (PRISM) algorithm.	36
3.1	Kapton tape was used to exfoliate relatively flat, thin areas of natural molybdenite and mount the samples to large glass slides prior to the deposition of gold via e-beam evaporation.	41
3.2	A range of Au morphologies are found to occur on MoS ₂ following e-beam deposition. Left: a dense, nanoporous Au structure on MoS ₂ . The Au does not form a continuous film. Right: Au is seen forming an ‘island’ morphology, with epitaxial alignment and preferential faceting. These domains can occur in close proximity to one another (center).	44
3.3	Three representative EDS spectra from two Au-MoS ₂ samples. The copper and carbon peaks are due to scattering from the copper TEM grid with lacy and ultra-thin carbon supports. The relative heights of the Au and Mo peaks vary with the Au density and MoS ₂ thickness in the analyzed area.	45
3.4	Table showing a variety a subset of virtual crystal systems for which PRISM simulated diffraction patterns were generated. Gold crystallites of various morphologies, together with 2H-MoS ₂ of different layer thicknesses, are simulated together in a finite system.	51
3.5	Table displaying simulated diffraction patterns as a finite virtual MoS ₂ crystal is tilted about both the x- and y-axes. The center image is oriented precisely along the MoS ₂ [0001] zone axis, and each rotational step is 3°. This simulation subset, then, sweeps from ±6° about the x-axis, and from ±3° about the y-axis. Displayed together, diffraction disks from the zero-th, first, and second-order Laue zones are readily observed.	53

- 3.6 Schematic drawing of the fcc reciprocal space including the ZOLZ spots for both [111] and [112] zone axes and the “upper” and “lower” {111} FOLZ spots of the (111) ZOLZ plane. As the {111} relrods are elongated along the [111] direction, they intercept both the (111) and (112) planes. They have been indexed accordingly. Thus, in the [111] zone axis, the reflections indexed as {111} are those corresponding to the $1/3\{422\}$ forbidden reflections, while in the [112] zone axis they correspond to the $1/2\{131\}$ forbidden reflections. *Figure and caption reprinted with permission* from Reyes-Gasga, J., Gómez-Rodríguez, A., Gao, X., and José-Yacamán, M. (2008). On the interpretation of the forbidden spots observed in the electron diffraction patterns of flat Au triangular nanoparticles. *Ultramicroscopy*, 108(9), 929–936, with permission from Elsevier[10]. 55
- 3.7 The Au $1/3\{422\}$ disks are visible in real data and simulated diffraction patterns. a) HAADF image of thin, flat, faceted Au crystallites grown on multilayer MoS₂. b) Summation of 2500 diffraction patterns from the boxed region in (a). A ‘forbidden’ Au reflection is labeled. c) A single diffraction pattern from a different area of the sample exhibiting a twist between Au and MoS₂ that also shows the ‘forbidden’ Au $1/3\{422\}$ disks. d) Simulated diffraction pattern from a virtual crystal comprised of 16 atomic layers of Au{111} on monolayer MoS₂. Here, the ‘forbidden’ Au disks exhibit a higher intensity than the nearby MoS₂{110} peaks, although thicker MoS₂ regions will result in higher intensities for those reflections. 56
- 3.8 (A) For a thin specimen, every point is replaced by a relrod. (B) The Ewald sphere cutting the relrods in (A) when the crystal is tilted slightly off the (001) axis. (C) The effect of the tilt in (B) on the DP. Notice that all of the spots in the DP are displaced relative to their positions on the square grid (the projection of the spots at zero tilt), but that the magnitude of the displacement varies depending on the sign and size of s. Of course, spots on the Ewald sphere must be the ‘correct’ distance from 000. *Figure and caption reproduced with permission from* Springer Science+Business Media: David B. Williams and C. Barry Carter. “Diffraction from Small Volumes”. In: *Transmission Electron Microscopy*. Boston, MA: Springer US, 2009, pp. 274. Copyright Springer US. 58

3.9	Pseudo-3D map of Au thickness from HAADF data of Au grown on MoS ₂ . Above: HAADF image of nanoporous Au on multi-tiered multilayer MoS ₂ . Bottom: Pseudo-3D map obtained by following the step-by-step workflow in section 3.7.	63
3.10	A Moiré fringe spacing of 1.8 nm is obtained from an HR-STEM image of Au deposited on MoS ₂	65
3.11	Projected 2D crystals of 2H-MoS ₂ along the [0001] direction and fcc Au along the [111] direction account for the shorter Moiré period observed in STEM imaging. Layers are labeled with ‘A’, ‘B’, or ‘C’ to indicate stacking structure.	67
4.1	Diffraction pattern showing the (111) orientation of Au grown epitaxially on MoS ₂ (0001). a) the unlabeled diffraction pattern. b) the same diffraction pattern with disks indexed according to an MoS ₂ zone axis of [0001], shown in magenta, and according to an Au zone axis of [111], shown in green. The $1/3\{422\}$ reflections are shown in light green. . .	71
4.2	HAADF images showing consistent epitaxial alignment of Au crystallites grown on MoS ₂ . Above: Some truncated triangular Au crystallites are highlighted by red and cyan outlines, showing the symmetric alignments. Below: Triangular Au crystallites are highlighted by yellow and green outlines, showing the consistent symmetries.	73
4.3	A small subset of 4D STEM images, using a bullsye aperture, collected as the beam scanned across a gold nanoparticle on a single MoS ₂ crystal. Each diffraction pattern shown above was taken 4 nm apart, and cross a gold nanoparticle about 12 nm in size. Patterns 1 and 5 show diffraction patterns from MoS ₂ along the [0001] zone axis, taken on either side of the nanoparticle. Patterns 2 and 3 are taken from the middle of the Au nanoparticle. Pattern 3 includes an overlay of the MoS ₂ [0001] and Au[111] diffraction patterns in magenta and green, respectively. Pattern 4 was taken on the edge of the nanoparticle. The beam spot size was about 2 nm at FWHM.	74
4.4	Even tilted slightly off-axis, the 10-to-11 Moiré periodicity of 32 Å is observed between MoS ₂ and Au, respectively. Molybdenum atoms are clarified by a lavender overlay, with brighter atoms corresponding to a higher HAADF intensity and thus more atoms in the column. Sulfur atoms diffract too weakly to be discerned with these microscope conditions, and an overlay for them is not shown.	76

4.5	A mean Moiré pattern spacing of 1.8 nm is measured from two HR-STEM images of Au deposited on MoS ₂ . The respective FFTs are shown in the insets.	77
4.6	4D STEM strain maps of single-crystal MoS ₂ terraces, analyzed using py4DSTEM. Top-left: HAADF images of MoS ₂ terraces; top-right: map of strains along the horizontal (x) direction; bottom-left: map of shear xy strain; bottom-right: map of local rotation. The range of colors expressed in each map is demarcated by a green box in their respective color bar legend.	79
4.7	Single diffraction pattern from a 4D STEM dataset scanning few-layer MoS ₂ . An ideal simulated MoS ₂ [0001] diffraction pattern is overlaid in magenta.	81
4.8	Single diffraction pattern from a 4D STEM dataset scanning few-layer MoS ₂ , taken using a bullseye aperture. An ideal simulated MoS ₂ [2 $\bar{1}$ 1] diffraction pattern is overlaid in magenta.	81
4.9	Large-period corrugation in a flake of multilayer MoS ₂ suspended on a web of lacey carbon and ultrathin carbon.	82
4.10	A large flake of single-crystal MoS ₂ , coated entirely with nanoporous gold. a) A low-magnification HAADF-STEM image of the flake. b) A higher-magnification image of a subsection of the flake shown in (a), marked by a dashed green rectangle. c) EDS map: Integrated EDS peak intensities at each pixel position corresponding to Mo-K and S-K transitions from the subsection shown in (b). d) EDS map: Integrated EDS peak intensities at each pixel position corresponding to the Au-L transition from the subsection shown in (b).	84
4.11	A large flake of single-crystal MoS ₂ , coated entirely with nanoporous gold. Two HAADF-STEM images are merged in the above image, joined at the green line shown.	85
4.12	Gold nanoparticles on the TEM grid that are not adhered onto the cleaved MoS ₂ . The Au likely grew onto an impurity, which may have then been pumped out by the vacuum or destroyed by the electron beam.	86
4.13	Apparent significant rotation between epitaxial Au and underlying MoS ₂	87

4.14	On the same sample, Au can exhibit different relative rotations with respect to the underlying MoS ₂ lattice. a) The diffraction pattern from the location marked ‘a’ in the HAADF image in b. Here, the Au lattice is twisted with respect to the underlying MoS ₂ by about 1.2°. Bright colored lines show perfect alignment, while faint colored lines are fit to the rotated disks. b) HAADF-STEM image of area where 4D STEM diffraction patterns were collected with a step size of 1 nm. 80 nm x 80 nm scan area marked by a red box. c) The diffraction pattern from the location marked ‘c’ in the HAADF image in b. Here, Au is well-aligned with the underlying MoS ₂	88
4.15	EDS, HAADF, and deformation maps of an Au-MoS ₂ sample. py4DSTEM was used to analyze 2500 diffraction images collected over a 500x500 nm ² sample area. Au was found to exhibit an (111) epitaxial orientation with respect to the underlying MoS ₂ flake. a) Au-L EDS map of the area marked by the teal square in (c). b) Combined Mo-K and S-K map of the area marked by the teal square in (c). c) HAADF image of a flake of MoS ₂ with deposited nanoporous gold. d) HAADF inset of the 4D STEM scan area. e-f) Deformation maps generated through a careful py4DSTEM analysis of the Au diffraction disks in the 4D STEM dataset. Blackout areas are locations where the MoS ₂ is corrugated, thus changing the zone axis in those areas. e) Au strain map oriented such that the x-axis along the scan direction. f) Au strain map oriented such that the y-axis is perpendicular to the scan direction. g) Map of the shear component of the Au deformation tensor. h) Rotation of the nanoporous Au with respect to the median rotation. A sweep of ±2° is reported.	90
4.16	FFT analysis of high-resolution STEM imaging data (left) reveal a twist variation of ±2° from the expected epitaxial alignment.	91

4.17	Atomic-resolution STEM images of Au nanoparticles grown on few-layer MoS ₂ , with FFTs shown as insets. a) A monolayer of hexagonal MoS ₂ suspended on an ultrathin carbon support. b) A twisted bilayer of MoS ₂ , exhibiting a twist Moiré pattern corresponding to an interplanar rotation of about 8.4°. The bright region at the bottom of the image is a large Au grain. c) An epitaxially-aligned nanoparticle of Au on bilayer 2H-MoS ₂ . MoS ₂ is shown to bend with a radius of curvature of about 50 nm. Individual gold atoms appear as bright points moving across the MoS ₂ surface due to beam irradiation. d) Au nanoparticles on few-layer MoS ₂ . One nanoparticle is co-located with a small piece (6-nm diameter) of MoS ₂ monolayer which is rotated by 8.4° relative to the MoS ₂ underneath.	93
5.1	Optical image and corresponding photoluminescence spectrum of an exfoliated MoS ₂ flake, consisting mostly of monolayer material. Left: Optical white-light image of an exfoliated flake of MoS ₂ on 260 nm thermal SiO ₂ on Si. Right: Photoluminescence spectrum collected from the area circled in yellow in the optical image. The peaks corresponding to the A- and B-excitons of MoS ₂ are labeled.	101
5.2	Optical image and corresponding photoluminescence spectra of an exfoliated MoS ₂ monolayer flake. Top: Combination of four optical white-light images of an exfoliated flake of MoS ₂ on SiO ₂ . Bottom: Photoluminescence spectra collected from the areas indicated in the optical image. The A-exciton and B-exciton peaks are labeled.	102
5.3	Optical image and corresponding photoluminescence spectra of an exfoliated WS ₂ flake, consisting of monolayer, bilayer, and multilayer areas. Top: optical white-light image of an exfoliated flake of WS ₂ on SiO ₂ . Bottom: Photoluminescence spectra collected from the areas indicated in the optical image.	103

- 5.4 Optoelectronic MoS₂ monolayer characterization. (a) White-light reflectance image of a set of transferred MoS₂ features on 260 nm thermal SiO₂ on Si; (b) photoluminescence image of the region; (c) photoluminescence spectra associated with the numbered locations in (a), confirming that monolayer MoS₂ has been transferred to the substrate; (d) the results of treating MoS₂ monolayers with a superacid, showing more than a one hundred-fold increase in quantum efficiency. *Reprinted with permission from* Hannah M. Gramling, Clarissa M. Towle, Sujay B. Desai, Haoye Sun, Evan C. Lewis, Vu D. Nguyen, Joel W. Ager, Daryl Chrzan, Eric M. Yeatman, Ali Javey, and Hayden Taylor. “Spatially Precise Transfer of Patterned Monolayer WS₂ and MoS₂ with Features Larger than 10⁴ μm² Directly from Multilayer Sources”. In: *ACS Applied Electronic Materials* 1 (2019), pp. 407–416. Copyright 2019 American Chemical Society. 105
- 5.5 Optical and optoelectronic WS₂ monolayer characterization. (a) White-light reflectance image of a set of transferred WS₂ features on 260 nm thermal SiO₂ on Si. (b) Photoluminescence image of part of the same region as in (a): orientation is the same as (a), and the outline corresponds to that of the region imaged in (a). (c) Photoluminescence spectra from 13 regions of WS₂ on 260 nm thermal SiO₂ on Si, confirming that monolayer WS₂ has been transferred to the substrate. (d) Result of treating a WS₂ monolayer with TFSI superacid, showing more than a 25-fold increase in quantum efficiency. *Reprinted with permission from* Hannah M. Gramling *et al.* “Spatially Precise Transfer of Patterned Monolayer WS₂ and MoS₂ with Features Larger than 10⁴ μm² Directly from Multilayer Sources”. In: *ACS Applied Electronic Materials* 1 (2019), pp. 407–416. Copyright 2019 American Chemical Society. 106

6.1	Color-scaled simulated diffraction patterns for a virtual sample comprised of 10 planes of Au(111), forming a faceted truncated triangular crystallite, epitaxially aligned on top of 10-layer MoS ₂ . a) Diffraction disks from each crystal species are clearly visible, as well as the hexagonal superstructure diffraction disks. b) Diffraction pattern where the Au crystallite was rotated azimuthally by 2° relative to the MoS ₂ substrate. c) Diffraction pattern where the entire sample was tilted by 6° about the x-axis (as an off-zone measurement). d) Diffraction pattern where the Au crystallite was rotated about the z-axis by 2° relative to the underlying MoS ₂ and the entire sample was also tilted by 6° about the x-axis.	117
A.1	Training a convolutional neural network (CNN) to classify NBED-STEM electron diffraction patterns. A training set of simulated diffraction patterns were generated for MoS ₂ [0001], Au[111], Au[211], and the direct probe (without a sample, or ‘over vacuum’). a) A subset of the training and verification data used to train the CNN. b) A schematic of the neural network architecture model, with the 65536 pixels in a binned, 256x256 pixel diffraction pattern serving as the input vector, and the crystal classifications as the output vector. c) A comparison of the experimental data to simulated data.	126
A.2	Output of the CNN classification model. Top row: The HAADF reference image for the 4D STEM dataset and the corresponding confidence map of a model trained only to recognize the presence or absence of MoS ₂ . Bottom row: The HAADF reference image for the 4D STEM dataset and the corresponding confidence maps of a model trained to classify each image as containing MoS ₂ , Au[111], or Au[211]. The model was not allowed to select two crystals, so areas of low confidence exist on the borders of the segmented domains.	128
D.3	White light optical microscope image (left) and atomic force microscopy (AFM) height map (right) of a bilayer and monolayer region of a gold-assisted exfoliated MoS ₂ flake. Compared to the SiO ₂ substrate, one layer of MoS ₂ has a height of about 7 Å. An additional step of 7 Å is observed to the bilayer regions. Au nanoparticles about 5 nm in height remain following the KI/I ₂ Au etch; their chemical identity was confirmed using x-ray photoelectron spectroscopy (XPS) analysis as discussed in the supplementary information with reference [1]. . . .	131

D.4	Single diffraction pattern from a 4D STEM scan of an Au-MoS ₂ sample which had been briefly annealed at 120°C for 1 minute. Left: Au(111)-MoS ₂ (0001) diffraction pattern. Right: Simulated diffraction patterns of Au (green) and MoS ₂ (magenta) overlaid on the same experimental diffraction pattern as (Left). No rotational misalignment is identified between the Au and the MoS ₂	132
D.5	The FFT (inset) of a HAADF image of nanoporous Au on MoS ₂ shows an angular sweep of 60.6°, corresponding to a variation of ±30.3°. When divided by the Moiré magnification factor for this image, 15.8 Å/1.58 Å = 10, this yields a real-space angular variation of ±3° over the 400-nm Au-MoS ₂ sample area above.	133
D.6	The angular distribution of Au grains in Fig. D.5. The pixel intensities of the elliptical streaks in the FFT (inset of Fig. D.5) were summed along their minor axes and plotted along their major axes (essentially summing their length-wise line profiles across their widths). The pixel ranges were reassigned values in degrees corresponding to the interior angle of the streak divided by the Moiré magnification factor measured for this sample. The histogram of both reflections is shown alongside a fitted Gaussian distribution with a standard deviation of 1.05°. . . .	134

Chapter 1

Introduction

This dissertation sets out to answer one broad question: how do a deposited thin film of gold and a molybdenum disulfide substrate relate to, and influence, one another? While concise, this central question has a multitude of answers, ranging with the conditions of the materials system in question, the properties of interest, and the size of the system itself. Answering this question also relies on one's ability to design an appropriate characterization method using one or several characterization tools and to select a narrow set of experimental conditions from a vast set of possible combinations.

In the following chapters, we will attempt both to define and critique a certain characterization approach for studying Au-MoS₂ epitaxy, and we will explore newly observed nanoscale heterogeneity in a system that has been studied for more than seven decades. This work employs a still-young characterization approach, 4D scanning transmission electron microscopy (4D STEM), coupled with 'workhorse' TEM techniques such as high-angle annular dark field imaging (HAADF STEM) and energy dispersive x-ray spectroscopy (EDS) to make detailed observations of the complex landscape of this materials system.

Molybdenum disulfide, also known by its mineral name molybdenite, is known to the industrial world as a dry lubricant. It can be mined naturally, found in hydrothermal ore deposits with other minerals such as pyrite (fools' gold) and quartz. Its lubricating property is owed to the fact that MoS₂ is formed of covalently bonded molecular sheets bound to one another by comparatively weak van der Waals forces. When thinned down to nanoscale proportions (< 10 nm), MoS₂ is considered a two-dimensional material.

1.1 Two-dimensional transition metal dichalcogenides

MoS₂ is one of a class of layered, semiconducting materials known as the transition metal dichalcogenides (TMDCs), comprised of an element from the chalcogen (oxygen) family and a transition metal, in a 2:1 proportion. When a monolayer is isolated from the multilayer crystal, the electronic properties of the TMDC can undergo a dramatic shift. In MoS₂, the band gap changes from an indirect gap of 1.2 eV in the bulk to a direct gap of 1.8 eV in the monolayer[1]. This intriguing feature has driven, in part, the recent surge in investigation into MoS₂ as a candidate for atomically-thin electronics, photonics, and spin valleytronics. In the last 7 years, for example, monolayer MoS₂ has been utilized in the world’s smallest transistor[2], in a strain-tunable photodetector[3], and in a centimeter-scale LED display[4]. Other early and prospective applications of the 2D TMDCs can be found in reviews [5–9].

The basic structure of TMDCs is as follows: one layer of transition metal atoms (e.g., Mo, W) in-between two layers of chalcogen atoms (e.g., S, Se). The 3D crystal is formed by stacks of these layers, with only van der Waals bonding between them. These weakly bonded multilayers, as in graphite, are the basis for the use of materials like molybdenite as dry industrial lubricants. There are several distinct solid phases (polytypes) of most TMDCs, identified by their unit cell symmetry and the number of layers required for distinction between them: 1, 2, or 3. For MoS₂, the most stable phase at room temperature and pressure is the 2H phase, which is comprised of an AB stacked van der Waals crystal with hexagonal symmetry, shown in Figure 1.1. Each layer of 2H MoS₂ is a glide reflection of the layer above or below it: the atom placements correspond to a translation of $c/2$, where the c is the unit cell vector along the stacking direction, and a reflection across the (100) plane. The semi-metallic, metastable 1T octahedral phase has also been observed, with AA stacking. Finally, the 3R phase has a rhombohedral unit cell and is defined by its ABC stacking.

The last fifteen years has seen an accelerating effort to exfoliate large, high-quality monolayers of MoS₂ and other TMDCs, both from their bulk forms and from grown multilayers [10]. As part of this effort, my colleagues and I have grown, exfoliated, characterized, and built simple devices from MoS₂ and WS₂, including both natural and contrived bi-layers and heterostructures[11, 12]. My contribution to this work will be discussed in detail in Chapter 5; for now, it is pertinent to introduce the two features that form the premise of these advances in TMDC exfoliation: 1) an Au ‘handle’ layer and 2) a compliant temporary ‘superstrate,’ which is used to grip the materials stack from above.

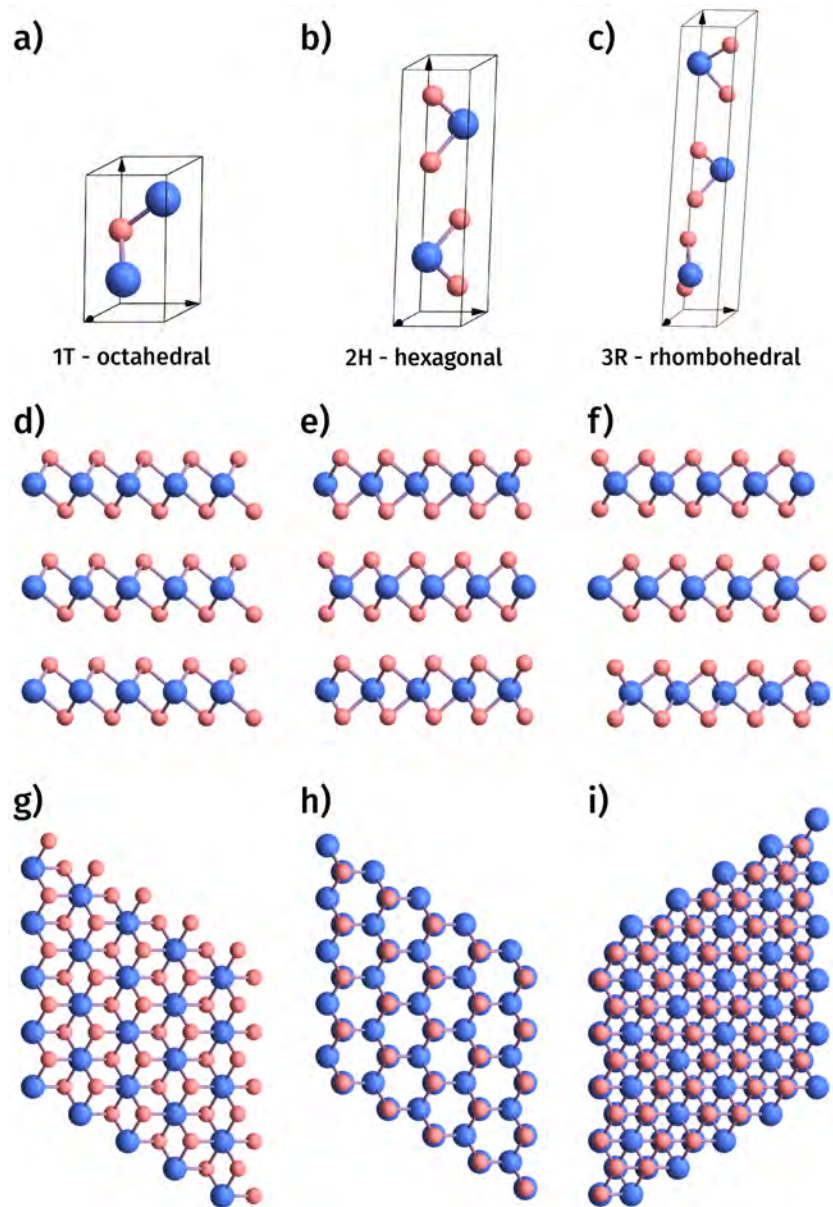


Figure 1.1: Schematic of the three known polytypes, or phases, of MoS_2 . a,d,g) The 1T octahedral phase. b,e,h) The 2H hexagonal phase. c,f,i) The 3R rhombohedral phase. The top row (a-c) shows a unit cell view, the middle row (d-f) shows a profile view along the $-a$ direction, and the bottom row (g-i) shows a top view.

In order to prepare the top layer of MoS₂ in a multilayer stack to be isolated and transferred as a monolayer to another substrate, it is advantageous to decrease the interlayer bond between that layer and the one immediately beneath it, thus increasing the probability that that interface will serve as a crack initiation site during mechanical exfoliation. Prior to the present work, it was found that the deposition of a thin film (100-150 nm) of gold on MoS₂ increased the size of exfoliated MoS₂ monolayers by nearly two orders of magnitude[13]. In subsequent work, Au films were used as a so-called ‘handle’ layer, leveraging the unusually strong bond between the gold and the surface chalcogen atoms of the TMDC layers to enhance the exfoliation process.

The second key feature of these exfoliation studies is the use of a compliant temporary superstrate, in this case is a polymer-backed adhesive tape or film, which serves to contact the gold layer, to protect the sample during certain steps in the lithographic patterning process, and to provide a physical anchor from which to initiate manual or mechanical cleavage without tearing or contaminating the TMDC layer itself.

1.2 Prediction of strain and motivation for selective exfoliation

The interfacial relationship that evolves between a metal film and a TMDC is of interest for the metal-assisted mechanical exfoliation of TMDCs as well as for TMDC-metal electronic junctions. Recent work by Zhou *et al.* computed from first principles the likely epitaxial relationships between Au and MoS₂, namely the favored alignment of the (111) plane of Au with the (0001) basal plane of MoS₂ (Figure 1.2). The stronger-than-usual van der Waals bond that forms between the gold and the sulfur is thought to play a key role in both the lattice alignment and any strains that persist at the interface[14, 15], given the significant Au-MoS₂ lattice mismatch on the order of 9%.

There is ample work, both experimental and computational, supporting the preferred rotational alignment of the MoS₂ basal plane (0001) to the (111) plane of FCC crystals such as Au, starting with Yoshiro Kainuma’s first recorded observations in 1950[16]. This relationship is seen consistently, whether MoS₂ is grown on these FCC metals [17–22], or whether the metal is deposited onto MoS₂[23–27]. The closest re-

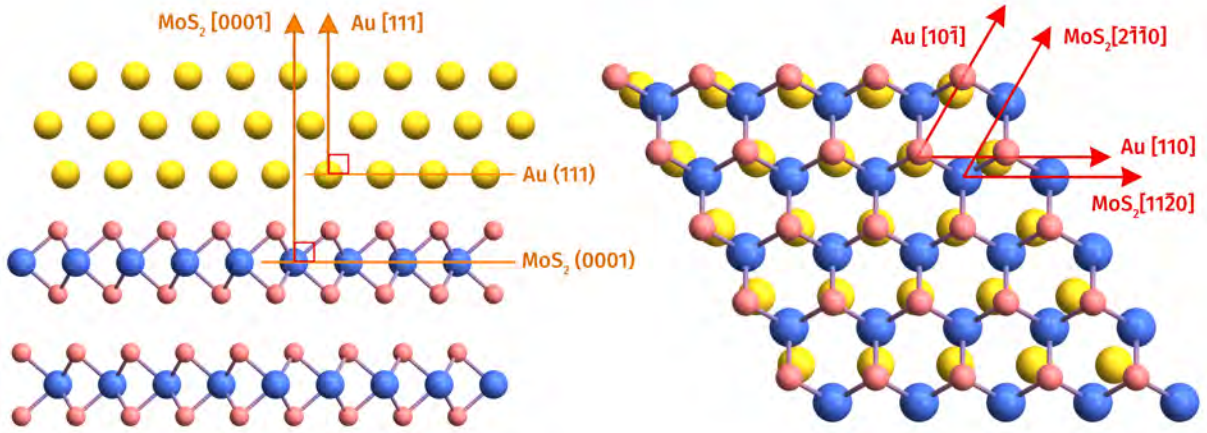


Figure 1.2: The most commonly-reported epitaxial alignment of Au grown on MoS₂. The (111) plane of Au is parallel to the (0001) basal plane of MoS₂, and the [11 $\bar{2}$ 0] direction of MoS₂ is parallel to the [110] direction in Au.

lation to MoS₂, tungsten disulfide (WS₂), is also observed to have this relationship with Au[28].

While Au nuclei that form on the surface of MoS₂ could be initially strained in an attempt to match lattice spacings while they remain below a critical size, it is thought that misfit dislocations will eventually arise to relieve the strain energy from any initial coherent epitaxial condition[29]. For example, evidence of dislocation movement in Au has been observed when 100-nm Au films were grown on MoS₂, particularly at elevated substrate temperatures[25].

Colleagues have previously predicted that strains resulting from this mismatch would weaken the van der Waals bonding between the top two MoS₂ layers, creating the possibility of using Au to increase the yield of selective monolayer exfoliation [14, 29, 30]. In fact, we and others have exploited this effect to successfully exfoliate large areas of monolayer MoS₂ from a multilayer stack[11]. We have also extended the process to the high-yield exfoliation of lithographically defined features[12]. This process and its subsequent iterations are described by references [11–13, 29] and summarized in section 5.3 of this work.

1.3 Thin film epitaxy: definitions, paradigms, and relevance

Before we begin to explore the interfacial relationship of gold and molybdenum disulfide, including an analysis of whether, and what type of, an epitaxial relationship exists between them, an introduction of thin film epitaxy is warranted.

Epitaxy is defined as a rotationally-oriented relationship between two crystals, with one crystal grown on the other in a preferred alignment. This relationship evolves in order to minimize the free energy of the interface, and crystals with similar symmetries and lattice constants often exhibit highly regular epitaxial relationships.

In cases where the two crystals are particularly well-matched, they can form a coherent interface. This ‘coherent epitaxy’ is a special case wherein the lattice constant of the grown crystal is constrained to that of the substrate. In the case of homoepitaxy, or self-epitaxy, where a crystal species is grown on an existing crystal of the same kind, a coherent interface would be expected. As a process, homoepitaxy is most often used to grow large single crystals with particular faceted surfaces.

Coherent epitaxy is an important tool in semiconductor engineering, particularly regarding devices utilizing the III-V group pairs, and in the field of ferromagnetics. However, coherence is a very special case of epitaxial growth, and is conditioned on such factors as atomic spacings, symmetry, bond types, electronegativity, temperature, defects, and the size of the constrained area. A coherent interface can reduce contact resistance in electrical devices and prevent energy losses from thermalization during device operation [6].

1.4 History of the relationship of Au grown on MoS₂

In this section, the earliest reports of Au-MoS₂ epitaxy from TEM studies in the 1950s and 60s will set the stage for the understanding of this relationship in modern scientific endeavors. The scientific ‘rediscovery’ of MoS₂ as an isolated monolayer and direct band-gap semiconducting material has warranted new examination of this metal-TMDC relationship, and some recent work has explored the relationships of metals on thin and monolayer samples of MoS₂ and other 2D transition metal dichalcogenides[31].

In the early 1940s at Nagoya Imperial University in Japan, Ryozi Uyeda was

among the first to deposit silver crystallites on a cleaved $\text{MoS}_2(0001)$ surface and identify that an epitaxial orientation existed using transmission electron microscopy[32]. At the time, the notion that dissimilar crystals would be constrained or influenced by atoms in a contacted plane was a novel and contested idea. It was found that silver, a face-centered-cubic (FCC) crystal, aligned to molybdenite with the (111) plane parallel to the cleaved (001) surface, and with the [110] vector of the Ag crystal parallel to the [100] vector of MoS_2 (the $[2\bar{1}\bar{1}0]$ vector in hexagonal notation). Ten years later, Uyeda’s student Yoshiro Kainuma identified the same relationship between cleaved molybdenite and gold, another FCC crystal[16].

The notation for this epitaxial alignment is as follows:

$$(111)\text{Ag}||(\text{001})\text{MoS}_2; [110]\text{Ag}||[100]\text{MoS}_2$$

Any epitaxial alignment can be defined by specifying the interfacial planes and one set of parallel directions in each crystal. For example:

$$(111)\text{Au}||(\text{0001})\text{MoS}_2; [01\bar{1}]\text{Au}||[11\bar{2}0]\text{MoS}_2$$

In the 1950s and 60s at Imperial College London, D.W. Pashley published a series of detailed epitaxy studies discussing the observed epitaxial growth of alkali halides, metals, and nonmetals in both homoepitaxial and heteroepitaxial conditions [23, 24, 33, 34]. Pashley cemented electron diffraction as the technique of choice for studying epitaxial systems, and he tabulated scores of observed epitaxial relationships and their growth and temperature conditions. Pashley was also among the first to observe the growth of Au on MoS_2 *in situ* in a TEM[24].

1.5 Interfacial rotations in 2D materials and epitaxial metals

Comprised almost entirely of surfaces, most 2D materials are inherently surface-sensitive, making them intriguing candidates for sensing applications and for novel electronic devices predicated upon these materials’ ability to modulate their electronic properties in response to their local bonding environment. One type of periodic modulation technique is imposing an interlayer twist in few- or bilayer 2D materials. Particularly after the 2018 discovery of superconductivity in ‘magic angle’ twisted bilayer graphene by Jarillo-Herrero’s group at MIT[35], the new field of twisted 2D materials rapidly emerged in the literature, paying particular attention to bilayer graphene and bilayer heterostructures based on the family of TMDCs[36,

37].

With regard to the question of interfacial rotation between epitaxially deposited metals and the TMDCs, there are few reports in the literature[38, 39]. The preferred epitaxial alignment between Au and MoS₂, described in the previous section, is reported widely; however, few reports discuss the presence of twist between these species or variation from the [01 $\bar{1}$]Au||[11 $\bar{2}$ 0]MoS₂ alignment. Yinghui Sun *et al.* report a measured $\pm 2.3^\circ$ rotation angle between epitaxial Au and MoS₂, derived from the fast Fourier transform of the Moiré fringes observed in high-resolution HAADF STEM[40]. As will later be described in section 4.5, this finding is consistent with both diffraction data and HR-STEM analysis undergone for this dissertation.

1.6 TEM methods for studying 2D materials

There are a number of advanced characterization techniques capable of examining materials on the nano-scale, each with their particular insights, strengths, and weaknesses. However, few techniques are so versatile and well-suited to the study of nano-dimensional materials than electron microscopy. With (sub)atomic resolution possible in all three dimensions, electron microscopy, and specifically transmission electron microscopy, is unrivaled in its ability to elucidate the finest structural details of nanoscale materials.

TEM

In a transmission electron microscope, a thermionic field-emission electron gun emits electrons using a filament, either tungsten or lanthanum hexaboride (LaB₆), and accelerates electrons using a potential of 60-300 kV, depending on the desired electron wavelength. Most experiments conducted throughout the course of this study were conducted at 300 kV, accelerating the electrons to a velocity of $2.33 * 10^8$ m/s, more than 3/4 the speed of light. The relationship between the microscope's accelerating voltage and the relativistic electron wavelength is given by equation 1.1:

$$\lambda = \frac{h}{[2m_0eV(1 + \frac{eV}{2m_0c^2})]^{1/2}} \quad (1.1)$$

where h is Planck's constant, m_0 is the mass of an electron, e is the fundamental

charge, V is the microscope accelerating voltage, and c is the speed of light.

When operated in so-called ‘TEM mode’, the microscope’s first two condenser lenses are adjusted such that the electron beam satisfies a parallel illumination condition, where the incident beam intersects an area of the sample typically several micrometers across with a parallel beam of electrons. This traditional mode of TEM operation produces contrast in the resulting image in response to anything that can put these coherent, parallel wavefunctions out of phase from one another (such as encountering dislocations in the crystal lattice), or in response to amplitude losses (e.g., electron absorption or scattering at very high angles). TEM mode is therefore useful for imaging the bulk structure of materials and studying a range of crystal defects. However, in order to examine such characteristics as strain and rotation in small (nm-scale) areas of a sample, a converged probe was selected for the studies in this dissertation.

STEM

Scanning transmission electron microscopy, or STEM, is a distinct mode of operation from TEM mode. It is possible to switch between these modes while operating a microscope; they do not require separate instruments. STEM mode operates by rastering a small probe, converged to a focal diameter of 0.1-5 nm, across a sample in order to produce an image of the sample or of the corresponding diffraction pattern in the back focal plane. Depending on the scattering angle of the diffracted electrons, several modes can be used to analyze STEM data: bright field, annular dark field, and high-angle annular dark field. Bright-field (BF) STEM images utilize electrons scattered at small angles of 0-10 mrad. Annular dark field (ADF) imaging generally utilizes electrons scattered between 10-50 mrad, and high-angle ADF (HAADF) collects and analyzes inelastically-scattered electrons between 50-200 mrad from the incident beam.

Contrast in STEM imaging mode has a power-law dependency on the atomic mass of the sample, allowing a relatively straightforward interpretation of imaging data. In dark-field STEM, brighter areas are either heavier or thicker (or both) than darker areas. This contrast mechanism will be discussed further in section 3.3.

In nanobeam diffraction mode, the convergence angle of the incident beam can be manipulated to best suit the given experiment. The smallest, sharpest diffraction

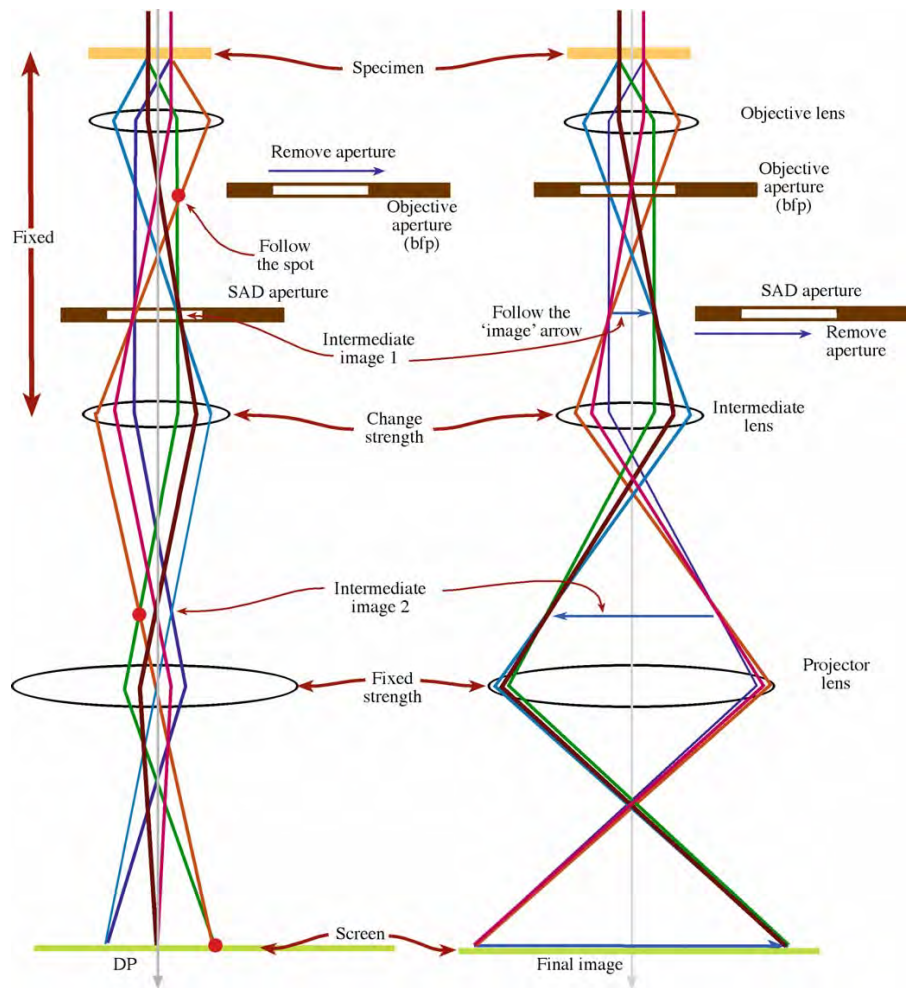


Figure 1.3: Simplified diagram depicting the two basic operations of the TEM imaging system: a) diffraction mode, which projects a diffraction pattern onto the viewing screen or camera and b) imaging mode, which projects an image of the sample onto the screen or camera. In diffraction mode, a selected-area (SA) aperture may be used, the objective aperture is removed, and the intermediate lens selects the back focal plane of the objective lens as its object. In imaging mode, the objective aperture is inserted, the SA aperture is removed, the intermediate lens selects the image plane of the objective lens as its object. *Figure reprinted with permission from Springer Science+Business Media: David B. Williams and C. Barry Carter. "The Instrument". In: Transmission Electron Microscopy. Boston, MA: Springer US, 2009, pp. 141–171. Copyright Springer US.*

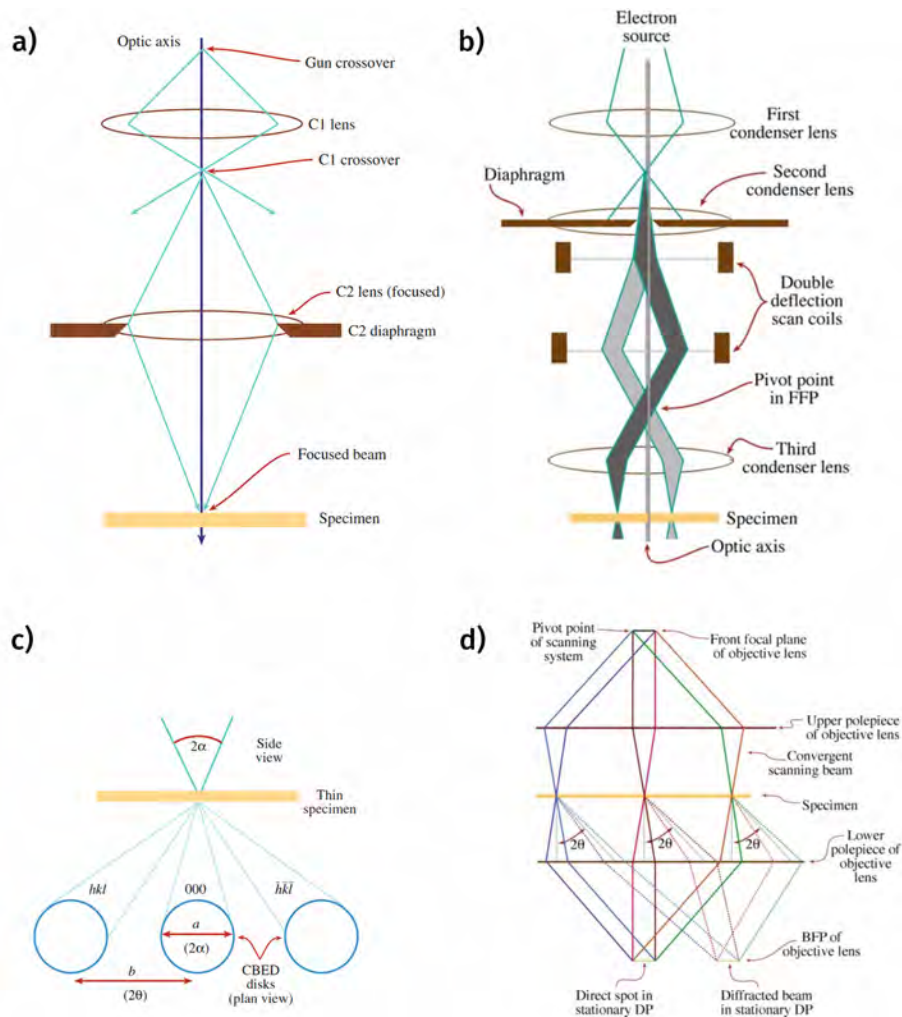


Figure 1.4: Schematics of TEM diffraction in STEM mode. a) Ray diagram of a converged STEM probe. b) Scanning the convergent probe for STEM image formation using two pairs of scan coils to ensure that the probe remains parallel to the optic axis as it scans across the specimen. c) Schematic of converged probe STEM diffraction disks, whose width is proportional to the beam convergence angle, α . d) Ray diagram depicting the creation of a convergent-beam diffraction pattern in the back focal plane of the objective lens. *Figures adapted with permission from Springer Science+Business Media: David B. Williams and C. Barry Carter. Transmission Electron Microscopy. Boston, MA: Springer US, 2009. Copyright Springer US.*

spots are obtained when the beam is most parallel. The diffraction spots become larger and more diffuse if the beam is condensed (CBED). The trade-off, of course, is between the spatial resolution and the precision of any structural measurements. This balance will also be discussed in later sections.

EDS, EELS

Chemical analysis is a very useful addition to a TEM setup. Energy dispersive x-ray spectroscopy (EDS or EDX) and electron energy-loss spectroscopy (EELS) detectors can be added to a TEM configuration and coupled with a HAADF detector for simultaneous imaging. Broadly, EDS works by taking advantage of the unique fingerprint of electron energy differences in atomic and molecular orbitals. As the sample is bombarded with electrons from the TEM probe, core-shell electrons in the sample are occasionally excited, and as an electron fills that ground state, it releases a photon (typically an X-ray) of a characteristic wavelength. The EDS camera will be placed above the sample stage, off-axis from the electron beam. Lateral resolution is typically on the order of nanometers, with an elemental sensitivity of 0.1-0.5 wt%.

By contrast, an EELS detector is placed below the specimen in the TEM column in order to measure the electrons' kinetic energy lost to inelastic collisions with the sample. This method is capable of measuring energy losses from excited phonons and plasmons, electron transitions within and between energy bands, inner shell ionizations, and even Cherenkov radiation. Like EDS, EELS can determine atomic composition based on the inner shell ionization energies, but it has an advantage in sensitivity for lighter elements.

1.7 Diffraction: Reciprocal space

This section briefly outlines the foundations of electron diffraction analysis, including special considerations for thin films and nanoparticles.

Diffraction patterns are created when an electron beam passes through a material and the electrons are deflected by the electron clouds and nuclei of that material. This is a Coulomb interaction, where the negatively-charged electrons are repulsed or attracted by the electron clouds and atomic nuclei, respectively, making electron diffraction a fundamentally different interaction from X-ray diffraction or neutron

diffraction.

Diffraction analysis relies on an understanding of reciprocal space. Reciprocal space is a constructed 3-dimensional space that describes the Fourier transform of a spatial function, or in real terms, of the atom positions or lattice vectors of a crystal. For a full derivation of the construction of this space, see references [41] and [42].

The diffraction pattern which is formed in the back focal plane of the microscope's objective lens is a result of constructive interference from the diffracted wavefunctions. The Laue equation expresses this simple condition for constructive interference:

$$\vec{K} = \vec{g} \tag{1.2}$$

where \vec{K} is the scattering vector and \vec{g} is the reciprocal lattice vector between two points in reciprocal space (see schematic in Fig. 1.6) corresponding to a particular set of planes in the real, or direct, lattice. By observation, \vec{K} must equal $\frac{2\sin\theta}{\lambda}$, and as such it can be seen that the Laue condition (Eq. 1.2) is equivalent to the familiar Bragg condition ($\lambda = 2d_{hkl}\sin\theta$)[41, 42]. Substituting this definition of \vec{K} for the left-hand side of Eq. 1.2 and the definition $\vec{g} = \frac{1}{d_{hkl}}$ for the right-hand side, we attain:

$$\frac{2\sin\theta}{\lambda} = \frac{1}{d_{hkl}} \tag{1.3}$$

This rearranges into:

$$\lambda = 2d_{hkl}\sin\theta \tag{1.4}$$

which is Bragg's law.

For ease of visualization, the Laue condition can be expressed as a geometrical construction, termed the "sphere of reflection," or the "Ewald sphere," and its intersection with lattice points in reciprocal space. The radius of the Ewald sphere is defined as the reciprocal of the wavelength of the incident wave, or $1/\lambda$. If the surface of the sphere intersects with a reciprocal lattice point, it means that the corresponding planes in the direct lattice satisfy the Laue condition and will constructively interfere, resulting in a peak in the diffraction pattern. Given that the wavelength of the accelerated electron beam is much smaller than a typical lattice spacing, the radius of the Ewald sphere will be large, and the sphere will intersect

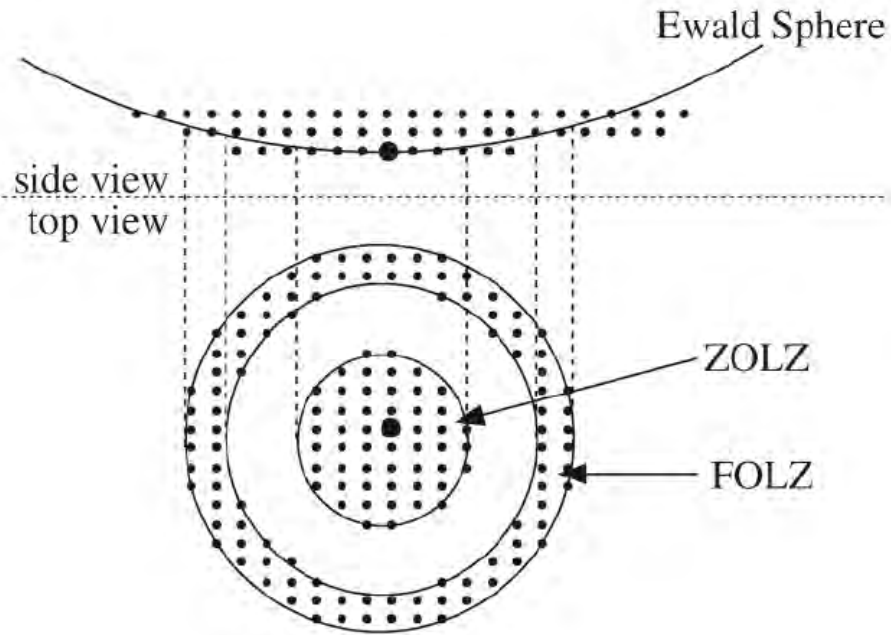


Figure 1.5: Intersections of the Ewald sphere with the reciprocal lattice of a simple cubic crystal, and two zones of bright diffraction spots. *Figure and caption adapted with permission from Springer Nature: Brent Fultz and James Howe. “Diffraction from Crystals”. In: Transmission Electron Microscopy and Diffractometry of Materials. pp. 279. Copyright Springer-Verlag Berlin Heidelberg 2013.*

with many nearby reciprocal lattice points in the same plane (Fig. 1.5).

The origin of the reciprocal lattice, the point where the transmitted (undiffracted) beam passes through, necessarily lies on the Ewald sphere. The plane containing the origin is defined as the “zero-th” order Laue zone (ZOLZ); the plane above it is the “first-order” Laue zone (FOLZ), and so on, to the second-order (SOLZ) and higher-order (HOLZ) zones. The intersection of the Ewald sphere with these planes is illustrated in Fig. 1.5.

For bulk, single-crystal materials viewed along any high-symmetry axis, the projected diffraction pattern is straightforward to predict, and conversely, to be used for crystal identification. The spacing between a lattice plane in real space, d_{hkl} , can be found by measuring the corresponding vector in reciprocal space, \vec{g}_{hkl} , and solving equation 1.5. This type of analysis is the cornerstone of electron diffraction studies.

$$d_{hkl}^2 = \frac{1}{|\vec{g}_{hkl}|^2} = \frac{1}{(\vec{g}_{hkl} \cdot \vec{g}_{hkl})} \quad (1.5)$$

Taking the square root and substituting the definition of \vec{g}_{hkl} [42]:

$$d_{hkl} = \frac{1}{|\vec{g}_{hkl}|} = \frac{1}{\sqrt{(h\vec{b}_1 + k\vec{b}_2 + l\vec{b}_3) \cdot (h\vec{b}_1 + k\vec{b}_2 + l\vec{b}_3)}} \quad (1.6)$$

where d_{hkl} is the interplanar spacing for the $\{hkl\}$ planes, \vec{g}_{hkl} is the reciprocal lattice vector, and the \vec{b} vectors are the reciprocal unit vectors.

This equation can be further specialized to a hexagonal crystal, as below:

$$\frac{1}{d_{hkl}^2} = \frac{4}{3} \frac{h^2 + hk + k^2}{a^2} + \frac{l^2}{c^2} \quad (1.7)$$

where d_{hkl} is the interplanar spacing for the $\{hkl\}$ planes, a is the lateral lattice constant, and c is the height lattice constant[43].

In thin samples, reciprocal lattice points are, appropriately, extended in the reduced dimension. A sample with little to no height – mere nanometers in the z-dimension, which is parallel to the c-axis in MoS₂ and Au – will find its reciprocal lattice points forming long rods aligned along the reciprocal c*-axis. Rather than reciprocal lattice ‘points’, we call these reciprocal lattice ‘rods’, or ‘relrods’ for short.

Electron diffraction analysis of thin films, then, has additional things to consider compared to bulk crystalline or powder samples, particularly for multi-crystalline materials such as epitaxial systems. Namely, reciprocal lattice rods from different sets of planes may simultaneously intersect the Ewald sphere, i.e., additional peaks or disks may show up in the diffraction pattern than one would expect for a given zone axis. In other words, interference from planes which do not exactly satisfy the Laue condition may still appear in a diffraction pattern, as shown in Fig. 1.6.

It should be noted that there will be entropically-favored out-of-plane distortions in any suspended ultra-thin crystal, which may alter the expected appearance of the corresponding diffraction pattern. Indeed, experimental measurements bear this out, as will be discussed in Section 4.3. In optical and electron microscopy measurements, MoS₂ areas are frequently rippled, folded, corrugated, torn, or otherwise disturbed

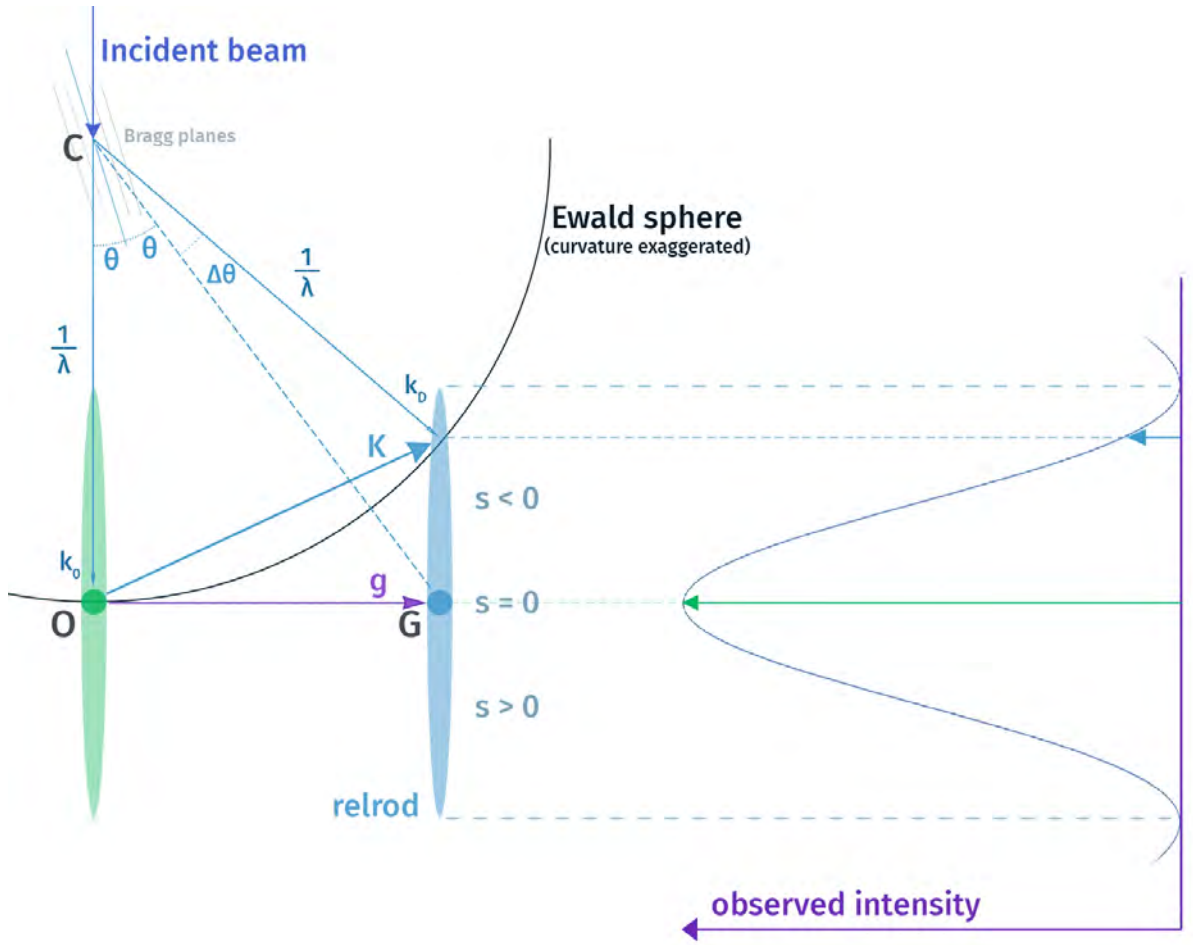


Figure 1.6: Schematic of the intersection of reciprocal lattice rods with the Ewald sphere. The incident beam is diffracted by a Bragg plane at point C . k_0 is the unscattered wavevector; k_D is the diffracted wavevector. Accordingly, K is the scattering vector. g is the reciprocal lattice vector between points O and G . s is the difference between K and g . Scattered intensity is highest when $|K| = |g|$.

from a theoretically flat 2D lattice.

Previous literature has explored the compliance of ultra-thin MoS₂[44, 45] and rippling in graphene[46, 47] and the 2D TMDCs[48]. Within a molecular layer of MoS₂, these physical distortions can stretch and compress bond lengths anisotropically across the three atomic layers.

1.8 Chapter 1 Summary

In the introductory chapter to this thesis, a brief overview of the 2D transition metal dichalcogenides (TMDCs) is offered, outlining their basic structure, highlighting recent device demonstrations, and describing the different polytypes of MoS₂. The idea of using compliant substrate epitaxy to improve monolayer selectivity in mechanical TMDC exfoliation is introduced, along with the motivating prediction of strain at the interface of the Au-MoS₂ epitaxial system. To prepare the reader for discussions in later chapters, several definitions for the different cases of epitaxy are established. This chapter also shares the history of the study of metal-TMDC epitaxial growth, and of the use of TEM analysis for characterizing such systems. Finally, background information on electron diffraction and reciprocal space, particularly as it pertains to thin films, is included.

Bibliography

- [1] Kin Fai Mak, Changgu Lee, James Hone, Jie Shan, and Tony F. Heinz. “Atomically thin MoS₂: A new direct-gap semiconductor”. In: *Physical Review Letters* 105.13 (2010), pp. 2–5. ISSN: 00319007. DOI: 10.1103/PhysRevLett.105.136805. eprint: 1004.0546.
- [2] Sujay B. Desai, Surabhi R. Madhvapathy, Angada B. Sachid, Juan Pablo Llinas, Qingxiao Wang, Geun Ho Ahn, Gregory Pitner, Moon J. Kim, Jeffrey Bokor, Chenming Hu, H. S. Philip Wong, and Ali Javey. “MoS₂ transistors with 1-nanometer gate lengths”. In: *Science* 354.6308 (2016), pp. 99–102. ISSN: 10959203. DOI: 10.1126/science.aah4698.
- [3] Patricia Gant, Peng Huang, D. Pérez de Lara, Dan Guo, Riccardo Frisenda, and Andres Castellanos-Gomez. “A strain tunable single-layer MoS₂ photodetector”. In: *Materials Today* 27.August (2019), pp. 8–13. ISSN: 18734103. DOI: 10.1016/j.mattod.2019.04.019.
- [4] Joy Cho, Matin Amani, Der Hsien Lien, Hyungjin Kim, Matthew Yeh, Vivian Wang, Chaoliang Tan, and Ali Javey. “Centimeter-Scale and Visible Wavelength Monolayer Light-Emitting Devices”. In: *Advanced Functional Materials* 1907941 (2019), pp. 1–6. ISSN: 16163028. DOI: 10.1002/adfm.201907941.
- [5] Stephen J. McDonnell and Robert M. Wallace. “Atomically-thin layered films for device applications based upon 2D TMDC materials”. In: *Thin Solid Films* 616 (2016), pp. 482–501. ISSN: 00406090. DOI: 10.1016/j.tsf.2016.08.068.
- [6] Wanshun Xia, Liping Dai, Peng Yu, Xin Tong, Wenping Song, Guojun Zhang, and Zhiming Wang. “Recent progress in van der Waals heterojunctions”. In: *Nanoscale* 9.13 (2017), pp. 4324–4365. ISSN: 20403372. DOI: 10.1039/c7nr00844a.
- [7] Daniel S Schulman, Andrew J Arnold, A L I Razavieh, Joseph Nasr, and Saptarshi Das. “The Prospect of Two-Dimensional Heterostructures”. In: *IEEE Journal of Photovoltaics* June (2017), pp. 6–17.
- [8] Sajedeheh Manzeli, Dmitry Ovchinnikov, Diego Pasquier, Oleg V. Yazyev, and Andras Kis. “2D transition metal dichalcogenides”. In: *Nature Reviews Materials* 2 (2017). ISSN: 20588437. DOI: 10.1038/natrevmats.2017.33.

- [9] Tahreem Nawz, Amna Safdar, Muzammil Hussain, Dae Sung Lee, and Muhammad Siyar. “Graphene to advanced MoS₂: A review of structure, synthesis, and optoelectronic device application”. In: *Crystals* 10.10 (2020), pp. 1–31. ISSN: 20734352. DOI: 10.3390/cryst10100902.
- [10] Mengjing Wang, Hao Li, Tae Jun Ko, Mashiyat Sumaiya Shawkat, Emmanuel Okogbue, Changhyeon Yoo, Sang Sub Han, Md Ashraful Islam, Kyu Hwan Oh, and Yeonwoong Jung. “Manufacturing strategies for wafer-scale two-dimensional transition metal dichalcogenide heterolayers”. In: *Journal of Materials Research* (2020). ISSN: 20445326. DOI: 10.1557/jmr.2020.27.
- [11] Hannah M. Gramling, Clarissa M. Towle, Sujay B. Desai, Haoye Sun, Evan C. Lewis, Vu D. Nguyen, Joel W. Ager, Daryl Chrzan, Eric M. Yeatman, Ali Javey, and Hayden Taylor. “Spatially Precise Transfer of Patterned Monolayer WS₂ and MoS₂ with Features Larger than 10⁴ μm² Directly from Multilayer Sources”. In: *ACS Applied Electronic Materials* 1 (2019), pp. 407–416. ISSN: 2637-6113. DOI: 10.1021/acsaem.8b00128.
- [12] Vu Nguyen, Hannah Gramling, Clarissa Towle, Wan Li, Der-Hsien Lien, Hyungjin Kim, Daryl C. Chrzan, Ali Javey, Ke Xu, Joel Ager, and Hayden Taylor. “Deterministic Assembly of Arrays of Lithographically Defined WS₂ and MoS₂ Monolayer Features Directly From Multilayer Sources Into Van Der Waals Heterostructures”. In: *Journal of Micro and Nano-Manufacturing* 7.4 (2019), pp. 1–8. ISSN: 2166-0468. DOI: 10.1115/1.4045259.
- [13] Sujay B. Desai, Surabhi R. Madhvapathy, Matin Amani, Daisuke Kiriya, Mark Hettick, Mahmut Tosun, Yuzhi Zhou, Madan Dubey, Joel W. Ager, Daryl Chrzan, and Ali Javey. “Gold-Mediated Exfoliation of Ultralarge Optoelectronically-Perfect Monolayers”. In: *Advanced Materials* 28.21 (2016), pp. 4053–4058. ISSN: 15214095. DOI: 10.1002/adma.201506171.
- [14] Matěj Velický, Gavin E. Donnelly, William R. Hendren, Stephen McFarland, Declan Scullion, William J. I. DeBenedetti, Gabriela Calinao Correa, Yimo Han, Andrew J. Wain, Melissa A. Hines, David A. Muller, Kostya S. Novoselov, Héctor D. Abruña, Robert M. Bowman, Elton J. G. Santos, and Fumin Huang. “Mechanism of Gold-Assisted Exfoliation of Centimeter-Sized Transition-Metal Dichalcogenide Monolayers”. In: *ACS Nano* 12.10 (Oct. 2018), pp. 10463–10472. ISSN: 1936-0851. DOI: 10.1021/acsnano.8b06101.
- [15] Cindy S. Merida, Duy Le, Elena M. Echeverria, Ariana E. Nguyen, Takat B. Rawal, Sahar Naghibi Alvillar, Viktor Kandyba, Abdullah Al-Mahboob, Yaroslav Losovyj, Khabiboulakh Katsiev, Michael D. Valentin, Chun Yu Huang,

- Michael J. Gomez, I. Hsi Lu, Alison Guan, Alexei Barinov, Talat S. Rahman, Peter A. Dowben, and Ludwig Bartels. “Gold Dispersion and Activation on the Basal Plane of Single-Layer MoS₂”. In: *Journal of Physical Chemistry C* 122.1 (2018), pp. 267–273. ISSN: 19327455. DOI: 10.1021/acs.jpcc.7b07632.
- [16] Yoshiro Kainuma. “Structure of Thin Metallic Films Formed by Evaporation on Molybdenite”. In: *J. Phys. Soc. Jpn.* 6 (1951), pp. 135–138.
- [17] Signe G. Sørensen, Henrik G. Führtbauer, Anders K. Tuxen, Alex S. Walton, and Jeppe V. Lauritsen. “Structure and electronic properties of in situ synthesized single-layer MoS₂ on a gold surface”. In: *ACS Nano* 8.7 (2014), pp. 6788–6796. ISSN: 1936086X. DOI: 10.1021/nn502812n.
- [18] Jill A. Miwa, Søren Ulstrup, Signe G. Sørensen, Maciej Dendzik, Antonija Grubišić Čabo, Marco Bianchi, Jeppe Vang Lauritsen, and Philip Hofmann. “Electronic structure of epitaxial single-layer MoS₂”. In: *Physical Review Letters* 114.4 (2015), pp. 1–5. ISSN: 10797114. DOI: 10.1103/PhysRevLett.114.046802. arXiv: 1410.0615.
- [19] Signe S. Grønborg, Søren Ulstrup, Marco Bianchi, Maciej Dendzik, Charlotte E. Sanders, Jeppe V. Lauritsen, Philip Hofmann, and Jill A. Miwa. “Synthesis of Epitaxial Single-Layer MoS₂ on Au(111)”. In: *Langmuir* 31.35 (2015), pp. 9700–9706. ISSN: 15205827. DOI: 10.1021/acs.langmuir.5b02533. arXiv: 1509.06864.
- [20] Nils Krane, Christian Lotze, Julia M. Läger, Gaël Reecht, and Katharina J. Franke. “Electronic Structure and Luminescence of Quasi-Freestanding MoS₂ Nanopatches on Au(111)”. In: *Nano Letters* 16.8 (2016), pp. 5163–5168. ISSN: 15306992. DOI: 10.1021/acs.nanolett.6b02101.
- [21] Harsh Bana, Elisabetta Travaglia, Luca Bignardi, Paolo Lacovig, Charlotte E Sanders, Maciej Dendzik, Matteo Michiardi, Marco Bianchi, Daniel Lizzit, Francesco Presel, Dario De Angelis, Nicoleta Apostol, Pranab Kumar Das, Jun Fujii, Ivana Vobornik, Rosanna Larciprete, Alessandro Baraldi, Philip Hofmann, and Silvano Lizzit. “Epitaxial growth of single-orientation high-quality MoS₂ monolayers”. In: *2D Materials* 5.3 (Apr. 2018), p. 035012. ISSN: 2053-1583. DOI: 10.1088/2053-1583/aabb74.
- [22] Nils Krane, Christian Lotze, and Katharina J. Franke. “Moiré structure of MoS₂ on Au(111): Local structural and electronic properties”. In: *Surface Science* 678.March (2018), pp. 136–142. ISSN: 00396028. DOI: 10.1016/j.susc.2018.03.015. arXiv: 1802.01380.

- [23] D. W. Pashley. “The Study Of Epitaxy In Thin Surface Films”. In: *Advances in Physics* 5.18 (1956), pp. 173–240. ISSN: 14606976. DOI: 10.1080/00018735600101175.
- [24] D. W. Pashley and M. J. Stowell. “Nucleation and Growth of Thin Films as Observed in the Electron Microscope”. In: *Journal of Vacuum Science and Technology* 3.3 (1966), pp. 156–166. ISSN: 0022-5355. DOI: 10.1116/1.1492467.
- [25] Seiichi Nagashima and Ichirou Otsuka. “Surface topography of epitaxial Au(111) films deposited on MoS₂”. In: *Journal of Crystal Growth* 146.1-4 (1995), pp. 266–270. ISSN: 00220248. DOI: 10.1016/0022-0248(94)00470-6.
- [26] Yumeng Shi, Jing Kai Huang, Limin Jin, Yu Te Hsu, Siu Fung Yu, Lain Jong Li, and Hui Ying Yang. “Selective decoration of Au nanoparticles on monolayer MoS₂ single crystals”. In: *Scientific Reports* 3.1839 (2013), pp. 1–7. ISSN: 20452322. DOI: 10.1038/srep01839.
- [27] Ruichun Luo, Wen Wu Xu, Yongzheng Zhang, Ziqian Wang, Xiaodong Wang, Yi Gao, Pan Liu, and Mingwei Chen. “Van der Waals interfacial reconstruction in monolayer transition-metal dichalcogenides and gold heterojunctions”. In: *Nature Communications* 11.1011 (2020), pp. 1–12. ISSN: 2041-1723. DOI: 10.1038/s41467-020-14753-8.
- [28] Maciej Dendzik, Matteo Michiardi, Charlotte Sanders, Marco Bianchi, Jill A. Miwa, Signe S. Grønberg, Jeppe V. Lauritsen, Albert Bruix, Bjørk Hammer, and Philip Hofmann. “Growth and electronic structure of epitaxial single-layer WS₂ on Au(111)”. In: *Physical Review B - Condensed Matter and Materials Physics* 92.24 (2015), pp. 1–7. ISSN: 1550235X. DOI: 10.1103/PhysRevB.92.245442. arXiv: 1509.05133.
- [29] Yuzhi Zhou, Daisuke Kiriya, E. E. Haller, Joel W. Ager, Ali Javey, and D. C. Chrzan. “Compliant substrate epitaxy: Au on MoS₂”. In: *Physical Review B* 93.5 (Feb. 2016), p. 054106. DOI: 10.1103/PhysRevB.93.054106. arXiv: 1505.07505.
- [30] Haoye Sun, Eric W. Sirott, James Mastandrea, Hannah M. Gramling, Yuzhi Zhou, Max Poschmann, Hayden K. Taylor, Joel W. Ager, and D. C. Chrzan. “Theory of thin-film-mediated exfoliation of van der Waals bonded layered materials”. In: *Physical Review Materials* 2.094004 (Sept. 2018), pp. 1–13. ISSN: 2475-9953. DOI: 10.1103/PhysRevMaterials.2.094004.

- [31] Alexander Kerelsky, Ankur Nipane, Drew Edelberg, Dennis Wang, Xiaodong Zhou, Abdollah Motmaendadgar, Hui Gao, Saien Xie, Kibum Kang, Jiwoong Park, James Teherani, and Abhay Pasupathy. “Absence of a Band Gap at the Interface of a Metal and Highly Doped Monolayer MoS₂”. In: *Nano Letters* 17.10 (2017), pp. 5962–5968. ISSN: 15306992. DOI: 10.1021/acs.nanolett.7b01986.
- [32] Ryozi Uyeda. “Cathode-ray Investigation of Thin Layers Formed Single Crystals”. In: *Proceedings of the Physico-Mathematical Society of Japan* 24.33 (1942), pp. 809–817.
- [33] D. W. Pashley. “The observation of dislocations in thin single crystal films of gold prepared by evaporation”. In: *Philosophical Magazine* 4.39 (1959), pp. 324–335. ISSN: 00318086. DOI: 10.1080/14786435908233344.
- [34] D. W. Pashley, M. J. Stowell, M. H. Jacobs, and T. J. Law. “The growth and structure of gold and silver deposits formed by evaporation inside an electron microscope”. In: *Philosophical Magazine* 10.103 (1964), pp. 127–158. ISSN: 00318086. DOI: 10.1080/14786436408224212.
- [35] Yuan Cao, Valla Fatemi, Shiang Fang, Kenji Watanabe, Takashi Taniguchi, Efthimios Kaxiras, and Pablo Jarillo-Herrero. “Unconventional superconductivity in magic-angle graphene superlattices”. In: *Nature* 556.7699 (2018), pp. 43–50. ISSN: 14764687. DOI: 10.1038/nature26160.
- [36] Chenhao Jin, Emma C. Regan, Aiming Yan, M. Iqbal Bakti Utama, Danqing Wang, Sihan Zhao, Ying Qin, Sijie Yang, Zhiren Zheng, Shenyang Shi, Kenji Watanabe, Takashi Taniguchi, Sefaattin Tongay, Alex Zettl, and Feng Wang. “Observation of moiré excitons in WSe₂/WS₂ heterostructure superlattices”. In: *Nature* 567.7746 (2019), pp. 76–80. ISSN: 14764687. DOI: 10.1038/s41586-019-0976-y. arXiv: 1812.09815.
- [37] Fang Liu, Wenjing Wu, Yusong Bai, Sang Hoon Chae, Qiuyang Li, Jue Wang, and James Hone. “Disassembling 2D van der Waals crystals into macroscopic monolayers and reassembling into artificial lattices”. In: *Science* 367 (2020), pp. 903–906. DOI: 10.1126/science.aba1416.
- [38] W. A. Jesser and D. Kuhlmann-Wilsdorf. “Measurement of elastic strains in small gold nuclei on molybdenite substrates as a function of nucleus size and misalignment”. In: *Journal of Applied Physics* 38.13 (1967), pp. 5128–5131. ISSN: 00218979. DOI: 10.1063/1.1709289.

- [39] Anna C. Domask, Kayla A. Cooley, Bernd Kabius, Michael Abraham, and Suzanne E. Mohny. “Room Temperature van der Waals Epitaxy of Metal Thin Films on Molybdenum Disulfide”. In: *Crystal Growth and Design* 18.6 (2018), pp. 3494–3501. ISSN: 15287505. DOI: 10.1021/acs.cgd.8b00257.
- [40] Yinghui Sun, Haofei Zhao, Dan Zhou, Yuchen Zhu, Huanyu Ye, Yan Aung Moe, and Rongming Wang. “Direct observation of epitaxial alignment of Au on MoS₂ at atomic resolution”. In: *Nano Research* 12.4 (2019), pp. 947–954. ISSN: 19980000. DOI: 10.1007/s12274-019-2329-4.
- [41] Brent Fultz and James Howe. “Diffraction from Crystals”. In: 2013, pp. 237–288. DOI: 10.1007/978-3-642-29761-8_6.
- [42] David B. Williams and C. Barry Carter. “Thinking in Reciprocal Space”. In: *Transmission Electron Microscopy*. Boston, MA: Springer US, 2009, pp. 211–219. DOI: 10.1007/978-0-387-76501-3_12.
- [43] Jian Min Zuo and John C.H. Spence. *Advanced Transmission Electron Microscopy*. New York, NY: Springer New York, 2017, p. 668. ISBN: 978-1-4939-6605-9. DOI: 10.1007/978-1-4939-6607-3.
- [44] Simone Bertolazzi, Jacopo Brivio, and Andras Kis. “Stretching and breaking of ultrathin MoS₂”. In: *ACS Nano* 5.12 (2011), pp. 9703–9709. ISSN: 19360851. DOI: 10.1021/nm203879f.
- [45] Andres Castellanos-Gomez, Menno Poot, Gary A. Steele, Herre S.J. Van Der Zant, Nicolás Agrait, and Gabino Rubio-Bollinger. “Elastic properties of freely suspended MoS₂ nanosheets”. In: *Advanced Materials* 24.6 (2012), pp. 772–775. ISSN: 15214095. DOI: 10.1002/adma.201103965.
- [46] Jamie H Warner, Ye Fan, Alex W Robertson, Kuang He, Euijoon Yoon, and Gun Do Lee. “Rippling Graphene at the Nanoscale through Dislocation Addition”. In: *Nano Letters* 13.10 (2013), pp. 4937–4944. DOI: 10.1021/nl402902q.
- [47] Qiang Cao, Xiao Geng, Huai peng Wang, Pengjie Wang, Aaron Liu, Yucheng Lan, and Qing Peng. “A review of current development of graphene mechanics”. In: *Crystals* 8.9 (2018). ISSN: 20734352. DOI: 10.3390/cryst8090357.
- [48] Yufei Sun and Kai Liu. “Strain engineering in functional 2-dimensional materials”. In: *Journal of Applied Physics* 125.8 (2019). ISSN: 10897550. DOI: 10.1063/1.5053795.

Chapter 2

4D Scanning Transmission Electron Microscopy

As a technique, 4D Scanning Transmission Electron Microscopy (4D STEM) involves recording a grid of electron diffraction patterns over a two-dimensional sample area, and the result is a 2D array of 2D diffraction patterns, comprising a 4D dataset as illustrated in Figure 2.1. This is distinct from “4D” techniques where some quality of a 3D sample is mapped over time, or where “phase” or another value is the fourth datum recorded in addition to the three spatial coordinates. Rather, 4D STEM is able to identify crystal species and orientations over a relatively large area (up to microns) while recording minute differences in crystal plane spacings (i.e., deformation) across the sample.

In this chapter, we will discuss the following: the applications of 4D STEM, instrumentation required for this technique, analysis methods for the characteristically large 4D STEM datasets, and our approach to open data archiving.

2.1 Introduction to 4D STEM

4D STEM is a relatively young (ca. 2006) electron microscopy technique that calls for at least two things: a transmission electron microscope with a STEM detector, and a calibrated scanning protocol. On its face, this is a process that could be done manually, and is indeed an advancement of method, not of imaging quality (e.g., resolution). By using a program to raster the beam rather than manual adjustments, experiment duration and human error are both reduced. The resulting regular array of diffraction data can then be analyzed across the real space dimensions. A significant challenge of 4D STEM lies in the rigorous analysis of this ‘Big Data’ problem, covered in section 2.3 in this chapter.

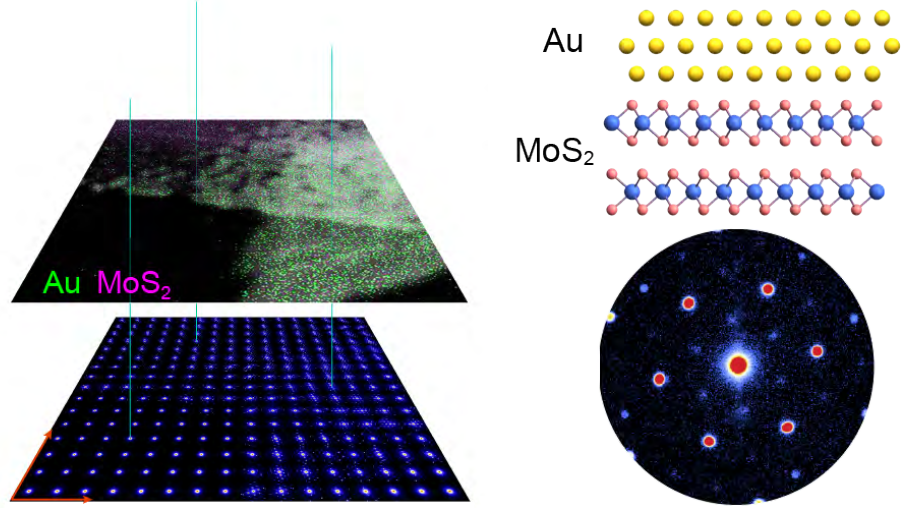


Figure 2.1: Schematic of 4D STEM data collection across a sample of epitaxial Au on MoS₂. A molecular ball-and-stick model is shown above a representative diffraction pattern, color-scaled to illustrate the high dynamic range.

Several recent technological advancements have given rise to 4D STEM as a newly popular experimental protocol. First, the emergence of high-performance electron detectors, such as monolithic active pixel sensors (APS) and hybrid pixel array detectors (PAD). Second, new computational methods and code repositories for 4D STEM analysis are currently under development with the immediate goal of integrating into TEM operational software. One of these repositories, py4DSTEM[1], will be discussed in this work.

Scientific aims well-suited to 4D STEM include crystal orientation mapping, evaluating strain landscapes, and quantifying medium-range (as opposed to only short-range) order, as well as a number of phase contrast imaging techniques. The strength of the approach is that it allows for a quasi-continuous mapping of crystallographic features in real space. The resulting datasets have a richness over and above that of single measurements taken at disjointed locations (where no position data is relevant or even recorded), and yields more insights than data acquired using line profile techniques. For example, in polycrystalline samples, grain size and grain boundary orientations can be directly ascertained using 4D STEM without the need for real-space imaging in high-resolution. Similarly, small and localized strains can be accu-

rately measured across a sample without using a proxy method or atomic-resolution imaging.

Like other TEM methods, 4D STEM is not ideal for studying materials that are sensitive to an accelerated electron beam. Biological materials and those which have embedded or thick structures are not ideal specimens for TEM studies without certain accommodations, such as using cryo- or low-dose TEM for the former and performing cross-sectional TEM (using a focused ion beam to obtain a lamellar sample) for the latter.

At present, 4D STEM protocols do not generally include a tilt or focal component; the only variable that is changed with each recorded diffraction pattern is the position of the beam on the sample. The issue with this, of course, is that these thin samples may bend across the length and width of the measured area, and diffraction patterns which may be well-aligned at the start of the scan may be significantly off-axis in another area of the scan. While this information is useful in itself, it can complicate or at least decrease the accuracy of analytical methods that ‘expect’ a consistent zone axis.

2.2 Instrumentation

This section will introduce the technical methods that comprise an informative 4D STEM experiment on a metal-TMDC system and highlight several recent improvements in electron detector technology.

Every characterization effort begins with the sample. The nature of the sample, the phenomena to be studied, and the constraints of interest will determine the experimental method, or methods, to be used. If a sample is thin, or can be made thin, such that a majority of electrons could pass through the sample, then TEM methods may be available. If the sample is atomically light-weight, or delicate (sensitive to vacuum or irradiation), or biological, or dissolved, then TEM may not be the ideal characterization avenue (though great strides have been made recently in cryo-TEM and low-dose TEM). As a class of atomically thin, semiconducting materials with reasonably heavy elements, the transition metal dichalcogenides are a good fit for TEM characterization. The transition metal disulfides like MoS₂ and WS₂ are slightly harder to characterize compared to the diselenides due to sulfur’s low atomic weight, but appropriate accommodations can be made.

In the field of characterization, a combination of complementary techniques can be more than the sum of its parts. 4D STEM is a powerful technique on its own, but it is all the more potent when coupled with real space imaging (e.g., HAADF) and compositional analysis (e.g., EDS, EELS). First, real-space imaging is crucial for navigating the sample and identifying areas for further analysis. Bright-field or dark-field imaging is used to recognize features, study sample morphology and density, and learn the relative positions of features, including along the beam direction (determined by focus). Since the Z-contrast mechanism allows for some ambiguity in whether a given area is thicker or simply heavier (in atomic weight), chemical analysis methods such as EDS are a straightforward and complementary way to distinguish between these possibilities. Chemical analysis also serves to confirm the sample identity and reveal any contaminants.

The 4D STEM experimental setup is equivalent to that used for electron ptychography, precession electron diffraction, and multi-beam electron diffraction (MBED-STEM) as recently described by Ophus *et al* and Hong *et al*[2, 3]. Essentially, electron diffraction patterns are collected at regular spatial intervals across a sample. To collect meaningful 4D STEM data, a suitable microscope is desired, with spatial resolution on the order of 0.5 Å and diffraction resolution below the specimen lattice constant. When operating a TEM, a thermionic field-emission electron gun emits electrons using a filament, either tungsten or lanthanum hexaboride (LaB_6), and accelerates electrons to 60-300 kV, depending on the mode of operation. Most STEM experiments conducted throughout the course of this study were conducted at 300 kV in order to maximize spatial resolution.

Figure 2.2 illustrates a STEM column configurations in selected-area diffraction mode. Figure 2.3 contrasts three diffraction techniques: selected area electron diffraction (SAED or SAD), nanobeam electron diffraction (NBED-STEM), and converged-beam electron diffraction (CBED-STEM) in terms of spot size at the same camera length and phase contrast in the disks. While SAED is a parallel-beam technique, NBED and CBED utilize a converged probe.

2.2.1 The right electron detector is critical for 4D STEM

Developments in electron detector technology, particularly in the past decade, have made possible the recent takeoff of 4D STEM experiments in the microscopy com-

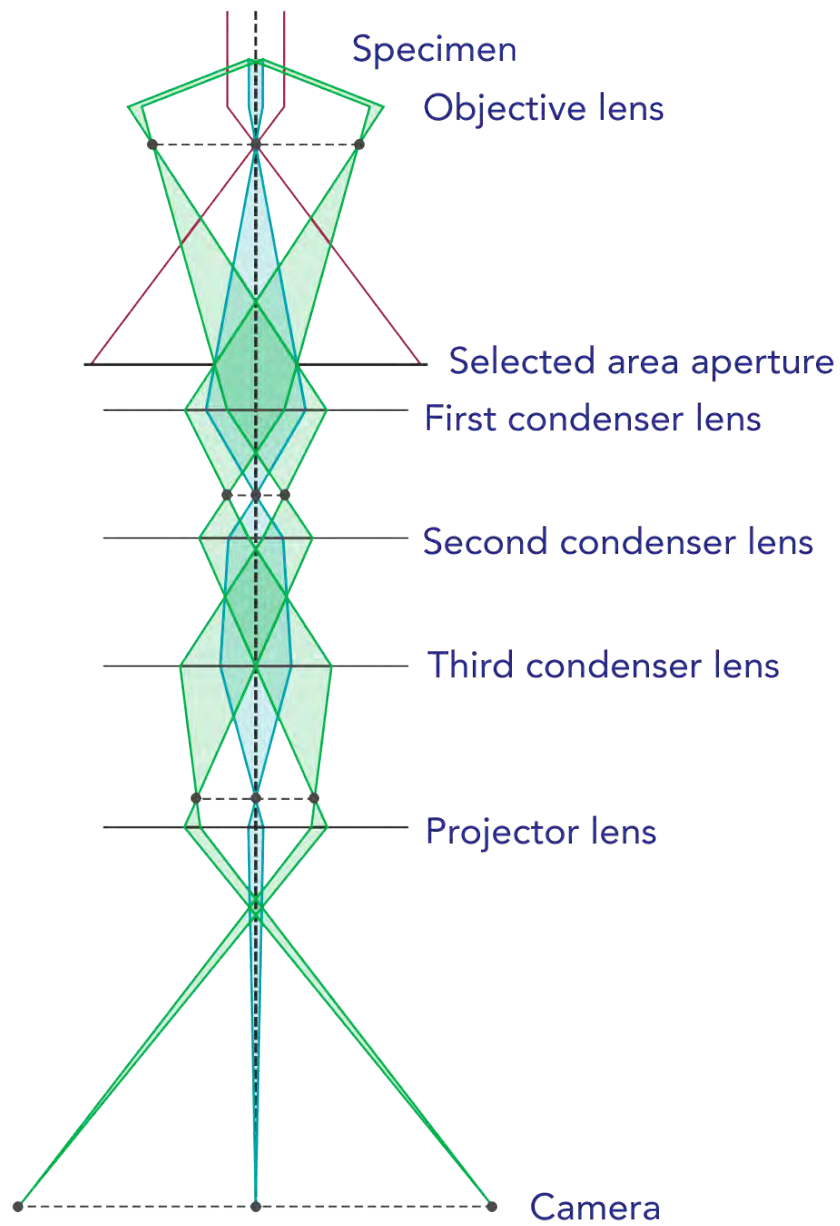


Figure 2.2: Diagram of a TEM column set up in selected-area diffraction mode.

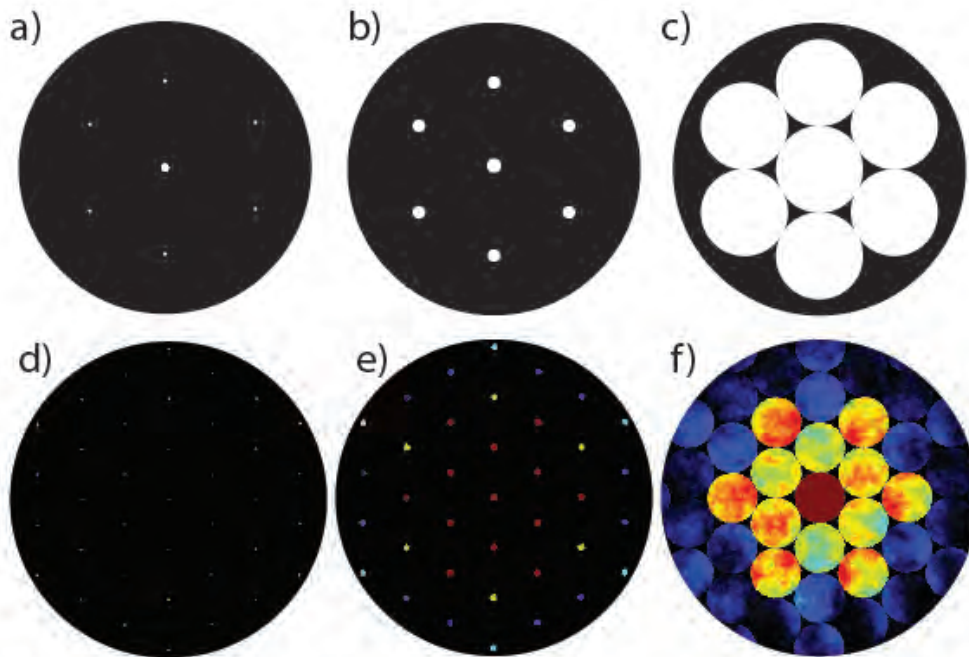


Figure 2.3: Schematic comparison between SAED (a,d), NBED (b,e), and CBED methods (c,f). The top row shows a representative spot pattern, and the bottom row shows a simulated diffraction pattern generated using the PRISM method, based on the multislice method (see section 2.3.3).

munity. Indeed, improvements to electron detectors have arguably outpaced major updates to other physical components of a typical TEM. As new leading-edge detectors gain in popularity (per the instrument update timelines and budgets of laboratories), the most widely-used electron detector is still the charge coupled device (CCD). This setup, common since the 1980s, uses a scintillator to translate the electron beam signal into photons, which then are detected by the CCD. While CCDs can be configured to be quite sensitive, as for the 4D STEM experiments in this dissertation, they will soon be replaced by detectors with an even higher dynamic range and stunningly higher speeds[4].

The ideal 4D STEM experimental setup utilizes a high-speed, high-sensitivity, high-dynamic-range detector. More modern electron detectors, such as monolithic active pixel sensors (APS) and hybrid pixel array detectors (PADs) address some weaknesses of CCD-based electron detectors.

A CCD/scintillator detector setup records one value per STEM probe position and uses segmented detectors for differential measurements. Generally, CCDs make use of 4-16 channels, though some use up to 120. The speed is limited by a video framerate: about 30-60 frames/second. By contrast, an ideal 4D STEM experiment would feature a detector that can record an image as fast as the probe itself can scan – on the order of microseconds to milliseconds per position. In fact, the current fastest electron detector in the world (87,000 fps) was developed for 4D STEM and is installed on one of the microscopes used in this dissertation[5, 6]. Early testing data using this detector was collected on some Au-MoS₂ samples I prepared for this project, although those datasets are not included here.

An APS setup uses a complementary metal-oxide-semiconductor (CMOS) chip with a doped epitaxial layer to achieve a high-speed, highly-sensitive measurement. When high-energy electrons pass through the doped epitaxial layer on the chip, low-energy electrons are ejected, collected, and measured. This detector style sometimes has issues with dynamic range, but with prescient choice of parameters, this can often be compensated for, and extraordinary speeds are possible. The stunning 87,000-fps camera mentioned above is a CMOS active pixel sensor[5].

A PAD setup uses an array of photodiodes that are bump-bonded (electrically connected via tiny balls of solder arranged in a grid) to an integrated circuit. This circuit is custom per its function, and the detector can be highly optimized for a specific microscope specification or use case. PAD detectors can be made to be highly

effective electron counters with high speed, sensitivity, and range[4, 7].

2.3 Data analysis and simulation

This section will discuss analysis approaches to take full advantage of the vast and detailed datasets produced by 4D STEM. To arrive at a particular insight, different workflows are often required; for example, a burgeoning subfield known as “ACOM” (automated crystal orientation mapping) uses 4D STEM to identify and label different crystal orientations within a sample.

Analysis of 4D STEM data is valuable both during a measurement session, in order to find areas of interest, and after the fact, in order to interpret the diffraction patterns in terms of the target inquiry. In this section, I describe the methodologies I either adapted or developed for this purpose.

2.3.1 Pre-processing in Mathematica

Wolfram Mathematica was used for initial, exploratory data analysis of 4D STEM datasets. Diffraction pattern images – or, more technically, 2D arrays of single-channel intensity data – were processed in Mathematica for much of this work. Given the high dynamic range of the data (from 0 to about 16000) and the nonlinear scaling of our own eyes, the data were normalized and adjusted for easy visual analysis. For computer analytical purposes, of course, the raw data was used.

To take stock of each new dataset, I created a graphical user interface (GUI) in Mathematica that maps diffraction patterns onto their real-space locations. The tool displays the corresponding diffraction pattern at a user-specified location on the simultaneous HAADF image (responsive to where the mouse is hovering). A screenshot of this interface is reproduced in Figure 2.4. This intuitive tool was essential for navigating thousands of diffraction patterns and observing changes with sample composition and thickness. The need for this tool arose from the sheer quantity of data, and the 4D STEM data format, which is a relatively recent one. Colleagues also recognized this need and later deployed a separate, more comprehensive GUI using python as part of the nascent py4DSTEM package[1].

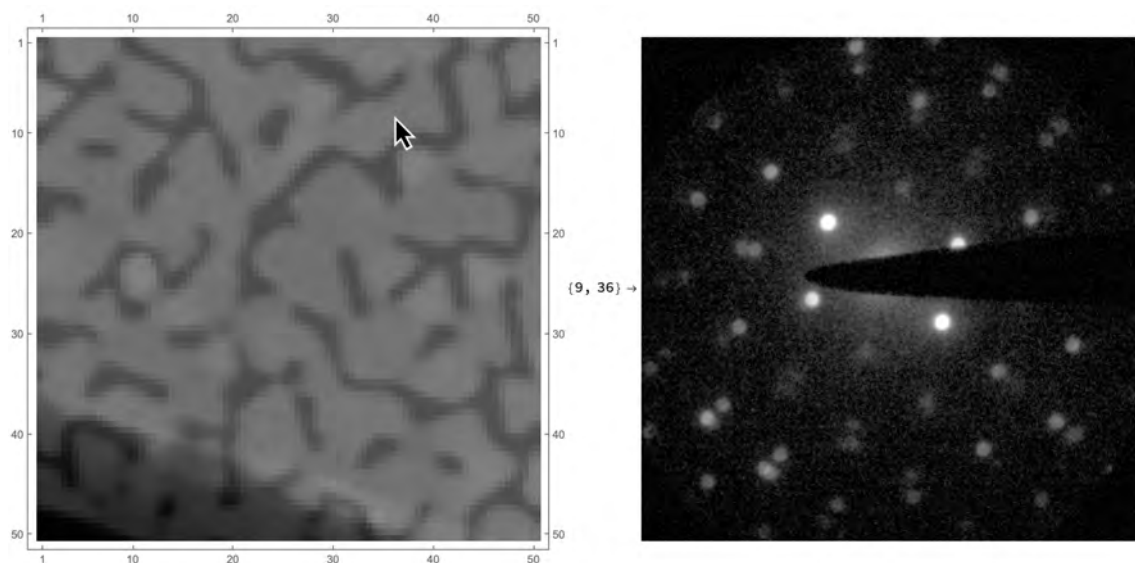


Figure 2.4: Screenshot of Mathematica tool that shows the corresponding diffraction pattern for the location where the user hovers their mouse pointer on the HAADF image.

2.3.2 py4DSTEM

py4DSTEM is a Python-based free and open-source software currently under development at Lawrence Berkeley National Laboratory for the analysis of 4D STEM data. The software has three stated goals:

1. “To make 4D-STEM data analysis easy and accessible for everyone
2. To facilitate reproducibility, even in cases of complicated or multi-step processing workflows
3. To provide a comprehensive, robust suite of 4D-STEM analysis tools, enabling high throughput, multimodal analysis in which a single dataset can simultaneously provide many distinct measurements of sample structure.” [1]

py4DSTEM is capable of measuring and mapping strains in a single crystal using diffraction patterns collected using 4D STEM.

Analyzing a dataset using py4DSTEM involves five processing steps - preprocessing, Bragg disk detection, calibration, polar transformation, and classification. The

full details can be found in Savitzky *et al.*[1]. In this section, we will touch upon Bragg disk detection and calibration, the two processes which are the most relevant in this work.

In order to detect the Bragg disks in a given diffraction pattern or set of diffraction patterns, the exact structure of the probe over vacuum must first be established. This ‘vacuum probe’ is used as a template for locating the Bragg disks in diffraction patterns taken across the sample area. The vacuum probe shape can be acquired in one of two ways: by averaging an image stack from a 4D STEM scan taken over vacuum (or, over an area of vacuum within an experimental 4D STEMscan), or by generating a synthetic probe, though “real” data is always preferred.

Next, a kernel is generated in order to perform a cross-correlation based on this vacuum template. The center of the diffraction pattern is found, either by detection or direct user input, and then a Gaussian function is subtracted which is wider than the probe.

In order to ensure the accuracy of the Bragg disk detection, and thus of the later strain calculations, several additional calibrations and corrections should be made. Even with an accurate probe shape acquired over vacuum, the effects of scanning drift over a large sample area (more than several tens of nanometers) must be quantified. Using py4DSTEM, for each diffraction pattern, the location of the unscattered beam is located and any shift in position from the previous diffraction pattern is recorded. These shifts are fit to a plane or a low-order polynomial and are then used to set corrected origin points in each image. The origin points are later used in analytical steps, including converting the data expression to polar coordinates.

2.3.3 Using Matlab to build a virtual crystal system and generate multislice STEM simulations

A number of Matlab scripts are useful in the analysis of microscopy data – such as those for principal component analysis and diffraction peak-finding. Matlab’s key use in this study, however, is a set of scripts that generate a user-specified virtual ‘sample’ and produce the corresponding STEM diffraction pattern using a multi-slice approach. It is relatively straightforward to calculate an accurate diffraction pattern for a given material. Diffraction patterns are essentially a 2D projection of a 3D structure, and mathematics are fully capable of describing this projection.

The inverse, however, is more challenging: determining the precise 3D structure from a single 2D projection is inherently more complex and prone to misinterpretation. This is due to the reduced dimensionality of the dataset. In theory, dissimilar 3D structures may produce identical, or practically indistinguishable, diffraction patterns. It is therefore extremely useful to be able to simulate any given crystal system and its corresponding diffraction pattern, including all possible permutations of a given system which present themselves similarly in diffraction datasets. Computational theory and molecular modeling, which require the same information about the simulated crystal system, can then be used to predict which of these permutations is most energetically favorable. In this way, the range of possibilities can be narrowed, and often, a prevailing structure can be identified.

For this work, thousands of simulated diffraction patterns were generated by first creating a virtual crystal that resembles a physical sample, projecting a potential wave through it, and solving the Schrödinger wave equation using the multislice algorithm. This algorithm can predict the scattering behavior of an electron beam when it interacts with a material, effectively conducting a virtual electron microscopy experiment.

In principle, any material can be created virtually; indeed, even unrealistic or non-physical materials can be imagined and visualized. There are two approaches to creating a virtual crystal whose analysis may yield scientific value: 1) the ideal or theoretical approach, and 2) the imperfect or “real” approach. In the latter approach lay all possible complexities, such as defects and deformations. Still, the ability to make a comparison to a perfect crystal is useful for benchmarking and validation.

The multislice algorithm is one approach to solving the Schrödinger wave equation, as opposed to the Bloch wave method. The multislice algorithm is preferred to generate simulated STEM diffraction patterns, largely because the computational power and memory requirements to use the Bloch wave approach exceeds current practical means. A key trade-off in using the multislice algorithm over the Bloch wave method is a much faster computation time in exchange for very slightly decreased accuracy. The multislice approach also relies on certain assumptions that may not prove true in all cases, or which require careful consideration when designing a virtual experiment.

The multislice algorithm makes one key assumption: namely, that the potential

is equal throughout the slice. This is a reasonable assumption in highly regular bulk samples, but may be problematic in highly disordered, heterogeneous, thin-film samples. In order to capture higher levels of complexity or disorder, the code should be adjusted to use smaller slices, but of course, this increases the computational expense.

While certainly faster than the Bloch wave method, part of what makes the multislice algorithm still so computationally expensive is the need to calculate the electron wave function at each probe position through each slice in the sample independently, that is, without sharing or reusing calculations with adjacent probe positions or parameters. A recent improvement upon this method was offered by Colin Ophus[8] called the ‘plane-wave reciprocal-space interpolated scattering matrix’ (PRISM) approach, and is described in reference [8]. Using this protocol, the STEM simulation is reformulated such that the computational load is shared between different probe configurations using an S-matrix approach. Matlab scripts initially drafted by Ophus which I customized for the simulations included in this work are provided in Appendix 6 and in the Github repositories listed there.

The workflow for generating a simulated STEM diffraction pattern using the PRISM multislice approach begins with building the crystal and defining constants. To build the crystal, little more than atomic positions and identities are required. Atomic positions can either be determined by the by the ideal unit cell and lattice constants, or by the output of a molecular dynamics or density functional theory (DFT) calculation, or by some other contrived or computational means. Fundamental constants, such as the mass of an electron, the fundamental charge, Planck’s constant, and the speed of light will be relevant to the calculation. Microscope parameters are also included in the simulation, allowing for a range of virtual experimental conditions.

2.4 Open access database archive

The raw 4D STEM data from this project is available on Box, and py4DSTEM scripts and Mathematica notebooks for pre-processing are available on Github.

We believe in open-access data and investigated best practices and what metadata to include. The necessary metadata for an electron microscopy experiment includes the following parameters: acceleration voltage, extraction voltage, emission current, magnification, defocus (distance from eucentric position), camera length, STEM ro-

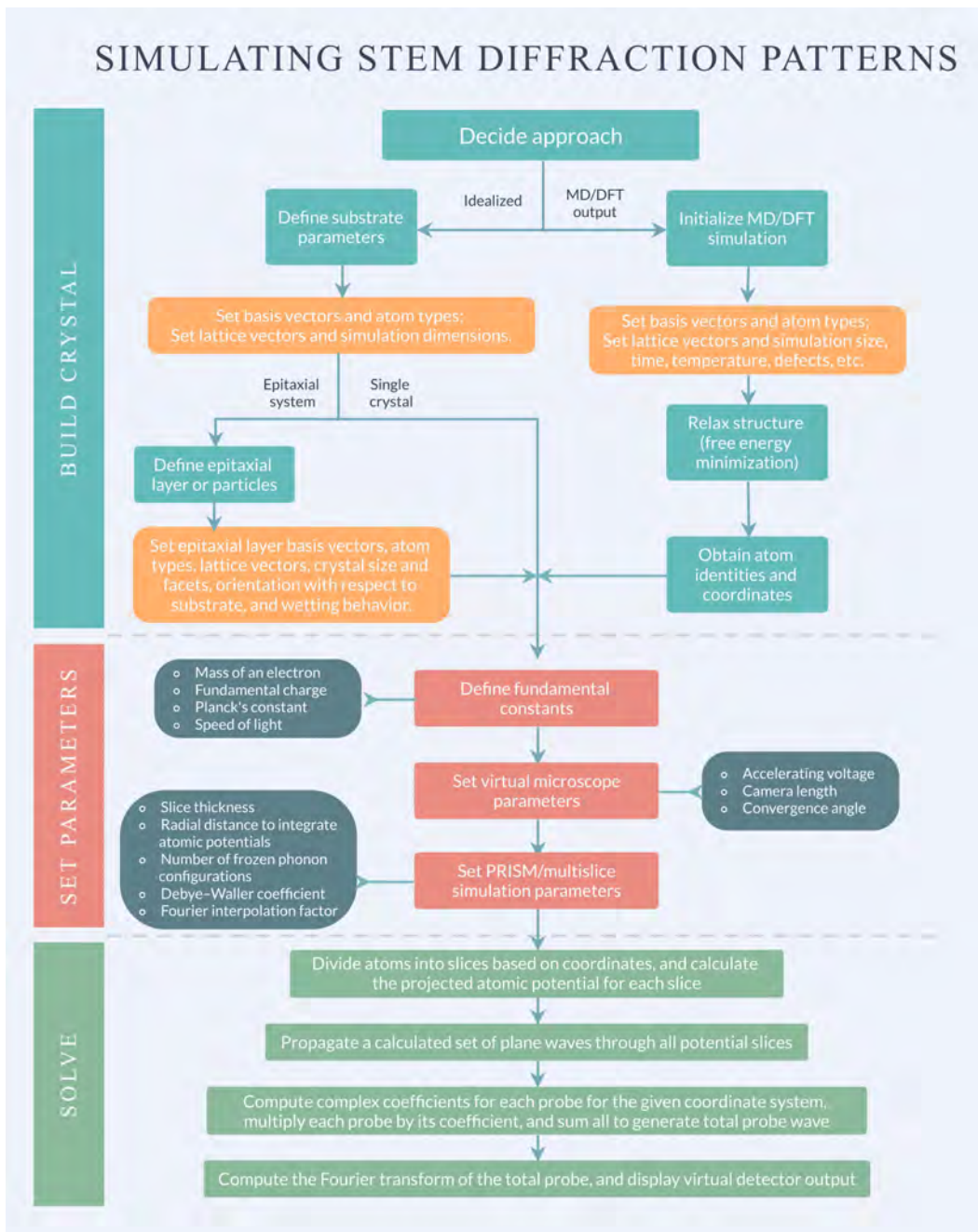


Figure 2.5: Workflow chart for generating a virtual crystal and generating simulated STEM diffraction patterns using the plane-wave reciprocal-space interpolated scattering matrix (PRISM) algorithm.

tation, convergence angle, scan dimensions, scan rate, illumination intensity, dose rate, scan duration, data size (in pixels), and pixel calibration length. These parameters are stored in the ‘.ser’ and ‘.emi’ HAADF data filetypes generated by Gatan DigitalMicrograph during data collection, and during analysis using py4DSTEM, they are stored in an ‘.h5’ filetype (hierarchical data format, HDF5).

Multi-modal diffraction, HAADF-STEM, and EDS datasets will be made publicly available immediately upon the publication of this dissertation.

Matlab and Mathematica code used to analyze datasets are available on Github at the following repository:

<https://github.com/cmtowle/4dstem>

Raw HAADF, EDS, and 4D STEM data from these investigations is available on Box in the following repository:

<https://berkeley.box.com/v/BhargavaSTEM>

2.5 Chapter 2 Summary

In this chapter, the operating principle of the 4D STEM technique is introduced, and its current analytical strengths and weaknesses are discussed. Different types of electron detectors are delineated, and the need for a fast detector for 4D STEM is emphasized. Consideration is given to this relatively new type of ‘4D’ dataset and to the data pre-processing steps and automated analysis approaches under development to analyze it. An approach to generating simulations as part of a 4D STEM analysis routine is summarized. Finally, this chapter also includes instructions to access the raw data and the code repository accompanying this dissertation.

Bibliography

- [1] Benjamin H Savitzky, Lauren A Hughes, Steven E Zeltmann, Hamish G Brown, Shiteng Zhao, Philipp M Pelz, Edward S Barnard, Jennifer Donohue, Luis Rangel DaCosta, Thomas C. Pekin, Ellis Kennedy, Matthew T Janish, Matthew M Schneider, Patrick Herring, Chirranjeevi Gopal, Abraham Anapolsky, Peter Ercius, Mary Scott, Jim Ciston, Andrew M Minor, and Colin Ophus. “py4DSTEM: a software package for multimodal analysis of four-dimensional scanning transmission electron microscopy datasets”. In: (2020), pp. 1–32. DOI: 10.1017/S1431927621000477. arXiv: 2003.09523.
- [2] Colin Ophus, Xuhao Hong, Steven Zeltmann, Karen Bustillo, Rohan Dhall, Benjamin Savitzky, Alexander Mueller, and Andrew Minor. “Recording 4D-STEM datasets at a range of beam tilts simultaneously with multi-beam electron diffraction”. In: *Microscopy and Microanalysis* 26.Suppl 2 (2020), pp. 2020–2021. ISSN: 14358115. DOI: 10.1017/S1431927620015603.
- [3] Xuhao Hong, Steven E. Zeltmann, Benjamin H. Savitzky, Luis Rangel DaCosta, Alexander Müller, Andrew M. Minor, Karen C. Bustillo, and Colin Ophus. “Multibeam Electron Diffraction”. In: *Microscopy and Microanalysis* 27.1 (2021), pp. 129–139. ISSN: 14358115. DOI: 10.1017/S1431927620024770. eprint: 2009.09134.
- [4] Colin Ophus. “Four-Dimensional Scanning Transmission Electron Microscopy (4D-STEM): From Scanning Nanodiffraction to Ptychography and Beyond”. In: *Microscopy and Microanalysis* 2019 (2019), pp. 563–582. ISSN: 14358115. DOI: 10.1017/S1431927619000497.
- [5] Jim Ciston, Ian J. Johnson, Brent R. Draney, Peter Ercius, Erin Fong, Azriel Goldschmidt, John M. Joseph, Jason R. Lee, Alexander Mueller, Colin Ophus, Ashwin Selvarajan, David E. Skinner, Thorsten Stezelberger, Craig S. Tindall, Andrew M. Minor, and Peter Denes. “The 4D Camera: Very High Speed Electron Counting for 4D-STEM”. In: *Microscopy and Microanalysis* 25.S2 (2019), pp. 1930–1931. ISSN: 1431-9276. DOI: 10.1017/s1431927619010389.

- [6] Peter Ercius, Ian Johnson, Hamish Brown, Philipp Pelz, Shang-Lin Hsu, Brent Draney, Erin Fong, Azriel Goldschmidt, John Joseph, Jason Lee, Jim Ciston, Colin Ophus, Mary Scott, Ashwin Selvarajan, David Paul, David Skinner, Marcus Hanwell, Chris Harris, Patrick Avery, Thorsten Stezelberger, Craig Tindall, Ramamoorthy Ramesh, Andrew Minor, and Peter Denes. “The 4D Camera – An 87 kHz Frame-rate Detector for Counted 4D-STEM Experiments”. In: *Microscopy and Microanalysis* 26.S2 (2020), pp. 1896–1897. ISSN: 1431-9276. DOI: 10.1017/s1431927620019753.
- [7] Barnaby Levin. “Direct Detectors and Their Applications in Electron Microscopy for Materials Science”. In: *Journal of Physics: Materials* (2021). ISSN: 2515-7639. DOI: 10.1088/2515-7639/ac0ff9.
- [8] Colin Ophus. “A fast image simulation algorithm for scanning transmission electron microscopy”. In: *Advanced Structural and Chemical Imaging* 3.1 (2017). ISSN: 21980926. DOI: 10.1186/s40679-017-0046-1. arXiv: 1702.01904.

Chapter 3

Detailed Methodology

This chapter covers a typical workflow for the TEM studies reported in this thesis, from sample preparation to data collection to analysis, including special considerations to ensure accuracy. The results of this workflow are reported in Chapter 4. The separate methodology for the photoluminescence study included in Chapter 5 is contained within that chapter, in section 5.3.

3.1 Sample preparation

Au-MoS₂ samples for TEM analysis were obtained by evaporating Au onto bulk MoS₂ to a mean thickness of 10 nm to 30 nm and then exfoliating onto TEM grids.

Natural, mined molybdenite crystal was obtained (eBay) and utilized as a source material for TEM samples. The molybdenite was quality-checked against a multi-layer sample fabricated by chemical vapor transport (CVT) to a thickness of about 0.2-0.3 mm, which was purchased from HQ Graphene and used as received. Multi-layer, CVT fabricated tungsten disulfide (WS₂) was also purchased from HQ Graphene and used as received. Quality was checked by using photoluminescence spectroscopy on exfoliated monolayer and bilayer samples and ascertaining the characteristic MoS₂ and WS₂ exciton peaks' presence and intensity (See Chapter 5).

To obtain a flat, thin (sub-mm) source of MoS₂, several initial tape exfoliations were performed on the natural molybdenite. Single-sided Kapton tape was lightly pressed onto the mineral and peeled off. Then, a clean strip of single-sided Kapton tape was joined with the first, sandwiching the MoS₂ in-between the adhesives, and then peeled apart. In this way, the molybdenite was divided several times until thin, macroscopically flat areas were obtained. These strips of tape were mounted to 2" by 3" glass slides, as shown in Figure 3.1, to prepare for e-beam evaporation of Au.



Figure 3.1: Kapton tape was used to exfoliate relatively flat, thin areas of natural molybdenite and mount the samples to large glass slides prior to the deposition of gold via e-beam evaporation.

10 nm to 30 nm of gold was deposited via e-beam evaporation (Veeco/Airco Temescal) at a deposition rate of 0.5-2 Å/s. The deposition rate was controlled by adjusting the filament emission current and the deposited thickness was monitored using quartz crystal microbalancing. Films were deposited at a high vacuum of 10^{-6} torr. The gold source had a purity of 99.9% and was provided by Oak Ridge National Laboratory.

Single-sided Revalpha thermal release tape (Semiconductor Equipment Corp.) was initially used to transfer the Au-MoS₂ material onto TEM grids, which was then heated on a hot plate to 120°C to release the thermal tape. However, persistent contamination from the adhesive made this method untenable, as leftover adhesive on the sample created unacceptable levels of carbon contamination in the TEM sample chamber[1]. To avoid this unnecessary contamination, the use of tape was suspended after initial experiments. This led to a change in sample preparation

methods wherein Au-MoS₂ was thereafter sheared onto TEM grids using friction. The shear force cleaving method was utilized to prepare the samples that are the basis for most data presented in this thesis.

In detail, the TEM grids used were composed of an ultrathin carbon film (less than 3 nm) supported by a lacey carbon film on a 400-mesh copper grid (TedPella, Inc.). In this context, a 400-mesh grid has the following specifications: a pitch of 64 μm ; a hole width of 38 μm ; a bar width of 26 μm ; and a transmission area of 35%. The size of the holes in the ‘lacey’ carbon ranges from 1/4 μm to 5 μm .

3.2 TEM Workflow: EDS, HAADF, 4D STEM

With guidance from collaborators at the National Center for Electron Microscopy (NCEM), thin film Au-MoS₂ samples were prepared, and data were collected on a FEI TITANX 60-300 microscope at 300 kV. The HAADF detector used (Gatan, Pleasanton, CA, USA) had an inner acceptance angle, β , of 70 mrad. EDS spectra were collected using a windowless detector with a solid angle of 0.7 steradians and an energy resolution of 140 eV (Bruker, Billerica, MA, USA). The holder is a FEI EDS double-tilt holder.

For 4D STEM measurements, all recorded on the TITANX, typical areas scanned were 50 x 50 nm² to 500 x 500 nm², at step sizes from 1-10 nm, with an electron beam width (FWHM) of 2 nm. In this scanning diffraction mode, I did not observe structural changes in the sample material due to beam exposure. Some carbon build-up was observed with prolonged beam exposure, as is typical[1].

To complement diffraction data, high-resolution HAADF-STEM images were acquired using the TEAM 0.5 microscope, a double-aberration corrected microscope with a lateral resolution of 50 picometers. The detailed specifications of this microscope, which is among the best in the world, can be found in Appendix 6. Images were initially collected with an accelerating voltage of 80 kV to avoid damaging the sample from prolonged exposure to high-energy electrons at high magnifications, although this was later changed to 200 kV in order to obtain images with higher spatial resolution. Some beam damage did occur to monolayer MoS₂ while operating at that elevated voltage.

The general procedure used to collect multi-modal STEM data was the following:

	4D STEM	HAADF	EDS	EELS
Data	Diffraction pattern array	Z-contrast image	X-ray energy spectrum	Electron energy spectrum
Insight	Crystal species, orientation, and strain	Thickness and atomic weight, morphology	Elemental composition	Composition, bonding, band gap, phonons

Table 3.1: Partial table of complementary scanning transmission electron microscopy (STEM) techniques, the data they produce, and the insight available through each one.

Step 1. A suitable area is found in high-angle annular dark field mode (HAADF-STEM). Here, “suitable” means a clean area of MoS₂ with few enough layers so as to provide a good signal-to-noise ratio. In order to compare the lattice constants of monolayers with those of multilayers, MoS₂ of various thicknesses were located on the sample, and those locations logged for revisiting. For this step, the microscope was operated with an acceleration voltage of 300 kV, an extraction voltage of 4.1 kV, an emission current of 170-190 μ A, a camera length of 130-160 mm, a 2000 μ m C1 aperture and either a 40 μ m or 70 μ m C2 aperture, and with any selected area or objective apertures retracted.

In addition to the “clean” MoS₂, sample areas that had been exposed to Au evaporation were located, usually exhibiting one of two typical Au island morphologies: either separated or partially coalesced (Fig 3.2). These Au islands were grown on multilayer MoS₂ prior to exfoliation by shearing to create a thinned sample for TEM analysis. Underneath the Au is MoS₂ of differing layer thicknesses, providing a testing environment for the behavior of the Au-MoS₂ system where the Au areal density is held constant while the MoS₂ thickness varies. These locations, too, were logged for revisiting.

Step 2. Concurrent with HAADF-STEM imaging, energy dispersive x-ray spectroscopy (EDS) was utilized to check the elemental composition. While the Z-contrast mechanism of HAADF-STEM – and prior knowledge of the sample – usually provides a clear delineation between the Au and the MoS₂, EDS offers verification, a degree of quantification, and some helpful insight into the presence of any contaminants. EDS allows areas with collocated Au and MoS₂ to be positively identi-

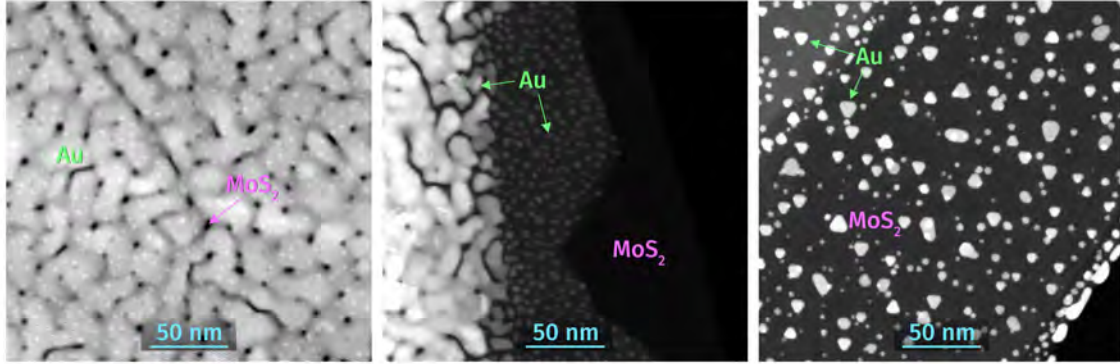


Figure 3.2: A range of Au morphologies are found to occur on MoS₂ following e-beam deposition. Left: a dense, nanoporous Au structure on MoS₂. The Au does not form a continuous film. Right: Au is seen forming an ‘island’ morphology, with epitaxial alignment and preferential faceting. These domains can occur in close proximity to one another (center).

fied. Gold was observed to grow in islands that can reach heights of more than 20 nanometers while maintaining inter-island separation of at least 3 nanometers (in other words, dozens of layers of Au atoms can be deposited non-uniformly without triggering coalescence).

Step 3. Once an area of interest is identified using HAADF-STEM and confirmed using EDS, the microscope configuration should be switched into a microprobe or nanoprobe mode, named for the reduced size of the STEM probe incident on the sample.

To capture nanobeam diffraction data, the microscope is aligned to intersect the sample with a converged probe width of 1-3 nanometers. This highly focused probe can achieve high spatial resolution in order to uncover local structural changes, although the indexing process is more difficult than in a parallel-beam condition. In a parallel beam condition, significant diffracted intensity is concentrated in the diffraction peaks, giving a high fidelity measurement of the reciprocal lattice constants, and thus, the interplanar spacings in the crystal. In a converged beam condition, this intensity is distributed in a diffraction disks, which overall appear much dimmer, and may have variations in intensity across the disk corresponding to a real-space image of the sample. Critically, it is nontrivial to locate the center of thousands of diffraction disks, as is necessary for high-throughput analysis of 4D STEM data; this

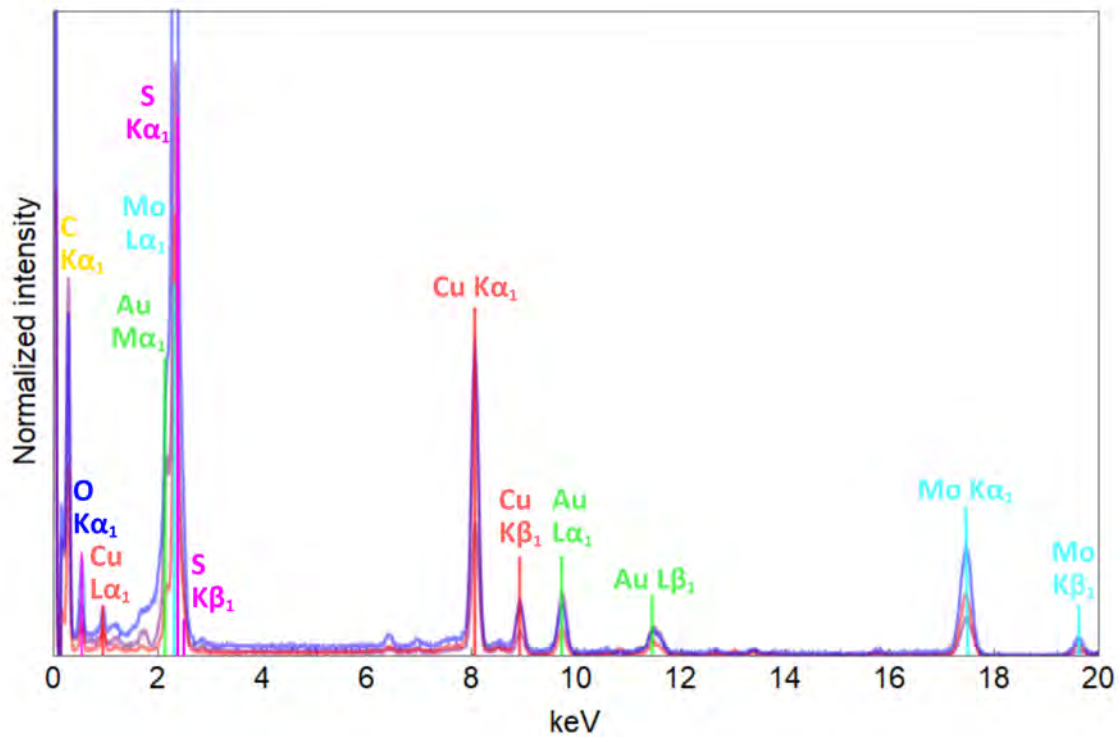


Figure 3.3: Three representative EDS spectra from two Au-MoS₂ samples. The copper and carbon peaks are due to scattering from the copper TEM grid with lacy and ultra-thin carbon supports. The relative heights of the Au and Mo peaks vary with the Au density and MoS₂ thickness in the analyzed area.

is discussed thoroughly in Chapter 4.

Most often, a 245-mm camera length was used to collect diffraction data, although this value was occasionally adjusted between 200 and 270 mm when using a circular aperture, and increased to 300 mm when using a more highly converged probe and a bullseye aperture. Generally, a convergence angle of either 0.48 or 1-1.5 mrad was used, depending on the usage of a circular aperture or bullseye aperture, respectively. When using a bullseye, or Zeltmann, aperture, a custom grating was inserted in the C2 aperture slot.

Once the microscope mode is set up appropriately to collect diffraction data, the sample can be tilted to align the beam along a high-symmetry zone axis. This step is not strictly necessary, but greatly facilitates data analysis and reduces ambiguities in the data by increasing the number and intensity of diffraction disks present in the pattern.

Finally, a custom Python script is used to raster the beam across a user-specified area with a given step size (e.g., a 50x50 scan with a 2-nm step size, covering a 100x100 nm² area).

3.3 How to approximate MoS₂ thickness using STEM

A key question throughout these studies has been whether, or the extent to which, Au epitaxy weakens the interlayer bonds of MoS₂, particularly between the top two layers, facilitating monolayer exfoliation. In determining how the presence of epitaxial Au influences the underlying MoS₂ crystal, the MoS₂ thickness, or more precisely, the number of MoS₂ layers, is highly relevant. Furthermore, when interpreting diffraction data, knowledge of the number of layers that produced the pattern would greatly inform analysis.

High-angle annular dark field (HAADF) scanning transmission electron microscopy (STEM) does not provide a means for direct measurement of sample thickness, but helpful approximations and deductions can be made which will be covered in this section. Annular dark field (ADF) imaging techniques are highly sensitive to atomic number, and exhibit a power law contrast mechanism termed ‘Z-contrast’ where the signal is proportional to the *n*th power of the atomic number, Z. Electrons are deflected more strongly by heavier atoms, and high-angle ADF techniques detect only strongly scattered electrons, explaining the source of HAADF contrast. This is an in-

tuitive and powerful model that contributes to the popularity of the STEM method. It is this contrast mechanism, for example, that has been used to assign accurate element ratios to columns of atoms in atomic-resolution HAADF images, without the need for atomic-resolution EDS, EELS, or cross-sectional TEM.

The thickness determination methods discussed in the following subsections are not the first-choice methods for ascertaining the thickness of a sample. Ideally, STM would be performed on a sample prior to TEM analysis if high-quality thickness profiles are desired[2]. The following methods are, simply, the options available *ex post facto* when HAADF data is the only type of data available.

3.3.1 Z-contrast for direct thickness measurement

In order to directly translate HAADF Z-contrast into a physical sample thickness, a reference or calibration measurement is required. This calibration sample would need to have a precise atomic thickness, known with a high degree of precision, in order to serve as an appropriate reference for HAADF Z-contrast. Further, for highest fidelity, the calibration sample and the target sample would need to be measured during the same session in order to maintain the same ambient conditions and microscope settings.

Perfect calibration samples are rare. In many cases, the materials system under study is novel in some way, and a corresponding sample with a known chemical identity and thickness is not available. Thus it is more typical to use an indirect means of thickness estimation, detailed in the following subsections.

Layered materials like MoS₂ have a particular trait that can aid in thickness estimates: layer step-edges. In HAADF mode, a step-edge appears as a discrete change in contrast, with a well-defined edge and with elemental composition held constant. In the course of these studies, MoS₂ flakes were found, with high frequency, to exhibit a tiered edge structure. While not a direct thickness measurement, it is possible to locate an extremely thin (dark) layer of MoS₂ and take advantage of the power law Z-contrast mechanism to approximately “count” the layers that comprise each step.

As a caveat, recent work points to deviations from this power law model for monolayer 2D materials including MoS₂[3]. At high accelerating voltages (e.g., 300 kV), this deviation is small but non-negligible; however, at low voltages such as 80

kV, it is much more pronounced. Therefore caution should be exercised in quantitative thickness estimates for extremely thin materials using STEM Z-contrast. As such, the thickness analysis in this dissertation relies on assuming certain parameters: namely, the power of Z (which can vary between 1 and 2), and a scaling coefficient, which must be estimated from a reference or bounded by known sample preparation parameters.

3.3.2 Attenuation of the direct beam in diffraction mode

Given the vast empty space between subatomic particles and the significant speed of accelerated electrons in a TEM, most electrons hit the detector without experiencing a scattering event. The majority of the intensity in a diffraction pattern, then, arises in the central point or spot, with a scattering semi-angle of 0 degrees.

In diffraction mode, a clear signal through vacuum (i.e., with no sample) is simply an image of the unobstructed electron beam. The full beam intensity hits the center of the detector. Adding one layer of atoms will result in a small fraction of those electrons being diffracted, creating points or disks around the direct beam with a particular symmetry and, naturally, decreasing the intensity striking the center of the detector. With every additional layer added, the intensity of the central beam is responsible for a smaller fraction of the integrated total intensity, until, at thicknesses which are no longer electron transparent, the detector reads only noise.

This phenomenon can be utilized, in reverse, to provide some information about relative sample thickness. While not a highly quantitative method, the attenuation of the direct beam is useful to the microscope operator during a session as a guide in locating thinner areas and, accordingly, in acquiring higher quality data (that is, with a higher signal-to-noise ratio).

The usual way to track thickness using the intensity of the direct beam is to employ the ratio of the diffracted peak intensity to that of the direct beam. That ratio increases monotonically, although not linearly, with thickness[4].

3.3.3 Comparative density of EDS signal

If the sample can be compared to a bulk standard, then EDS can be used to obtain the mass-thickness (and if the density is known, the actual thickness) of a sample[5]. Without such a standard, then within a single EDS map, relative signal intensity can be used as a rough proxy for thickness if the material is only expected to exist in discrete intervals (i.e., layers). This not a preferable method of thickness determination, and is often a noisier version of the same analysis available via a coupled HAADF detector, making EDS thickness analysis redundant. There is qualitative value, though, in areas where HAADF Z-contrast is unclear. For example, in compounds which have a thick area composed of a light element and a thin area composed of a heavy element, the contrast could be misleadingly similar. EDS could be helpful in clarifying the sample composition, and thereby the thickness, in these particular cases, but for most situations, EDS is not a reliable means of measuring thickness.

3.3.4 Diffraction tilt series

In reciprocal space, lattice points for extremely thin materials are extended in the c^* -dimension, forming oblong points called ‘relrods’ (for “reciprocal rods”). These relrods intersect the Ewald sphere at slight off-zone tilts, and this effect is increased by further thinning the sample. Using a set of diffraction patterns taken over a small range of tilts (e.g. one or two degrees), the incidence of additional reflections (from out-of-plane relrods) can provide a hint as to the thickness of the sample. This is a comparative means of analysis, best coupled with simulations for a more precise interpretation[6]. Without comparison to simulations, this method is difficult to use as a standalone method, as it requires either a highly uniform sample or a highly sensitive and well-calibrated tomography stage, and careful calibration of microscope parameters across all samples under consideration.

3.4 Multislice simulations of MoS_2 and the Au-MoS_2 system

If experimental diffraction data are sufficiently complicated, as they often are, then it becomes prudent to conduct ‘virtual experiments’ in order to narrow possible explanations for observed phenomena. This section will discuss the effort to model finite Au-MoS_2 epitaxial crystal systems and simulate the corresponding STEM diffraction patterns using a multi-slice simulation, aiming for a realistic alignment with my

experimental microscope parameters. An array of crystal sizes, morphologies, and strain relationships were modeled, a subset of which are displayed in Figure 3.4.

It is immediately apparent that, by definition, this effort aims to replicate, from the bottom up, a sample we had created from the top down. Put another way, the typical size of my experimental Au-MoS₂ samples was on the order of hundreds of nanometers, or even several microns, whereas system sizes in computational atomic models are already burdensome on the order of a couple dozen nanometers. This difference is not too much of a problem, except that it quickly revealed an erroneous assumption we had made: that the Au was thick enough to avoid the appearance of ‘forbidden reflections’.

It is important to note that there are truly two kinds of forbidden reflections. There are those which would ordinarily appear on a particular zone axis but are forbidden due to the structure factor of the material, and those which would not ordinarily appear, except in cases where the sample is extremely thin. In the former case, ‘extra’ spots could appear if the crystal is considered incomplete; that is, for FCC crystals, if the layer count is not an integer multiple of 3. In the latter case, nearby reciprocal lattice points now intersect the Ewald sphere due to the lengthening of rods with decreasing sample thickness. It is this latter category which was initially overlooked in the course of analyzing the diffraction patterns in this study. The use of virtual crystals and simulated diffraction patterns, created using the methodology laid out in section 2.3.3 and following the workflow in Fig. 2.5, was key to recognizing and positively identifying these anomalous Au peaks. The presence of forbidden Au reflections is further discussed in section 3.5.

3.4.1 Generating simulations of rippling and tilting in MoS₂

The perennial problem with the reduced dimensionality of diffraction data is that it is far easier to determine the 2D diffraction pattern of a 3D structure than it is to determine the 3D structure, with certainty, from a 2D diffraction pattern. The use of highly converged STEM probes is generally favored to offer more information about the 3D environment using phase information, but small-angle probes and parallel beam diffraction provide very little information about the sample’s 3D features.

Still, in simplified cases, such as a single pristine crystal, there are fewer solutions to the backwards (2D to 3D) problem, and an attempt can be made to match

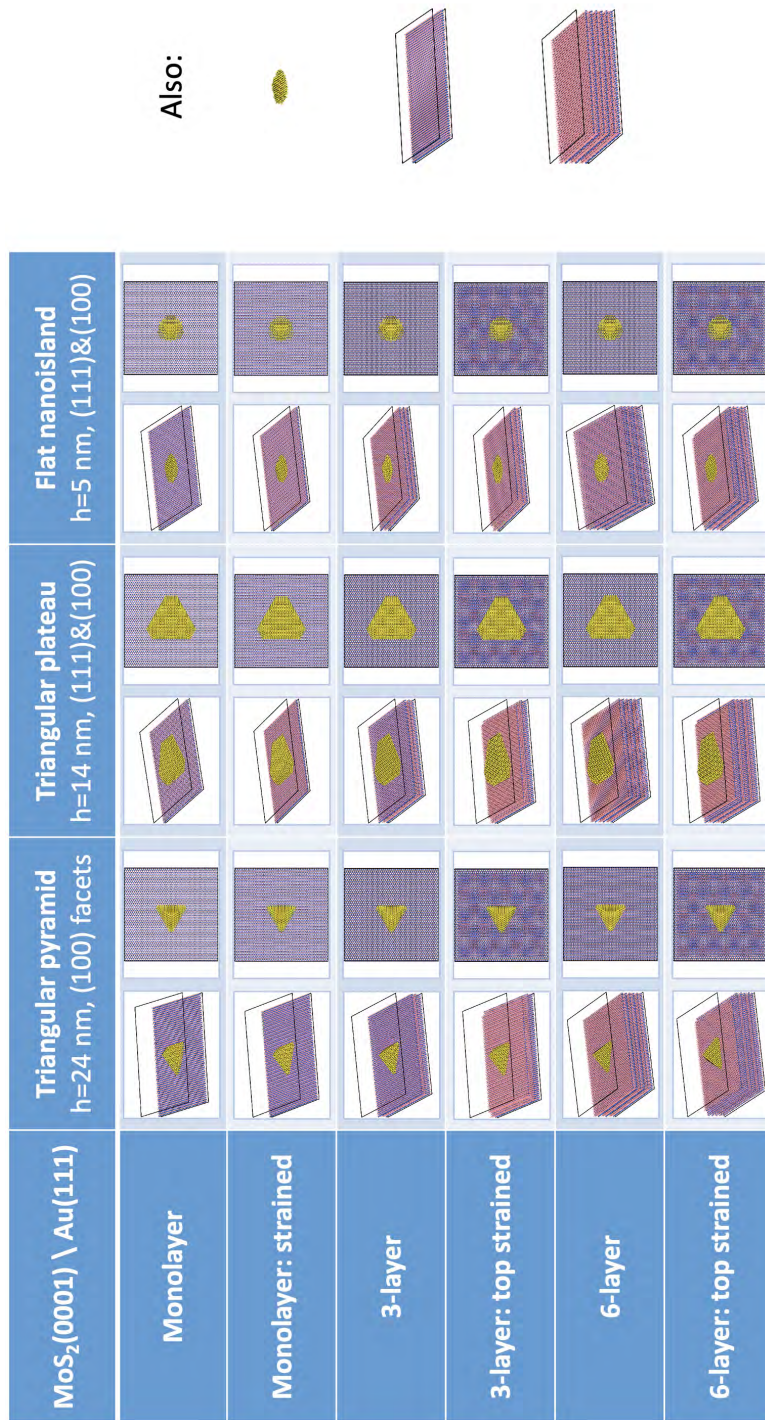


Figure 3.4: Table showing a variety a subset of virtual crystal systems for which PRISM simulated diffraction patterns were generated. Gold crystallites of various morphologies, together with 2H-MoS₂ of different layer thicknesses, are simulated together in a finite system.

experimental diffraction patterns to a generated database of simulations. Others have attempted to use χ^2 analysis and principal component analysis to perform such matches. In section A., I discuss my attempt to solve this problem using convolutional neural networks.

When building a database of simulated diffraction patterns, the boundaries and intervals used to generate this database are based, respectively, on the range of likely tilts, strains, and rotations thought to be possible in the sample, and on the accuracy to which a positive identification is needed. Appropriate simulation parameters, such as beam width, accelerating voltage, camera length, and illumination intensity are chosen to best reproduce experimental conditions. If labeled experimental data exist, those patterns may also be added to the database to improve the accuracy of the matching process.

Figure 3.5 shows a table of simulated diffraction patterns, created using a multislice algorithm to propagate a potential wave through a 250- μm piece of multilayer MoS_2 . The appearance and disappearance of certain diffraction disks, and importantly, the wide modulation in disk intensity, are the hallmarks of a sample that is undergoing tilt with respect to the intended high-symmetry zone axis.

3.5 Forbidden reflections of Au in electron diffraction

For Au(111) crystallites, observations of certain ‘anomalous’ (typically forbidden) peaks have been reported previously, in particular the $1/3\{422\}$ peaks, when Au is grown epitaxially on graphite[7] and molybdenite[8]. The same anomalous peaks have been observed in other FCC metals such as Ag, Pd, and Pt when grown on MoS_2 [9].

The forbidden peaks of Au(111) intersect the Ewald sphere very close to the MoS_2 peaks expected for this zone axis. In nanobeam electron diffraction, where we are dealing with diffraction disks, these nearby sets of disks complicate analysis of thin Au films on MoS_2 .

One set of forbidden Au diffraction disks, apparently a result of the extended relrods of the first-order Au[111] Laue zone (see section 1.7), may overlap with the nearest set of $\text{MoS}_2\{1\bar{1}00\}$ reflections when using a converged STEM probe. There is also a second set of forbidden diffraction disks from the zero-th order Laue zone of

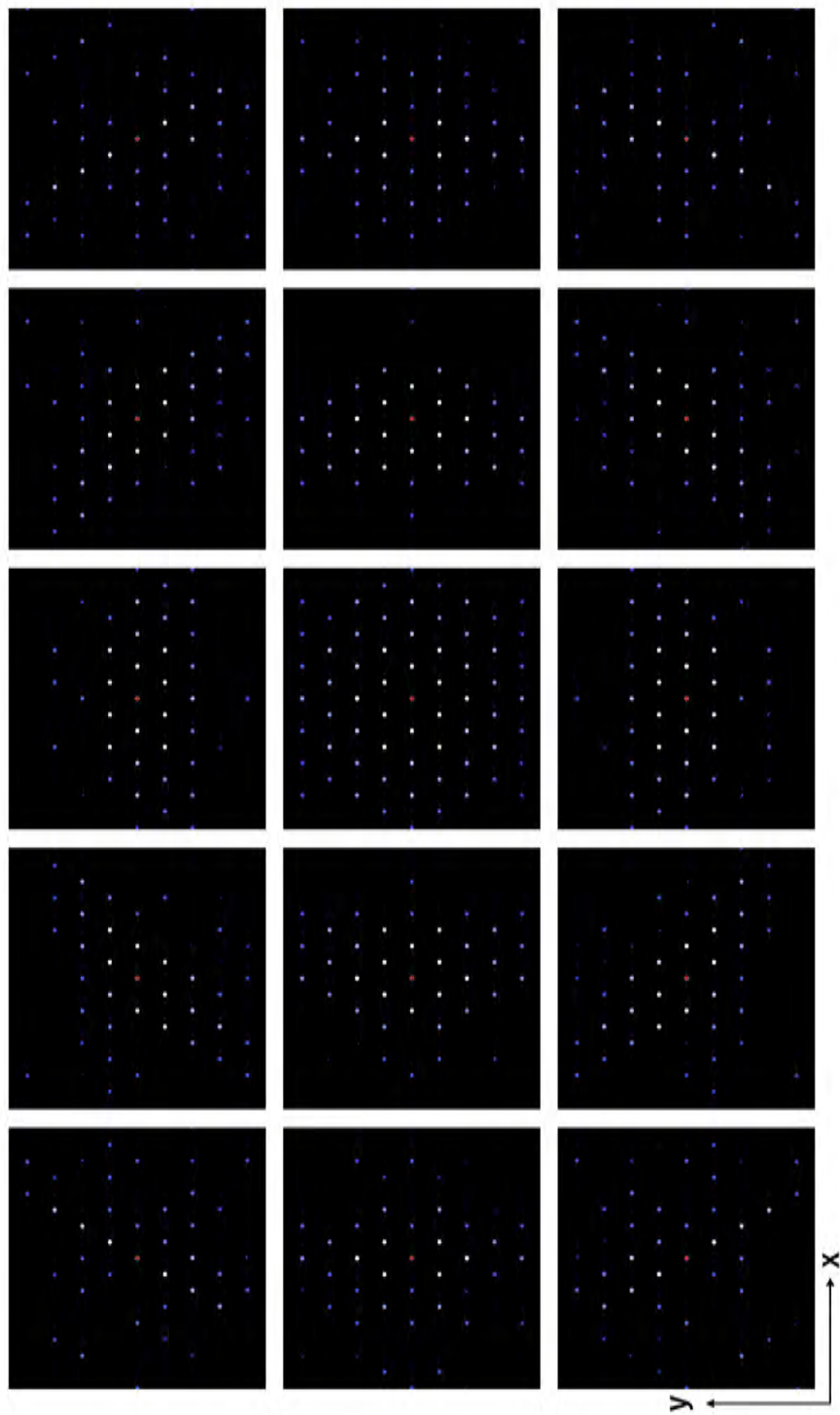


Figure 3.5: Table displaying simulated diffraction patterns as a finite virtual MoS_2 crystal is tilted about both the x- and y-axes. The center image is oriented precisely along the $\text{MoS}_2[0001]$ zone axis, and each rotational step is 3° . This simulation subset, then, sweeps from $\pm 6^\circ$ about the x-axis, and from $\pm 3^\circ$ about the y-axis. Displayed together, diffraction disks from the zero-th, first, and second-order Laue zones are readily observed.

Au[211] visible further from the unscattered beam, intersecting the Ewald sphere near the $\text{MoS}_2\{1\bar{3}20\}$ disks. A schematic drawing of the FCC reciprocal space, including the origin of these forbidden peaks, is reproduced from reference [10] in Figure 3.6. A snapshot comparison of real NBED and 4D STEM data to simulated patterns is included in Figure 3.7.

3.6 Calibration approaches for measuring strain using diffraction data

This section outlines several considerations when exploring the presence of strain in a sample using diffraction data.

First, a suitable calibration area must be found. This could be a standard sample created expressly for calibration, in which case, it is inserted into the microscope prior to examining the sample of interest, aligned along a high-symmetry zone axis, and its diffraction pattern recorded. Like standards for other characterization techniques, this necessarily means that the sample is known, pure, clean, and un-strained. Then, the known reciprocal lattice spacings can be used to determine the relationship between reciprocal length units and pixels in the diffraction image. Once this relationship is established, the sample of interest is inserted into the microscope and, using the same parameters, experimental diffraction patterns are recorded. Then, the number of pixels between diffraction disk centers can be translated into reciprocal length units, which are then used to calculate the lattice plane spacings in real space.

It is sometimes the case that a separate calibration sample is not strictly required, and for convenience an area on the sample of interest is used for self-calibration. Conservatively, this method should only be used when the sample includes a separate, easily identified, clean area with consistent composition. For example, a sample of MoS_2 which is minimally impacted by the sample preparation process may prove to be a reasonable calibration standard for another area of the sample where MoS_2 appears together with another crystal, e.g., Au. At worst, this convenient calibration method will only describe relative, rather than absolute, changes in lattice constants. This could result in a slight error in calculated strains, but would still provide a semi-quantitative description of the magnitude and direction of lattice distortions. At best, this method could provide an accurate and clear comparative analysis of changes to the crystal system, e.g., displacements in MoS_2 lattice spacings under the influence of an epitaxial Au film.

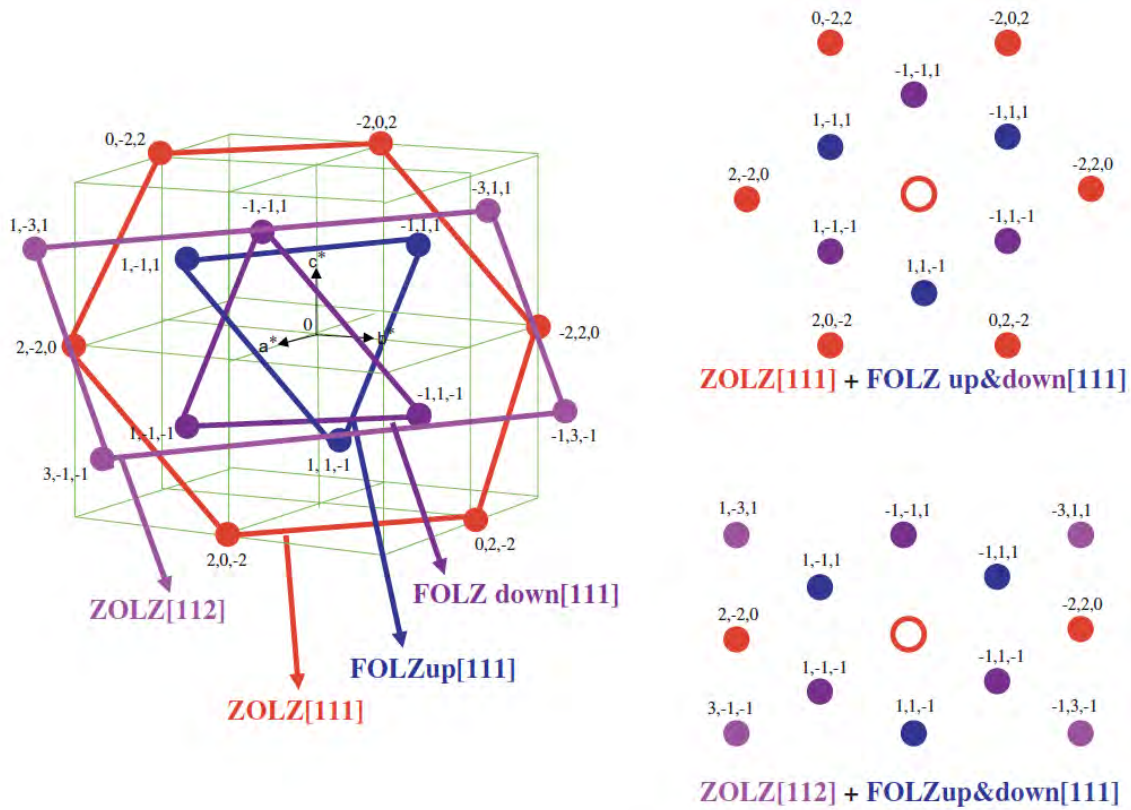


Figure 3.6: Schematic drawing of the fcc reciprocal space including the ZOLZ spots for both $[111]$ and $[112]$ zone axes and the “upper” and “lower” $\{111\}$ FOLZ spots of the (111) ZOLZ plane. As the $\{111\}$ relrods are elongated along the $[111]$ direction, they intercept both the (111) and (112) planes. They have been indexed accordingly. Thus, in the $[111]$ zone axis, the reflections indexed as $\{111\}$ are those corresponding to the $1/3\{422\}$ forbidden reflections, while in the $[112]$ zone axis they correspond to the $1/2\{131\}$ forbidden reflections. *Figure and caption reprinted with permission from Reyes-Gasga, J., Gómez-Rodríguez, A., Gao, X., and José-Yacamán, M. (2008). On the interpretation of the forbidden spots observed in the electron diffraction patterns of flat Au triangular nanoparticles. Ultramicroscopy, 108(9), 929–936, with permission from Elsevier[10].*

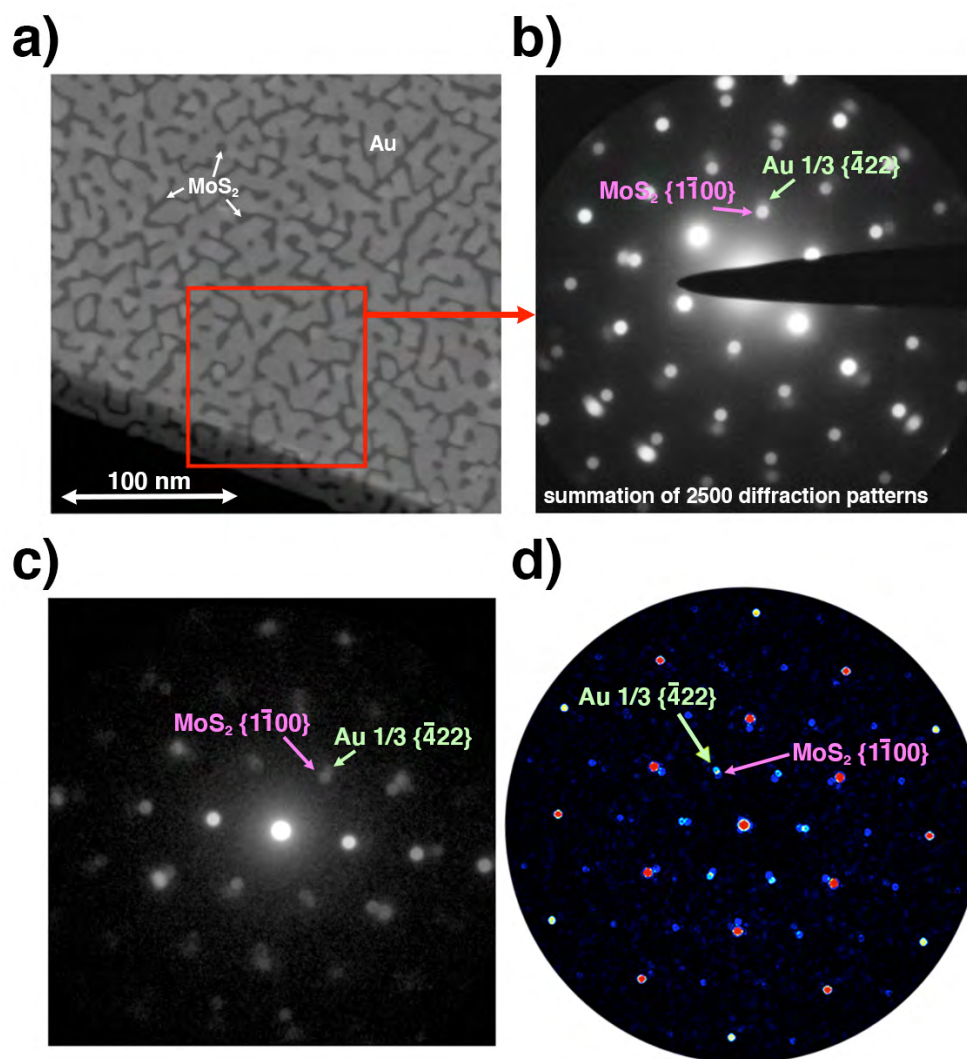


Figure 3.7: The Au 1/3{4 $\bar{2}$ 2} disks are visible in real data and simulated diffraction patterns. a) HAADF image of thin, flat, faceted Au crystallites grown on multilayer MoS₂. b) Summation of 2500 diffraction patterns from the boxed region in (a). A ‘forbidden’ Au reflection is labeled. c) A single diffraction pattern from a different area of the sample exhibiting a twist between Au and MoS₂ that also shows the ‘forbidden’ Au 1/3{4 $\bar{2}$ 2} disks. d) Simulated diffraction pattern from a virtual crystal comprised of 16 atomic layers of Au{111} on monolayer MoS₂. Here, the ‘forbidden’ Au disks exhibit a higher intensity than the nearby MoS₂{1 $\bar{1}$ 00} peaks, although thicker MoS₂ regions will result in higher intensities for those reflections.

Let us briefly rewind. Students learning how to approach an electron diffraction pattern will be taught to identify a single reciprocal space lattice and measure the lattice vectors. If one is lucky, and possesses some prior knowledge of the sample, then the distance ratios and angles between the vectors can be used to confirm the crystal identity, type, and orientation by matching these values to a standard table. But what happens if the reciprocal lattice does not readily match any known, high-symmetry orientation of the presumed sample? What if the values are close to a known value, but not exact? There are three explanations for slight differences in reciprocal lattice spacings and angles between experimental and tabulated patterns. The first which must be ruled out is distortion by the instrument itself, such as astigmatism or other uncorrected aberrations in the microscope projection. The second possible explanation is a slight misalignment along the high symmetry axis, which may change peak/disk intensities and may also introduce other overlapping reflections into the pattern, giving the effect of blurred or shifted diffraction disks. Third, the crystal could be physically deformed, as in strain (difference in lattice constant) or shear (difference in unit cell angles). Each of these explanations have their own hallmarks, and criteria for inclusion or exclusion into consideration.

If astigmatism and aberrations are known to be sufficiently corrected in the microscope, the next likely culprit of inexact lattice fitting is sample tilt away from a desirable low-index (high-symmetry) zone axis. For thin samples, while many of the same relrods may intersect the Ewald sphere and therefore appear in the diffraction pattern, the location of those intersections will be slightly shifted (see Fig. 3.8).

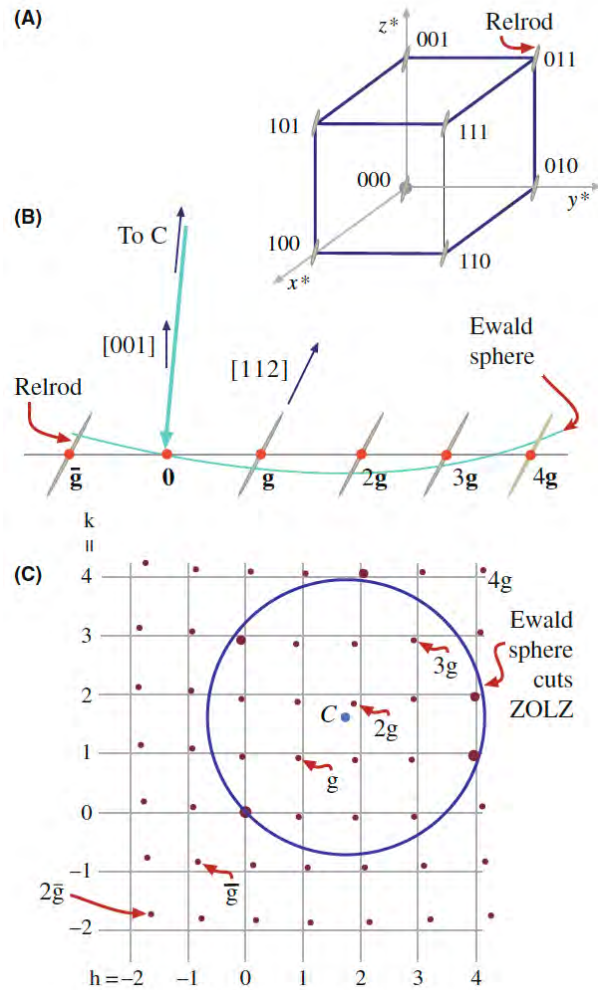


Figure 3.8: (A) For a thin specimen, every point is replaced by a relrod. (B) The Ewald sphere cutting the relrods in (A) when the crystal is tilted slightly off the (001) axis. (C) The effect of the tilt in (B) on the DP. Notice that all of the spots in the DP are displaced relative to their positions on the square grid (the projection of the spots at zero tilt), but that the magnitude of the displacement varies depending on the sign and size of s . Of course, spots on the Ewald sphere must be the ‘correct’ distance from 000. *Figure and caption reproduced with permission from Springer Science+Business Media: David B. Williams and C. Barry Carter. “Diffraction from Small Volumes”. In: Transmission Electron Microscopy. Boston, MA: Springer US, 2009, pp. 274. Copyright Springer US.*

The third explanation for a diffraction pattern which deviates from that of a known, pure, unstrained crystal is the obvious and most interesting case: the sample is not a standard specimen. Then, interplanar distances between any low-index planes not directly perpendicular to the incident beam can be calculated using Eq. 1.6. Using interplanar spacing from at least two families of planes (which are not parallel to each other), the 3D deformation tensor for the crystal can be found.

3.7 Estimating Au morphology from HAADF images

This section examines the Au morphology observed in several high-angle annular dark field (HAADF) images of the same Au-MoS₂ system. Using the Z-contrast proportionality of the HAADF images ($I \propto Z^\alpha$, where I is the HAADF intensity and Z is atomic number), a possible thickness range for nanoporous epitaxial Au is approximated. Further, variations in Au thickness are discussed in the context of the e-beam evaporation of Au onto MoS₂.

First, the Z-contrast proportionality is rearranged and expanded:

$$\text{thickness} = \frac{(\text{intensity}) * (\text{scaling factor}) * (\text{interlayer thickness})}{(\text{atomic-number-per-area})^{(\text{exponent of Z})}} \quad (3.1)$$

Eq. 3.1 was derived from discussions in references [3] and [11].

The intensity values in a HAADF image do not linearly translate into height data, if one were to attempt to convert a 2D image into a 3D one. There are two immediate problems: 1) A single transmission electron microscopy image does not directly reveal which features are ‘above’ or ‘below’ one another on the sample. In STEM mode, relative placement along the z-direction can be inferred by observing which features are in simultaneous focus, and the ‘focal distance,’ so to speak, between different features. Absent a through-focal series for each HAADF image, however, other clues may inform relative feature placement.

Knowledge of how the sample is made is naturally invaluable in interpreting the STEM data, although any assumptions must be frequently challenged. For the Au-MoS₂ samples included in this dissertation, it can be reasonably assumed that the gold is on the surface of the MoS₂, and not, say, in-between the layers to any significant degree.

The Au morphology itself is a helpful clue into the relative placement of features. In the case where there are n different layers of MoS₂, as in Figure 3.9, the continuity of Au over an apparent MoS₂ ‘edge’ could imply that the step edge is actually located on the opposing surface of MoS₂, rather than the surface in contact with gold. This edge feature may or may not influence the gold on the opposite side, but in generating a 3D map, it would not increase the height in that region (rather, it would increase the thickness of the MoS₂ by deepening the depth in that region).

In order to translate HAADF data into height information, once the relative position of certain features are reasonably known, the HAADF image must be segmented by chemical species. Since the contrast mechanism of a HAADF-STEM image is Z-contrast, which follows a roughly power-law model that increases with atomic weight, any heterogeneous image must be partitioned, then scaled, and finally re-joined (or presented separately). Any thickness analysis relying on HAADF data alone is necessarily built on many assumptions. Still, a step-by-step process for producing such a ballpark thickness estimate (Fig. 3.9) is included here:

1. Obtain raw HAADF data (the highest dynamic range possible).
2. Import into an analytical software program (such as Mathematica or ImageJ), ensuring the data is not re-scaled.
3. Partition the HAADF image into regions of presumed uniform composition. For Fig. 3.9, these regions were the following:
 - MoS₂ of thickness A
 - MoS₂ of thickness B
 - MoS₂ of thickness A with nanoporous Au
 - MoS₂ of thickness B with nanoporous Au
4. Define assumptions and limits:
 - MoS₂ is not thicker than about 200 nm, given that it was easily imaged in transmission.
 - The Au here is not thicker than about 20 nm, given that the e-beam deposition parameters set a mean thickness of 15 nm for this sample, and even with dewetting, Au covers at least 3/4 of the MoS₂ surface (measured by image segmentation). Thus, the mean thickness of the Au regions would be on the order of 20 nm.

- MoS₂ is assumed to have a constant thickness in each of the two stepped regions (A and B).
5. For regions with two or more species, isolate contrast from each species.
 - It was assumed that the nanoporous Au had the same thickness across the sample (i.e., across MoS₂ regions A and B). Therefore, the difference in contrast between the Au on the lower MoS₂ tier and the upper one was subtracted following image segmentation.
 - It was also assumed that the lower MoS₂ tier contributed linearly to the HAADF contrast (although HAADF contrast is known to be nonlinear with thickness, it is closer to linear in thinner areas[4]). Therefore, the mean contrast from the lower tier was subtracted from the segmented Au region.
 6. Calculate the cross-sectional area for single-composition areas and the atomic number per projected 2D unit cell.
 - For the MoS₂ regions, the projected 2D unit cell is a regular rhombus (interior angles of 60° and 90°) with an edge length of 3.16 Å (the *a* lattice constant of MoS₂), and the atoms contained within a single cell are one Mo atom and two S atoms. This gives a ‘Z per area’ of 8.557 e/Å².
 - For Au{111}, the projected 2D primitive cell is a regular rhombus with an edge length of 2.88 Å (the nearest-neighbor distance in FCC Au), and the atoms contained within a single cell are one Au atom. This gives a ‘Z per area’ of 14.42 e/Å².
 7. Estimate the power of Z and a scaling coefficient using the limits from step 4.
 - In this case, the power of Z was set at 1.5.
 - The maximum MoS₂ height was estimated to be between 20-200 nm. This is based on the knowledge that this sample area was not atomically thin, and yet was easily imaged in transmission. Fitting the higher tier’s contrast in the image to 200 nm, a scaling coefficient of 1300 is obtained from 3.1 .

8. Put everything together: Scale the Au contrast using the scaling factor, the Z-per-unit-area, the power of Z, and the interlayer thickness:

$$\text{thickness} = \frac{(\text{intensity}) * (\text{scaling factor}) * (\text{interlayer thickness})}{(\text{atomic-number-per-area})^{(\text{exponent of Z})}}$$

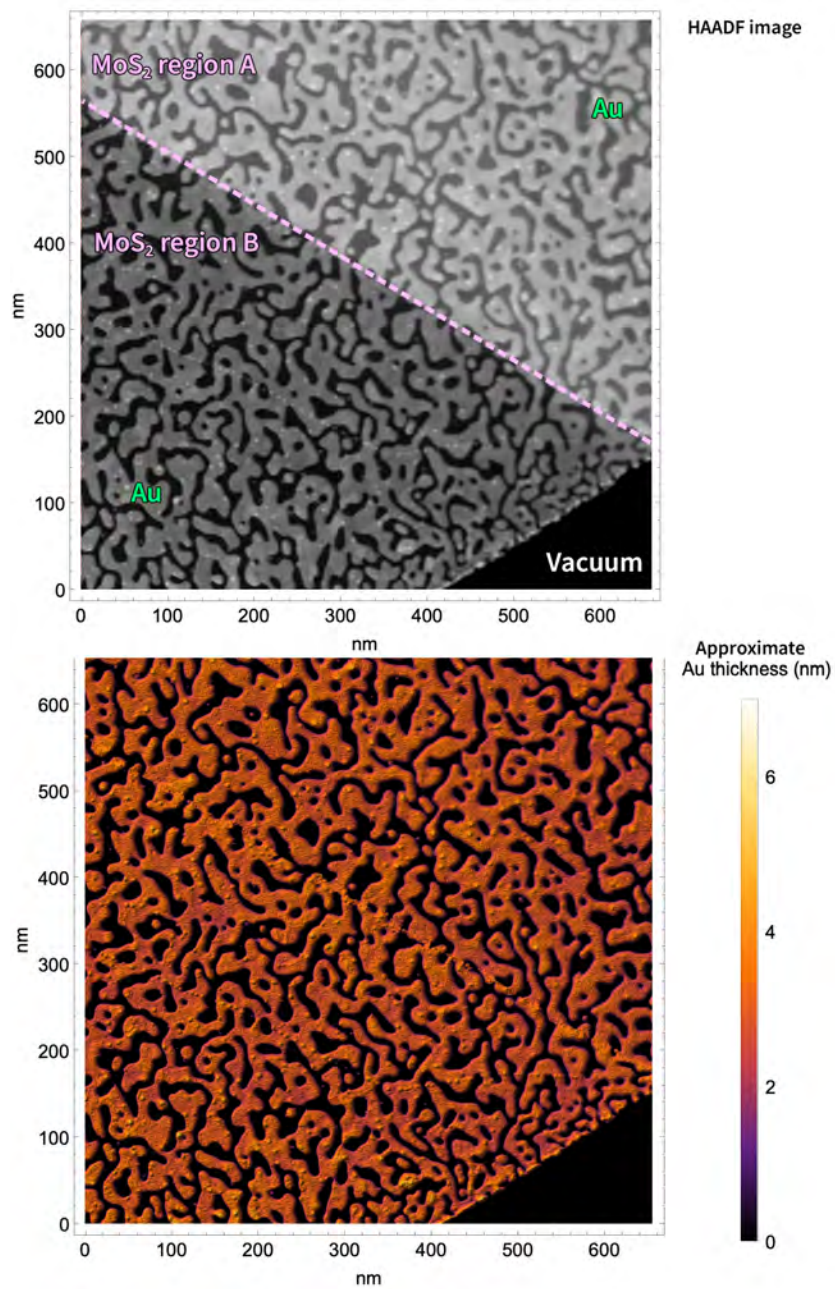


Figure 3.9: Pseudo-3D map of Au thickness from HAADF data of Au grown on MoS₂. Above: HAADF image of nanoporous Au on multi-tiered multilayer MoS₂. Bottom: Pseudo-3D map obtained by following the step-by-step workflow in section 3.7.

3.8 Moiré analysis

The rotational and lattice alignment of Au with MoS₂ can be determined, among other methods, by examination of the Moiré fringes and patterns in experimental HAADF images of the Au-MoS₂ system.

First, a word of caution: Moiré fringes, on their own, are simple evidence of two different frequencies overlapping with each other. They are an interference pattern, recognizable to anyone who has tried to take a picture of a TV or computer screen only to find a bizarre set of lines crossing the screen, caused by the difference in frequencies between the camera sensor and the TV or computer illumination. Similarly, in the case of scanning transmission electron microscopy (STEM), Moiré patterns can be caused when the scanning steps are on the same order of magnitude as a characteristic length scale in the sample. An imperfect alignment of these frequencies will produce a Moiré pattern which is purely an artifact of the STEM parameters in use.

Scanning frequency effects can be ruled out by changing microscope parameters such as magnification, scan rate, or scan direction. If the observed Moiré is persistent throughout these changes, then such fringes and patterns in dark field STEM images can reveal the mismatch, strain, or (mis)alignment of crystals even without atomic resolution imaging. Moiré superstructures also have a corresponding diffraction signature that offers additional quantitative information in k-space about the relationships observed in real space.

To measure the periodicity of the Moiré fringes, one can open an image in an analysis program such as ImageJ, Photoshop, etc. Given that the calibrated pixel-to-distance scale should be known and stored in the image metadata, the pixel distances between the fringes can be converted to real space distances. To improve precision, the line should cross several fringes at once such that the average spacing can be obtained. Of course, this can also be done by taking the Fast Fourier Transform (FFT) of the area and converting that reciprocal measurement back to a real space quantity.

Without atomic resolution, Moiré patterns in HAADF STEM images can be used to solve for one unknown variable of the following: the plane spacing of crystal A (d_A), the plane spacing of crystal B (d_B), or the angle between them (α). In the case of two dissimilar crystals (e.g., heteroepitaxy), one species' plane spacing must be known in order to find the other because the length of the Moiré period (L) only reveals the absolute difference between them, Δd :

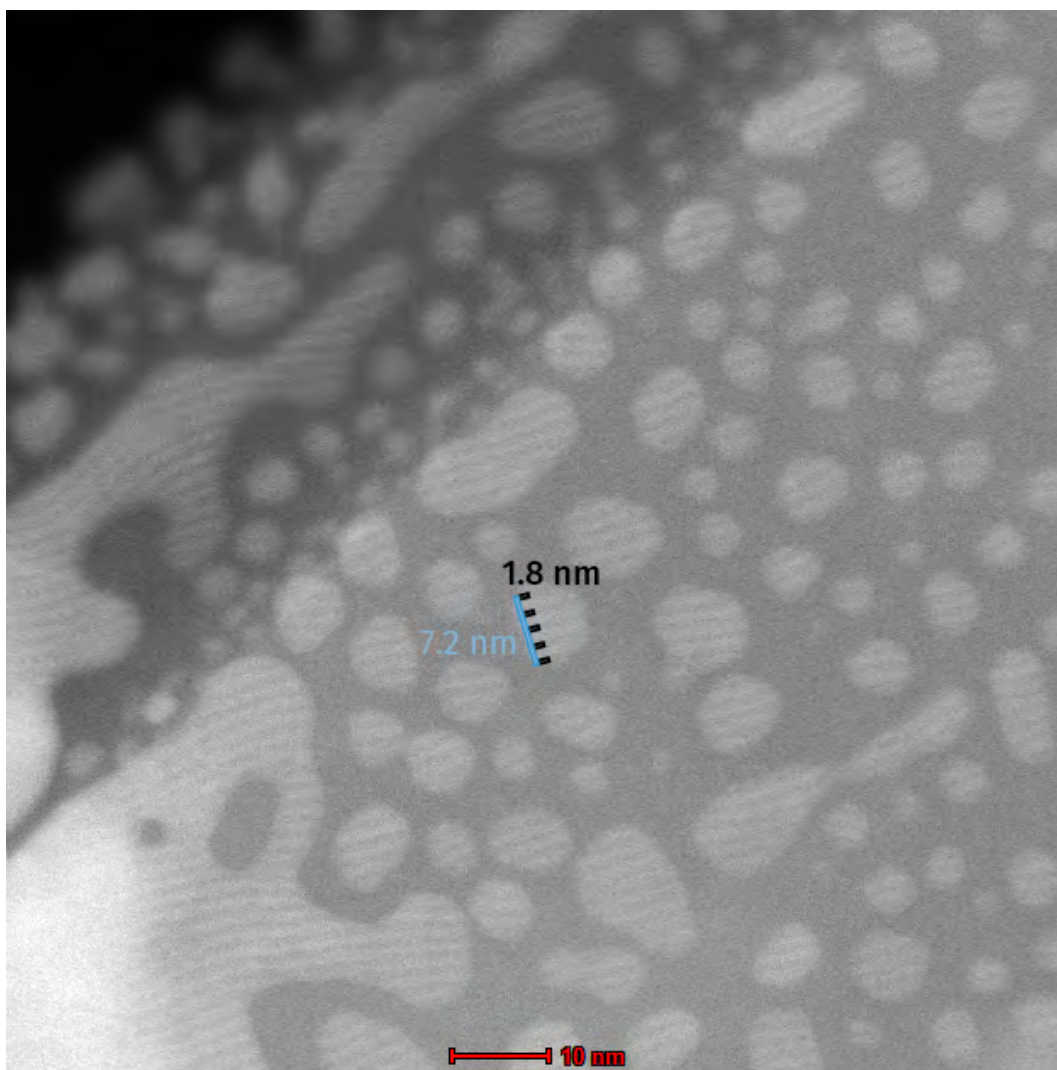


Figure 3.10: A Moiré fringe spacing of 1.8 nm is obtained from an HR-STEM image of Au deposited on MoS₂.

$$L = \frac{d_A d_B}{\Delta d} \quad (3.2)$$

In the other generalized Moiré scenario, where two like crystals are rotated azimuthally against one another, the Moiré period can reveal the rotation angle, α . Using a small-angle approximation ($\alpha < \frac{\pi}{6}$), the Moiré periodicity is related to the interplanar spacing, d , and the rotation angle, α :

$$L = \frac{d}{\alpha} \quad (3.3)$$

Without the small-angle approximation, these equations can be combined as follows:

$$L = d_A d_B \frac{\cos \alpha}{\Delta d} \quad (3.4)$$

With atomic resolution, of course, it may not be necessary to use Moiré analysis as a means to find these interplanar spacings, as they may be directly observable. However, in cases where one species is in focus while the other is out of focus, Moiré patterns can be a helpful aid in revealing the spacing of the second lattice. At least, this would be the sensible conclusion, but implementing this approach turns out to be a naïve endeavor. If we assume that both MoS₂ and Au{111} are relaxed in a given sample, as can be determined by diffraction data, then $d_A = 3.16 \text{ \AA}$ and $d_B = 2.88 \text{ \AA}$, respectively, and then we should find a Moiré periodicity of $L = 32.5 \text{ \AA}$.

STEM imaging suggests a much smaller Moiré period of only 18 \AA . Reidy *et al.* point out that this smaller periodicity, although frequently observed for this system in (S)TEM data, is the result of a projection effect, and the calculated 32.5 \AA period reflects the physical reality[12]. This projection effect arises from the AB stacking of 2H-MoS₂ and the ABC stacking of Au, a face-centered cubic crystal (Figure 3.8). Viewed along the [0001] direction, the projected 2D MoS₂ honeycomb lattice has an interatomic spacing of only 1.828 \AA , which is calculated from the MoS₂ lattice constant, 3.166 \AA , by $\frac{3.166 \text{ \AA}}{\sqrt{3}} = 1.828 \text{ \AA}$. And, viewed along the [111] direction, the 3D placement of Au atoms in its three planes are projected such that they form a hexagonal 2D lattice with a lateral interatomic ‘spacing’ which is related to the Au lattice constant, 4.078 \AA , by $\frac{4.078 \text{ \AA}}{\sqrt{6}} = 1.664 \text{ \AA}$. Per equation 3.2, these two spacings produce a Moiré superstructure with a period of about 18.5 \AA :

$$L = \frac{1.828 \text{ \AA} * 1.664 \text{ \AA}}{1.828 \text{ \AA} - 1.664 \text{ \AA}} = \frac{3.042 \text{ \AA}^2}{0.164 \text{ \AA}} = 18.5 \text{ \AA} \quad (3.5)$$

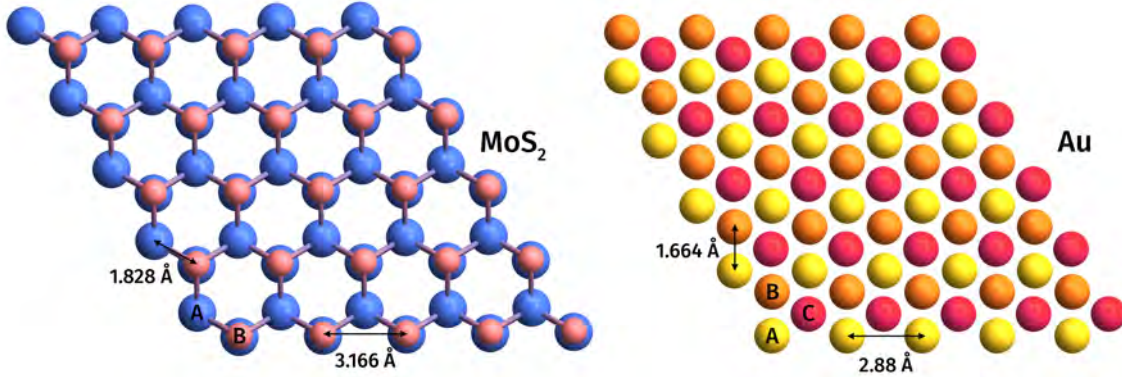


Figure 3.11: Projected 2D crystals of 2H-MoS₂ along the [0001] direction and fcc Au along the [111] direction account for the shorter Moiré period observed in STEM imaging. Layers are labeled with ‘A’, ‘B’, or ‘C’ to indicate stacking structure.

3.9 Chapter 3 Summary

Chapter 3 details how the TEM samples analyzed in this dissertation were prepared and studied. A typical TEM multi-modal workflow is explained, walking step-by-step through using HAADF-STEM, STEM-EDS, and 4D STEM during a microscope session. To lay the groundwork for analysis, the different options for thickness estimation using TEM methods are explored. Further, the benefits of performing diffraction simulations are highlighted: among them, elucidating the behavior of forbidden reflections that become visible in the diffraction patterns from thin-film gold. In order to ensure accuracy in strain measurements obtained from diffraction data, approaches to data calibration are described. While using a 4D STEM method, it is recommended to compare experimental data to simulated data, and a simulated tilt series of MoS₂ is presented. This chapter also contains my thoughts on understanding the morphology of MoS₂ and deposited gold using HAADF-STEM, and I include quasi-3D maps of both layered MoS₂ and nanoporous Au. Finally, a technical background is given into Moiré patterns and Moiré analysis in diffraction and HAADF-STEM.

Bibliography

- [1] Catriona M. McGilvery, Angela E. Goode, Milo S.P. Shaffer, and David W. McComb. “Contamination of holey/lacey carbon films in STEM”. In: *Micron* 43.2-3 (2012), pp. 450–455. ISSN: 09684328. DOI: 10.1016/j.micron.2011.10.026.
- [2] Xinjun Chu, Guanggeng Yao, Andrew Thye Shen Wee, and Xue Sen Wang. “Size-tunable Au nanoparticles on MoS₂(0001)”. In: *Nanotechnology* 23.37 (2012). ISSN: 09574484. DOI: 10.1088/0957-4484/23/37/375603.
- [3] Shunsuke Yamashita, Jun Kikkawa, Keiichi Yanagisawa, Takuro Nagai, and Kazuo Ishizuka. “Atomic number dependence of Z contrast in scanning transmission electron microscopy”. In: *Scientific Reports* 8.12325 (2018), pp. 1–7. ISSN: 2045-2322. DOI: 10.1038/s41598-018-30941-5.
- [4] Rik Brydson. *Aberration-Corrected Analytical Transmission Electron Microscopy*. 2011. ISBN: 9780470518519. DOI: 10.1002/9781119978848.
- [5] G. Stenberg and M. Boman. “Thickness measurement of light elemental films”. In: *Diamond and Related Materials* 5.12 (1996), pp. 1444–1449. ISSN: 09259635. DOI: 10.1016/S0925-9635(96)00563-8.
- [6] Ryan J. Wu, Michael L. Odlyzko, and K. Andre Mkhoyan. “Determining the thickness of atomically thin MoS₂ and WS₂ in the TEM”. In: *Ultramicroscopy* 147 (2014), pp. 8–20. ISSN: 18792723. DOI: 10.1016/j.ultramicro.2014.05.007.
- [7] J. C. Heyraud and J. J. Métois. “Anomalous 1/3 422 diffraction spots from {111} flat gold crystallites: (111) surface reconstruction and moiré fringes between the surface and the bulk”. In: *Surface Science* 100.3 (1980), pp. 519–528. DOI: 10.1016/0039-6028(80)90419-7.
- [8] M. H. Jacobs and M. J. Stowell. “Moiré patterns and coherent double-positioning boundaries in (111) epitaxial gold films”. In: *Philosophical Magazine* 11.111 (1965), pp. 591–603. ISSN: 00318086. DOI: 10.1080/14786436508224244.

- [9] Xiao Huang, Zhiyuan Zeng, Shuyu Bao, Mengfei Wang, Xiaoying Qi, Zhanxi Fan, and Hua Zhang. “Solution-phase epitaxial growth of noble metal nanostructures on dispersible single-layer molybdenum disulfide nanosheets”. In: *Nature Communications* 4 (2013). ISSN: 20411723. DOI: 10.1038/ncomms2472.
- [10] J. Reyes-Gasga, A. Gómez-Rodríguez, Xiaoxia Gao, and M. José-Yacamán. “On the interpretation of the forbidden spots observed in the electron diffraction patterns of flat Au triangular nanoparticles”. In: *Ultramicroscopy* 108.9 (2008), pp. 929–936. ISSN: 03043991. DOI: 10.1016/j.ultramicro.2008.03.005.
- [11] T. Walther, Y. Qiu, and A. G. Cullis. “Measuring the contrast in annular dark field STEM images as a function of camera length”. In: *Journal of Physics: Conference Series* 241 (2010). ISSN: 17426596. DOI: 10.1088/1742-6596/241/1/012068.
- [12] Kate Reidy, Georgios Varnavides, Joachim Dahl Thomsen, Abinash Kumar, Thang Pham, Arthur M. Blackburn, Polina Anikeeva, Prineha Narang, James M. LeBeau, and Frances M. Ross. “Direct imaging and electronic structure modulation of moiré superlattices at the 2D/3D interface”. In: *Nature Communications* 12.1 (2021), pp. 1–9. ISSN: 20411723. DOI: 10.1038/s41467-021-21363-5. arXiv: 2008.12215.

Chapter 4

STEM studies of MoS₂ and evaporated Au

This chapter details the results obtained using the approach defined in Chapter 2 and the methodology discussed in Chapter 3. Data confirm the preferred Au(111)-MoS₂(0001) epitaxial alignment and reveal the extent of strain in this system, the rippling in ultra-thin MoS₂, the self-avoiding growth morphology of thin-film Au, and the rotation between these species.

4.1 Epitaxial alignment of Au on MoS₂

Two types of TEM data can be used to examine the epitaxial alignment of a substrate and epilayer: HR-(S)TEM imaging, in which atoms can be individually discerned in real space, and diffraction, in which the crystal types can be identified and their orientations measured in reciprocal space. Here, a number of samples are presented for which this orientation identification is straightforward, as well as discuss the challenges in making an identification when the data do not fit the ideal, best-aligned case.

Figure 4.1 shows a set of diffraction patterns corresponding to a sample of thin gold grown on MoS₂(0001). The hexagonal reciprocal space lattice corresponding to the MoS₂ diffraction pattern along the [0001] zone axis is clearly marked in magenta. Near each MoS₂ reflection in Fig. 4.1, at a slightly larger radius, are additional diffraction spots, shown in green. These are indexed to the Au [111] zone axis. Note the presence of the $1/3\{422\}$ Au spots, which usually do not appear in an Au [111] diffraction pattern, except in thin films. The presence of these spots is explained in Section 3.5.

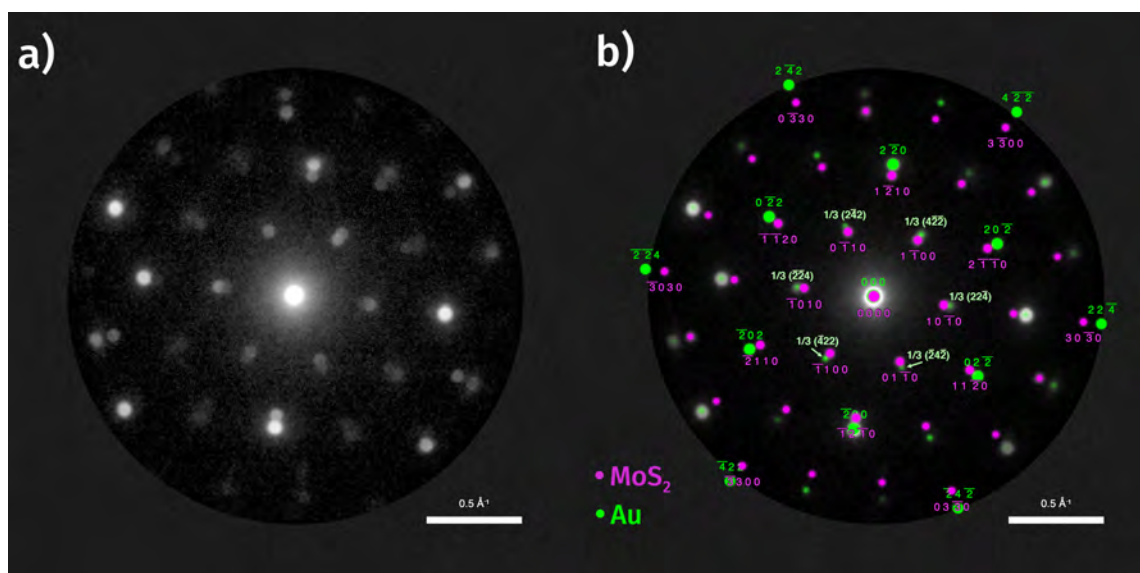


Figure 4.1: Diffraction pattern showing the (111) orientation of Au grown epitaxially on MoS₂(0001). a) the unlabeled diffraction pattern. b) the same diffraction pattern with disks indexed according to an MoS₂ zone axis of [0001], shown in magenta, and according to an Au zone axis of [111], shown in green. The 1/3{422} reflections are shown in light green.

The presence of an epitaxially-aligned system can sometimes be confirmed with low-magnification imaging methods, such as optical microscopy, if the epitaxial species grows into faceted crystallites with self-consistent orientations. In the Au-MoS₂ system studied here, e-beam deposited Au was often found to grow in triangles, truncated triangles (hexagons), and ‘bowties’, as shown in a representative HAADF image in Figure 4.2. Faceted crystallites alone are not evidence of a preferential alignment between the substrate and the grown species; it is the consistent orientation of these crystallites that proves it.

Figure 4.3 shows five evenly-spaced diffraction patterns of an Au crystallite grown on MoS₂, as in the sample shown in the top image of Fig. 4.2. Each diffraction pattern was recorded at locations on the sample that are 4 nm apart. These are five diffraction patterns out of 10,000 patterns recorded in a 100x100 nm area of the sample, with a 2-nm spacing between each one, and an incident beam with a width of 2 nm at FWHM. The great convenience of the 4D STEM approach is the ability to return to the same sample and re-examine specific features or perform new analysis after-the-fact. Diffraction patterns from various Au crystallites can be isolated and compared to each other as well as to diffraction from the underlying MoS₂ substrate.

As is to be expected for any sample with sufficient variation, the larger the sample size that is scanned using 4D STEM, the higher degree of variation shows up in the collected diffraction data. A standard step in typical STEM operation is to align the sample along a high-symmetry zone axis, in order to simplify analysis and increase the number and intensity of diffracted disks in the field of view. However, even if the electron beam is parallel to a high-symmetry zone axis at one point on the sample, lateral movement on the order of tens or hundreds of nanometers greatly increases the chances that in-plane rippling or other sample distortions will put the sample out of perfect alignment. In the diffraction patterns shown in Fig. 4.3, the closest high-symmetry zone axis is the [0001] axis of MoS₂ (and the [111] zone axis of Au), but the crystal is tilted by 2-4° from that axis.

4.1.1 Epitaxial alignment of Au: Moiré analysis

In high magnification HAADF-STEM imaging, Au was observed to have a Moiré periodicity with MoS₂ of 18 Å, as shown in Figure 4.5. At ultra-high (atomic) resolution, however, the true crystallographic periodicity is confirmed to be 32 Å (Figure 4.4), consistent with the predicted epitaxial alignment between Au and MoS₂ and

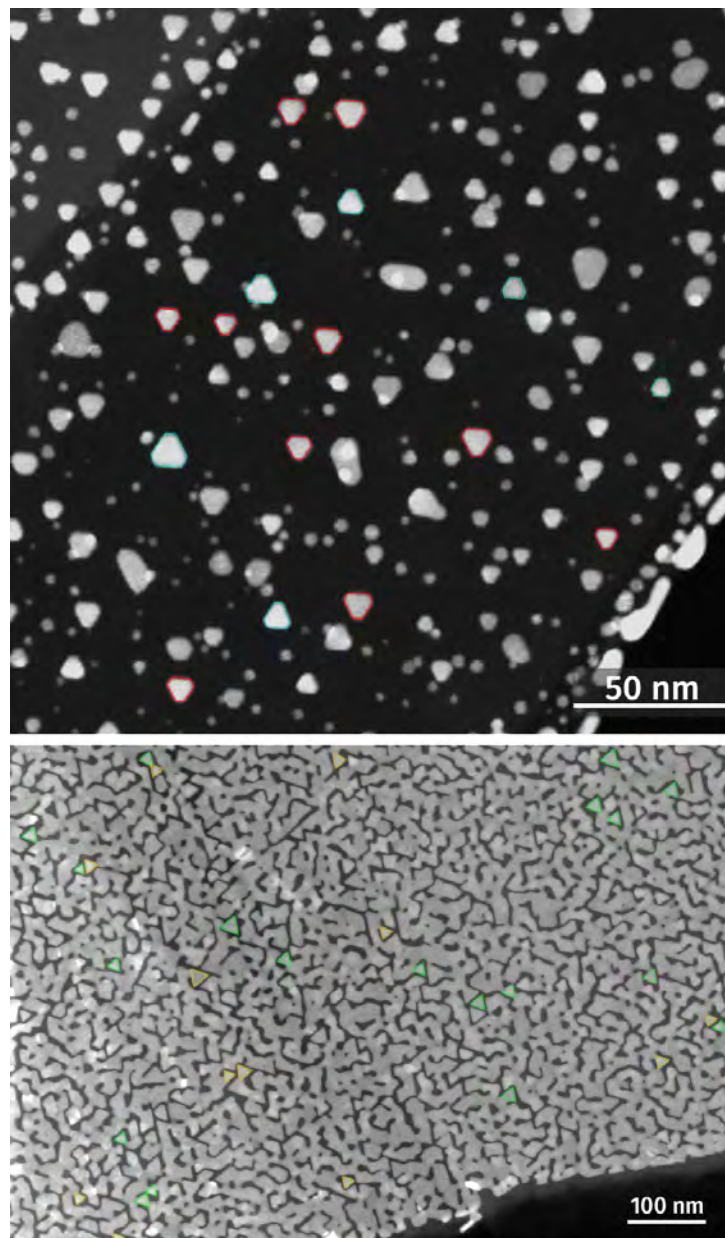


Figure 4.2: HAADF images showing consistent epitaxial alignment of Au crystallites grown on MoS₂. Above: Some truncated triangular Au crystallites are highlighted by red and cyan outlines, showing the symmetric alignments. Below: Triangular Au crystallites are highlighted by yellow and green outlines, showing the consistent symmetries.

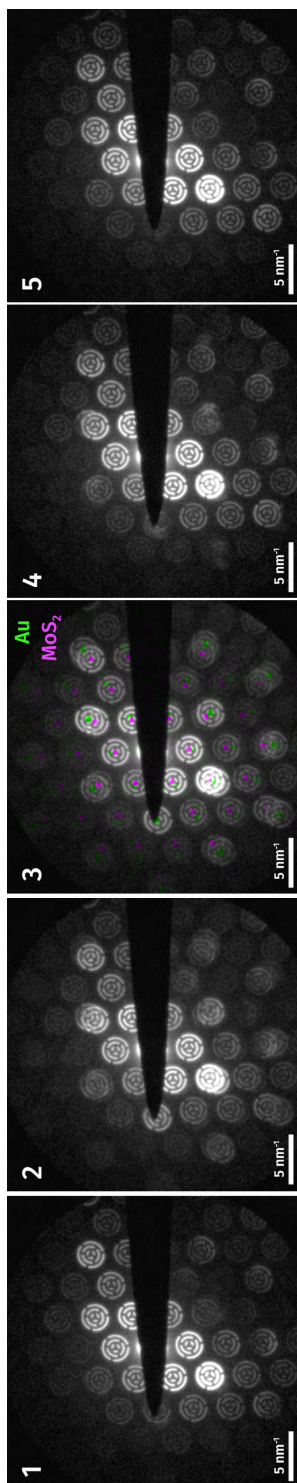


Figure 4.3: A small subset of 4D STEM images, collected as the beam scanned across a gold nanoparticle on a single MoS₂ crystal. Each diffraction pattern shown above was taken 4 nm apart, and cross a gold nanoparticle about 12 nm in size. Patterns 1 and 5 show diffraction patterns from MoS₂ along the [0001] zone axis, taken on either side of the nanoparticle. Patterns 2 and 3 are taken from the middle of the Au nanoparticle. Pattern 3 includes an overlay of the MoS₂[0001] and Au[111] diffraction patterns in magenta and green, respectively. Pattern 4 was taken on the edge of the nanoparticle. The beam spot size was about 2 nm at FWHM.

corresponding STM studies[1, 2]. The apparent 18 Å Moiré periodicity is seen consistently in STEM literature[3], but rather than a direct reflection of the lattice relationship between the two species, it was aptly described by Reidy *et al.* as an effect of STEM projection[4]. Indeed, a Moiré pattern is merely an interference effect from two nearby frequencies, and in STEM imaging, the overall Moiré is a convolution of the projections of all Moiré frequencies in the crystal. Electronic properties, however, are shown by Reidy and others to be modulated with the 31 Å periodicity.

4.2 Presence of strain

This section addresses two questions: 1) How much strain is intrinsic to this type of MoS₂ sample, made in this way? 2) How much strain is measurable in MoS₂, if any, using NBED-STEM data from regions with epitaxial gold nanocrystals or a nanoporous gold layer?

In general, MoS₂ is not discernibly strained in the vicinity of epitaxial gold. The most convincing evidence towards this conclusion is the thousands of diffraction patterns collected across hundreds of nanometers of Au-MoS₂ sample areas using a Zeltmann aperture, which makes a diffraction spot shift of even a couple pixels readily noticeable to a human observer. Diffraction patterns collected on and around a representative Au crystal on a MoS₂ substrate (Fig. 4.3) show no deviation in the location of the MoS₂ peaks, indicating that the MoS₂ crystal is in a consistent unstrained state, at least below a maximum sensitivity threshold of 0.1% for measurements performed.

This sensitivity threshold is calculated using the maximum pixel distance between diffraction peaks which can be reliably located in each diffraction pattern in a 4D STEM scan. For a 512 x 512 diffraction pattern, which was binned by 4 from a 2048-pixel camera, typical distances between furthest reflections were on the order of 400 pixels. If disk centers are found with a precision of 1 pixel, then the maximum sensitivity is $1/400 = 0.25\%$. For a 1024 x 1024 image (binned by 2 from a 2048-pixel camera), and a reasonable highest disk-to-disk distance of 900 pixels, the sensitivity threshold improves to about 0.1% (from $1/900 = 0.11\%$)

The advantage of binning the pixels in a diffraction pattern (rather than using the full camera resolution) is the improvement in signal-to-noise ratio, making it easier for computers and microscopists alike to identify the positions and borders of

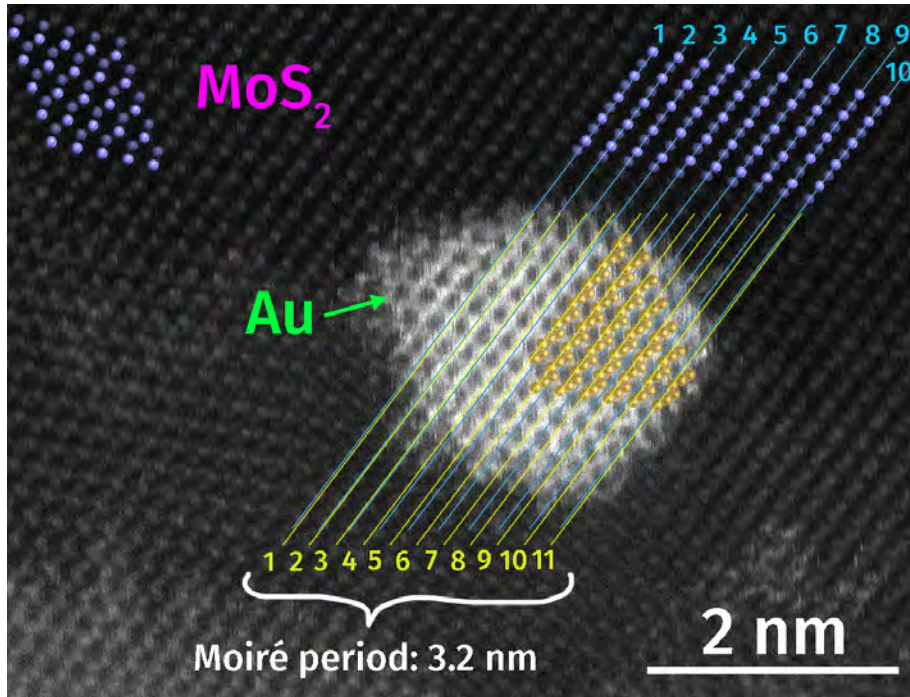


Figure 4.4: Even tilted slightly off-axis, the 10-to-11 Moiré periodicity of 32 Å is observed between MoS₂ and Au, respectively. Molybdenum atoms are clarified by a lavender overlay, with brighter atoms corresponding to a higher HAADF intensity and thus more atoms in the column. Sulfur atoms diffract too weakly to be discerned with these microscope conditions, and an overlay for them is not shown.

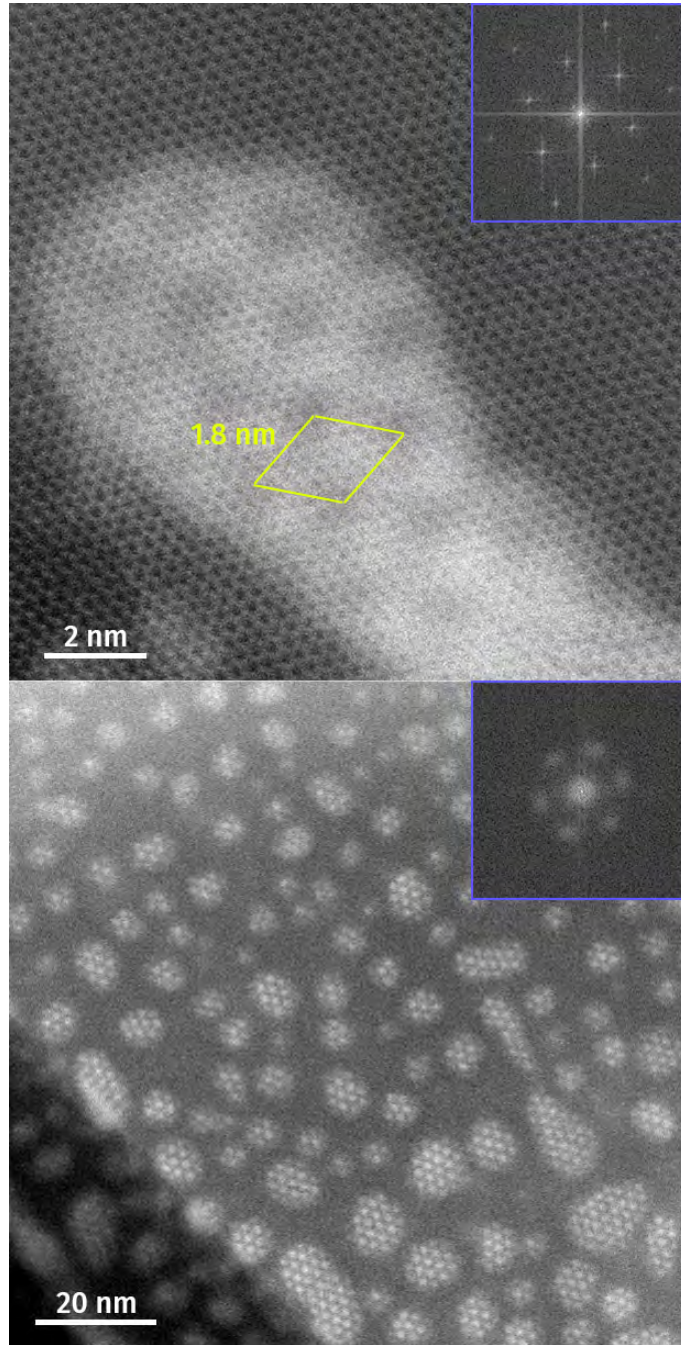


Figure 4.5: A mean Moiré pattern spacing of 1.8 nm is measured from two HR-STEM images of Au deposited on MoS₂. The respective FFTs are shown in the insets.

the Bragg disks.

In addition to the high sensitivity threshold for the data collected, one further complicating factor for this analysis was the degree to which exfoliated, natural MoS₂ samples could exhibit pre-existing strains, whether by defects[5, 6], elastic deformation[7, 8], corrugation[9, 10], or entropic (thermal) rippling[11, 12]. An example of corrugation in a flake of MoS₂ is shown in Figure 4.9.

In the samples analyzed for this work, un-coated (that is, without gold) molybdenum disulfide exhibited latent in-plane strains that measure up to 0.25%, with typical magnitudes of 0.1-0.15%. Analysis of a representative MoS₂ 4D STEM dataset, comprised of 400 MoS₂ diffraction patterns taken every 10 nm over a single-crystal 400x400 nm area, is shown in Figure 4.6. In Figure 4.7, a typical diffraction pattern from a few-layer MoS₂ sample is shown. In this example, the spacing between the diffraction disks is about 79 pixels, which is divided by a calibrated conversion factor of 217 pixels/Å⁻¹ to find the reciprocal lattice spacing of 0.366 Å⁻¹, or equivalently, 3.66 nm⁻¹. This measurement is in agreement with the known spacing for the MoS₂ (0001) diffraction pattern, corresponding to the reciprocal of the interplanar spacing of 2.73 Å between the {1100} planes in real space. As MoS₂ has a hexagonal lattice, the interplanar spacing can be derived from reciprocal lattice vectors using equation 1.7.

For a van der Waals layered crystalline material like MoS₂, diffraction patterns along the [0001] zone axis are the most convenient to analyze due to having equal unit vector magnitudes and consistent angles between unit vectors. However, experimentally, several other high-symmetry axes appear in datasets where the scan area contains multiple crystals, bends or ripples, or simply was not aligned to the [0001] direction before data collection. These patterns can still be used for crystal identification, strain measurements, and determining the epitaxial orientation of a deposited crystal on the (0001) surface.

It is challenging, however, to quickly or automatically distinguish the diffraction patterns of multiple crystals that are co-located, producing generally superimposed diffraction patterns. The difficulty lies in the exponential complexity with each added crystal; instead of simply fitting the diffraction disks to the closest zone axis of a known crystal, there is an additional task of first partitioning the disks belonging to each crystal when the species and zone axis could both be uncertain. Additionally, for a layered material like MoS₂, symmetries could be broken by defects such as an

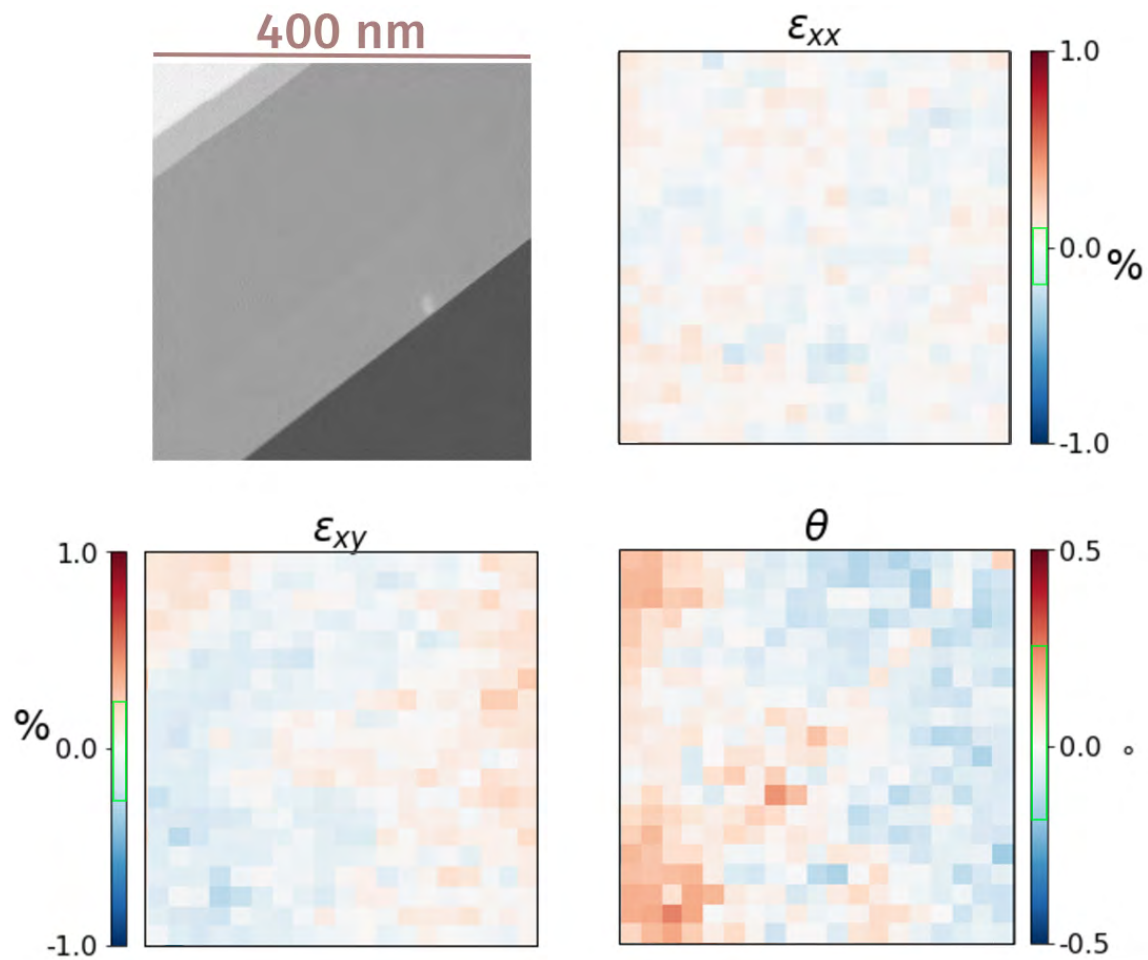


Figure 4.6: 4D STEM strain maps of single-crystal MoS₂ terraces, analyzed using py4DSTEM. Top-left: HAADF images of MoS₂ terraces; top-right: map of strains along the horizontal (x) direction; bottom-left: map of shear xy strain; bottom-right: map of local rotation. The range of colors expressed in each map is demarcated by a green box in their respective color bar legend.

intercalated species or a glide dislocation.

Figure 4.8 shows an indexed diffraction pattern for the $[2\bar{1}\bar{1}1]$ zone axis of MoS_2 , a lower symmetry zone axis to the typical $[0001]$ axis. These zone axes are significantly off-axis from each other, with an angle between them of 65.9° . When examining an MoS_2 sample in TEM, correcting a sample tilt of such a degree while maintaining x-y positioning is cumbersome. Instead, with a larger camera length than shown in Fig. 4.8, more diffraction disks can be brought into the diffraction plane and used for analysis. In this way, the sample can still be analyzed for such features as strain and azimuthal rotation, even while aligned along a less-common zone axis.

4.3 MoS_2 rippling

The best way to measure rippling in 2D materials is through a surface analysis method such as AFM or STM, or through a reflectance method. Determining the existence and extent of rippling in 2D materials using HAADF-STEM contrast alone is a semi-quantitative method, at best, but useful approximations can be made. The Z-contrast of the HAADF technique offers a way to track 2D density across a 3D sample. Put another way, where there is more material (such as in a slope of a ripple), there is brighter contrast. For this method to be somewhat accurate, the sample should be comprised of a consistent number of layers such that any variation in contrast must come from the tilt of those layers alone, putting more atoms in the beam path and resulting in more scattered electrons.

Energy-dispersive x-ray scattering can also give a measure of the material density – and the rise and fall of that density – as the beam scans across a sample. This can be roughly correlated to slopes and peaks in a rippled sample, if and only if the sample is comprised of a consistent number of layers.

In real space imaging, it may or may not be obvious that a suspended 2D material is bending in and out of the image plane. 4D STEM diffraction data can provide a more concrete analysis of rippling by comparing specific peak intensities with those in simulated STEM data[13]. Tilt angles can be ascertained and compared to the diffraction pattern taken every couple nanometers across a sample. Irrespective of scan direction, 4D STEM data can be reorganized into diagonals, or binned to allow more choice of angular rotations, such that the virtual scan direction can be more or less aligned with a single ripple direction.

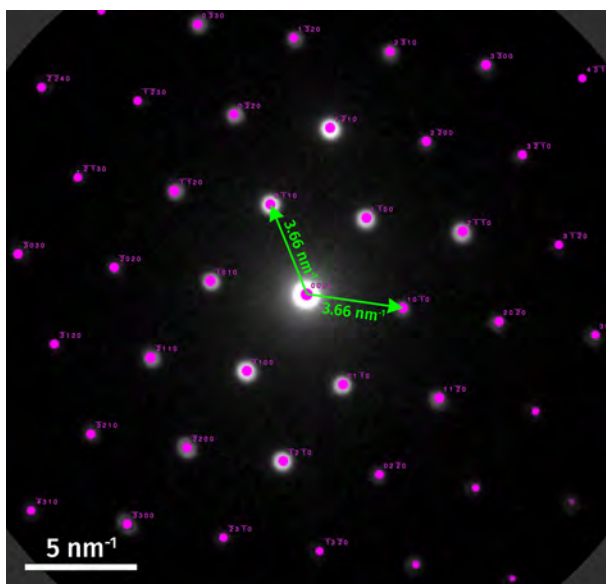


Figure 4.7: Single diffraction pattern from a 4D STEM dataset scanning few-layer MoS_2 . An ideal simulated $\text{MoS}_2[0001]$ diffraction pattern is overlaid in magenta.

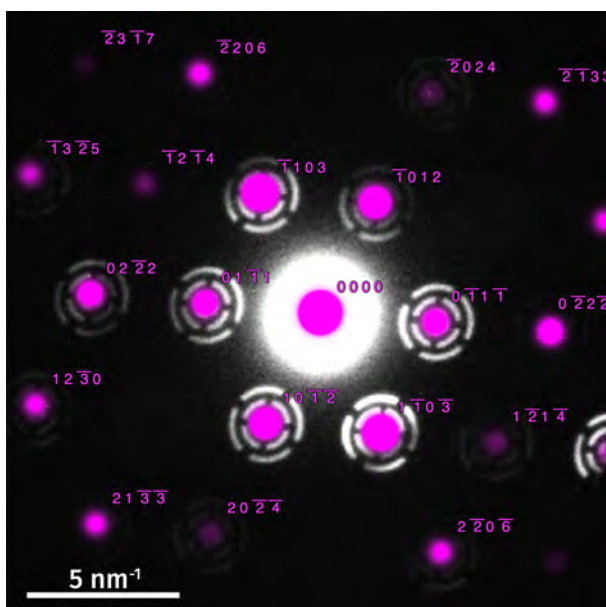


Figure 4.8: Single diffraction pattern from a 4D STEM dataset scanning few-layer MoS_2 , taken using a bullseye aperture. An ideal simulated $\text{MoS}_2[2\bar{1}\bar{1}1]$ diffraction pattern is overlaid in magenta.

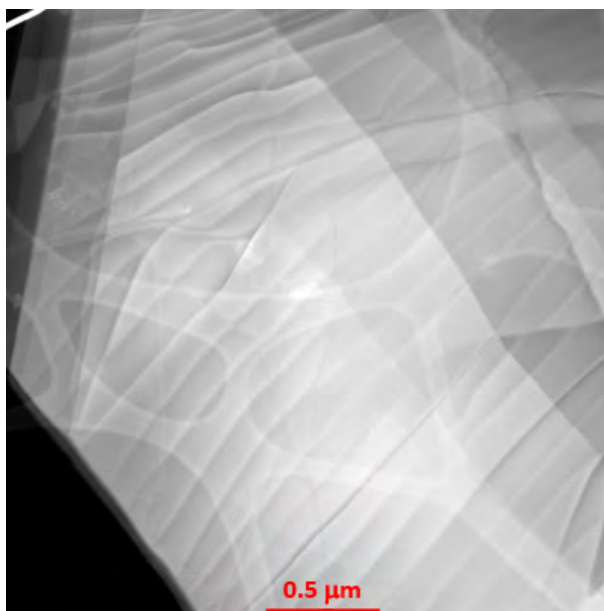


Figure 4.9: Large-period corrugation in a flake of multilayer MoS₂ suspended on a web of lacey carbon and ultrathin carbon.

4.4 Self-organization and growth of nanoporous Au

All molybdenum disulfide samples examined in the TEM for this dissertation were prepared from the same natural mined source, and all gold examined in this dissertation was deposited using e-beam evaporation at room temperature. Yet, a range of Au-MoS₂ morphologies was observed in the prepared samples. In some areas, small, rounded nanoparticles were observed, as in Figure 3.8, with a median diameter of 4 nm and about 1-4 nm between them. Well-oriented triangles and truncated triangles were also observed, as in Figure 4.2, with diameters between 6 nm and 10 nm, with nearest-neighbor spacings ranging from 1 nm to 6 nm. And, very commonly, semi-continuous nanoporous gold was found across large flakes (tens of microns across, Fig. 4.11) of MoS₂, with an approximate feature width (pore spacing) of 15 nm and an average pore size of 8 nm.

It should be noted that the only areas examined in the TEM were areas in which the Au-MoS₂ was sufficiently thin so as to be relatively electron-transparent, which

is usually defined as less than the effective mean free path of an electron through the material. For gold, a heavy atom in a dense FCC lattice, this distance is about 100 nm, but practically speaking, a thinner sample is preferable in order to avoid multiple scattering events and obtain data with a high signal-to-noise ratio.

Interestingly, the mean thickness of gold deposition according to the quartz crystal micro-balancing method was 10-15 nm, depending on the sample, with a purported accuracy of 1 Å. This, however conflicts with two observations seen frequently across the prepared samples: the presence of forbidden Au diffraction disks, generally only seen in exceptionally thin samples[14], and the weaker-than-expected Z-contrast from HAADF-STEM (Fig. 3.9). Both of these observations point to an actual thickness of less than 10 nm, perhaps even less than 5 nm, and this disparity is further exacerbated by the presence of gaps or pores in-between the deposited gold. These gaps should have, in fact, increased the actual thickness of gold in areas where it coalesced, to a thickness greater than 15 nm, in order to maintain that amount as mean thickness across the sample. One possible explanation would be selection bias, as suggested above, in that the only TEM data examined was collected in comparatively thin areas of the prepared samples. However, nanoporous gold was observed across large areas on the order of tens of microns, as shown in Figure 4.10a and 4.11, decreasing the possibility that thicker deposits of gold lie elsewhere on the unmeasured sample. This phenomenon requires further investigation.

In certain cases, on the TEM grids containing the Au-MoS₂ samples, polycrystalline Au nanoparticles appeared in small clusters by themselves, supported only by the ultrathin and lacey carbon supports of the TEM grid. This unintentional occurrence must have resulted from the sample preparation method, possibly as a result of dust particles that could have been on top of the MoS₂. When the MoS₂, together with its epitaxial Au, was cleaved by hand onto the TEM grids for characterization, these Au-coated dust particles may have been dislodged by friction and inadvertently adhered to the TEM support grid as shown in Figure 4.12.

4.5 Rotation of epitaxial Au: Diffraction analysis

Relative to the underlying MoS₂, epitaxial Au crystals exhibit various rotational relationships. Previous literature suggest that an idealized Au (111) epilayer grown on a flat, perfectly clean MoS₂ (0001) surface will exhibit an alignment where the [01 $\bar{1}$] direction of Au is parallel to the [11 $\bar{2}$ 0] direction of MoS₂ (note that the Au

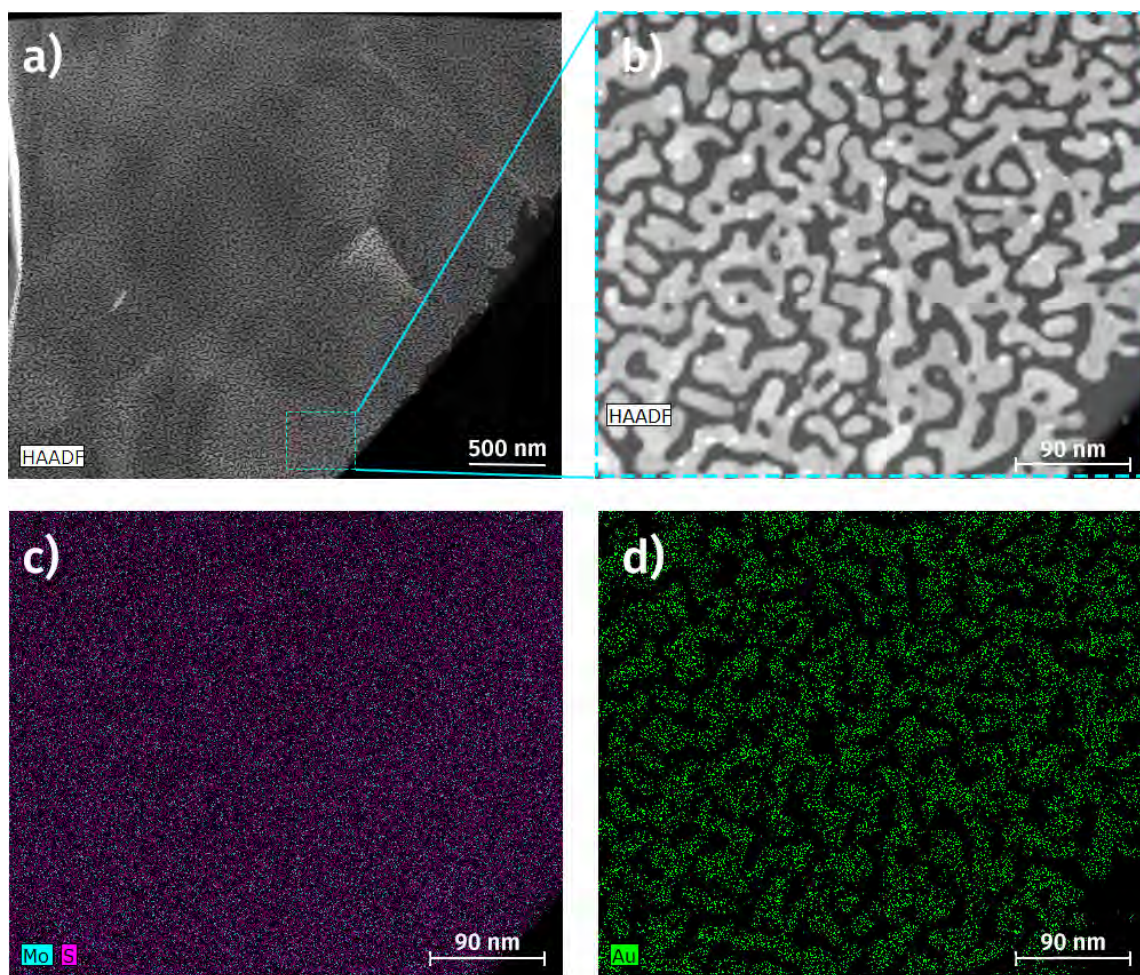


Figure 4.10: A large flake of single-crystal MoS₂, coated entirely with nanoporous gold. a) A low-magnification HAADF-STEM image of the flake. b) A higher-magnification image of a subsection of the flake shown in (a), marked by a dashed green rectangle. c) EDS map: Integrated EDS peak intensities at each pixel position corresponding to Mo-K and S-K transitions from the subsection shown in (b). d) EDS map: Integrated EDS peak intensities at each pixel position corresponding to the Au-L transition from the subsection shown in (b).



Figure 4.11: A large flake of single-crystal MoS₂, coated entirely with nanoporous gold. Two HAADF-STEM images are merged in the above image, joined at the green line shown.

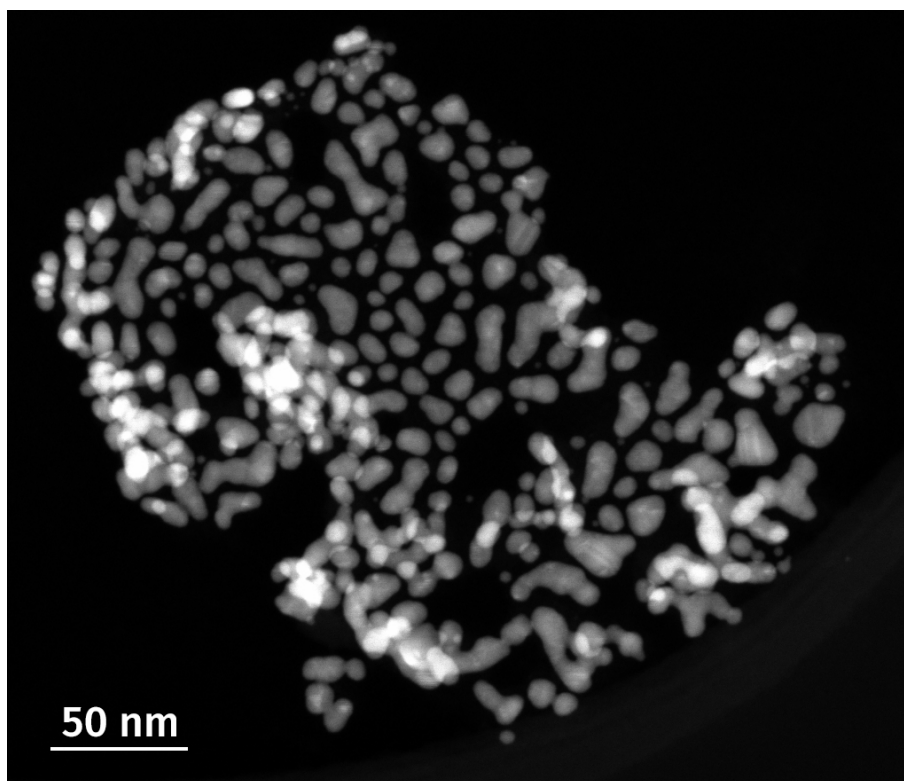


Figure 4.12: Gold nanoparticles on the TEM grid that are not adhered onto the cleaved MoS₂. The Au likely grew onto an impurity, which may have then been pumped out by the vacuum or destroyed by the electron beam.

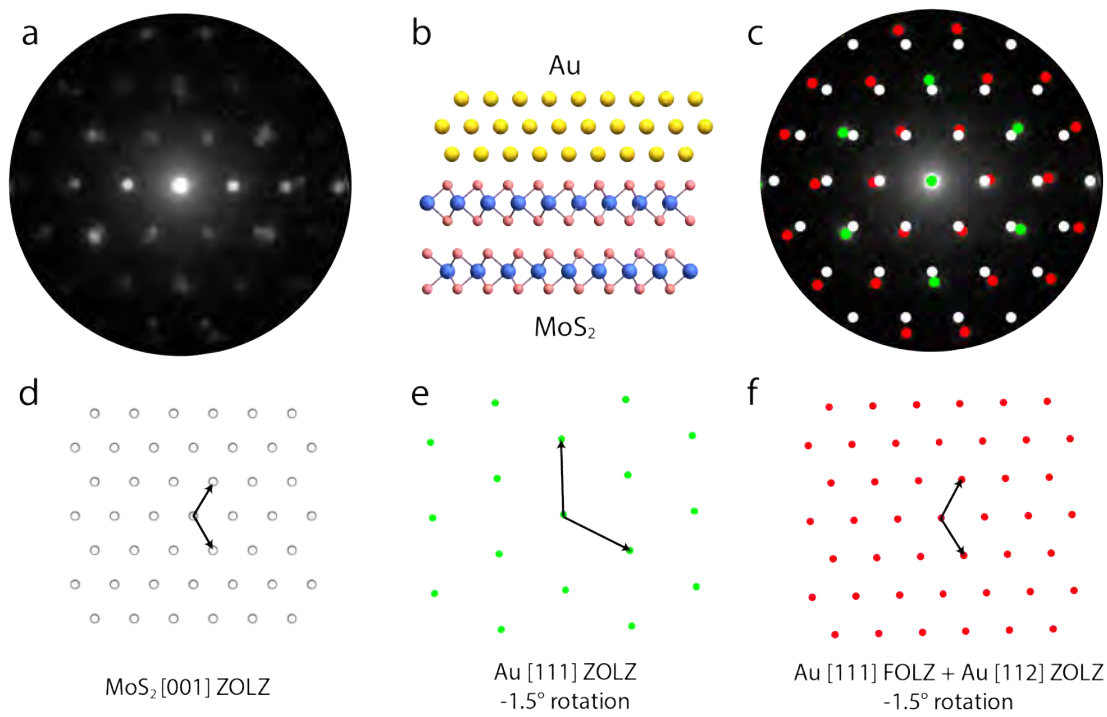


Figure 4.13: Apparent significant rotation between epitaxial Au and underlying MoS₂.

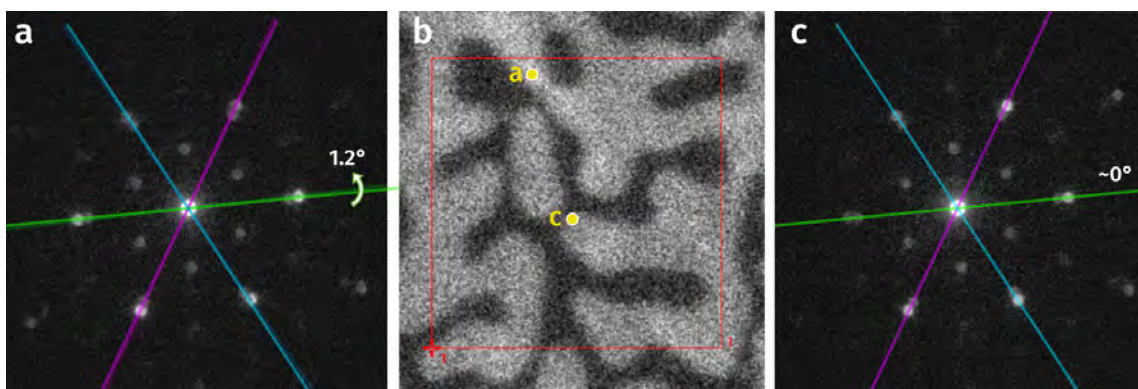


Figure 4.14: On the same sample, Au can exhibit different relative rotations with respect to the underlying MoS₂ lattice. a) The diffraction pattern from the location marked ‘a’ in the HAADF image in b. Here, the Au lattice is twisted with respect to the underlying MoS₂ by about 1.2°. Bright colored lines show perfect alignment, while faint colored lines are fit to the rotated disks. b) HAADF-STEM image of area where 4D STEM diffraction patterns were collected with a step size of 1 nm. 80 nm x 80 nm scan area marked by a red box. c) The diffraction pattern from the location marked ‘c’ in the HAADF image in b. Here, Au is well-aligned with the underlying MoS₂.

([01 $\bar{1}$] and Au [02 $\bar{2}$] vectors are co-linear). In a diffraction pattern, this relationship is shown by the co-linear alignment of the Au (02 $\bar{2}$) diffraction disk and the MoS₂ (11 $\bar{2}$ 0) diffraction disk, together with the central spot from the direct beam.

From a crystallography standpoint, this rotational alignment alone does not describe the placement of atoms on the respective crystals’ basis vectors, and thus does not directly describe the lateral placement of atoms in the Au(111) plane over the surface layer of sulfur atoms in the MoS₂. However, previous literature[15] suggests that the gold atoms will attempt to stack directly over the sulfur atoms, rather than between them. In any case, over a short distance, the Au atoms will cover a distribution of 11 different positional relationships to the MoS₂ lattice, as shown in Figure 4.4.

Au crystals were found to deviate slightly from this epitaxial relationship; specifically, the Au was found to be rotated azimuthally from the underlying MoS₂ semi-continuously up to about 3°, with a median twist of 1-1.5°, shown in Figures 4.13 and 4.14. Within the span of tens or hundreds of nanometers, some gold crystals were found to rotate from a respective -3° to +3° from the predicted epitaxial relation-

ship (Fig. D.5 and Fig. D.6). If the contact layer in the MoS₂ crystal is influenced at all by this rotation, such as by matching that rotation all or in part, then the resulting misalignment between MoS₂ surface and subsurface layers would modulate the interlayer separation between them and, if externally strained, produce buckling initiation sites at the points of highest separation [16]. This could support the theory behind observations of increased monolayer yield using exfoliation processes which utilize gold as a handle layer as discussed in Sections 1.1 and 1.2.

It should be noted that any rotational misalignment between MoS₂ layers inconsistent with the existing 6-fold rotational symmetry would, naturally, impose a free energy cost. Molecular dynamics simulations indicate that interlayer twists of at least 2° in 10-nm triangular flakes of 2H-MoS₂ can be corrected through relaxation[17], such as by annealing.

The crystal domain size of deposited Au is a limiting factor in how large rotated domains can be; namely, up to 15-20 nm. Rotational deviation from the expected epitaxial alignment was found repeatedly, across samples prepared by separate depositions and measured with different microscope parameters. Assuming little to no rotation in the single crystal of MoS₂, then in the span of 500 nm, for example, Au[1 $\bar{1}$ 0] – MoS₂[0 $\bar{1}$ 12] misalignment can range to an extreme of $\pm 3^\circ$. These rotated domains appear to exhibit little variation inside a given grain, and the large rotational variability over a large area occurs instead from the summation of the rotations of distinct grains and the probability of encountering extrema over increasingly large sample areas.

Figure 4.15 shows the result of the py4DSTEM analysis of a 2500-image 4D STEM dataset of an Au-MoS₂ sample. Here, py4DSTEM was utilized to track small changes in the Au{220} diffraction disk positions and calculate the corresponding deformation tensor.

4.5.1 Rotation: Moiré analysis

In Figure 4.16, the variation in the rotational alignment across a sample area of 234 nm is calculated to be $\pm 2^\circ$. The mean Moiré spacing observed in the HAADF image is 17.1 Å, which is 10.8 times the unstrained interplanar spacing for the MoS₂(11 $\bar{2}$ 0) plane, which is 1.58 Å. Thus, 10.8 is the Moiré magnification factor, which will be relevant in a moment.

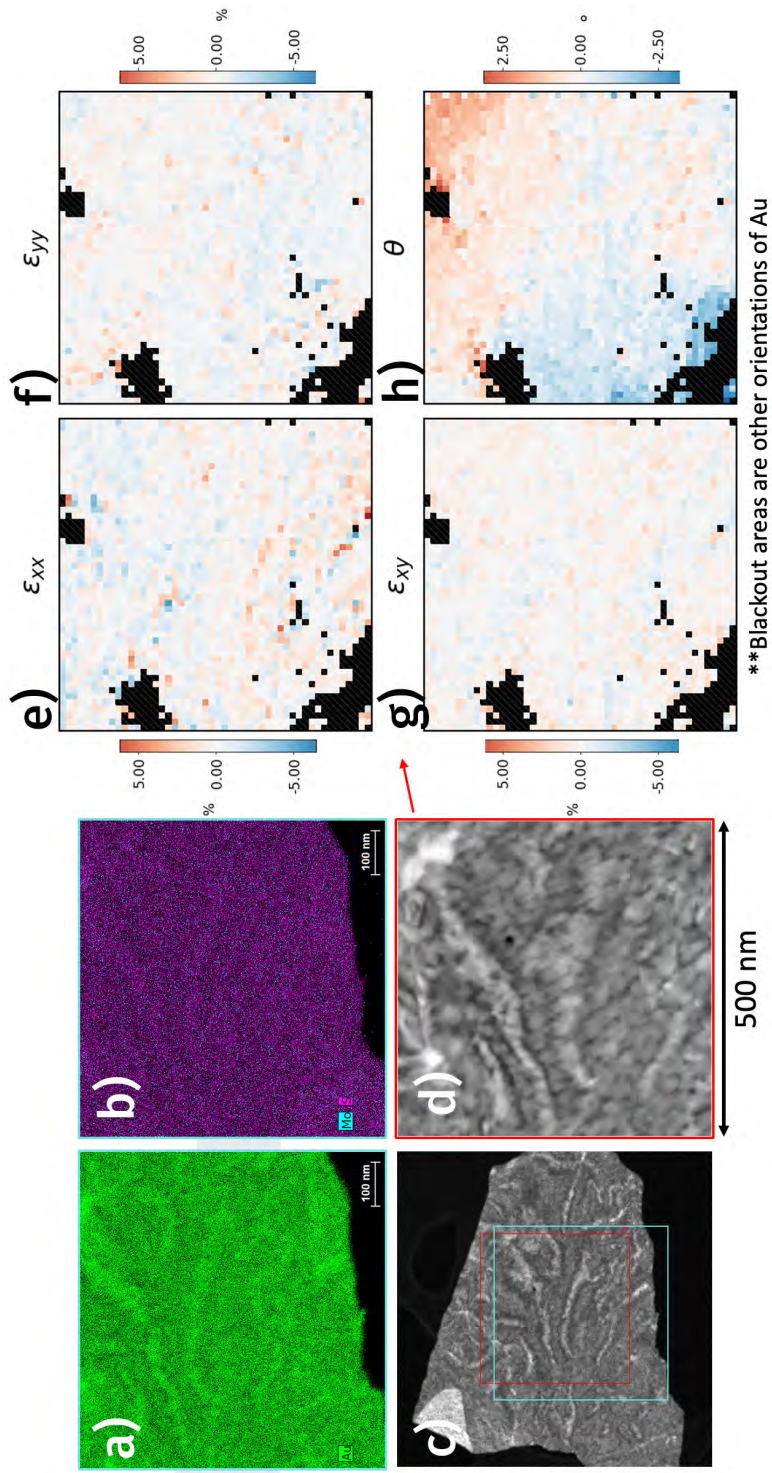


Figure 4.15: EDS, HAADF, and deformation maps of an Au-MoS₂ sample. py4DSTEM was used to analyze 2500 diffraction images collected over a 500x500 nm² sample area. Au was found to exhibit an (111) epitaxial orientation with respect to the underlying MoS₂ flake. a) Au-L EDS map of the area marked by the teal square in (c). b) Combined Mo-K and S-K map of the area marked by the teal square in (c). c) HAADF image of a flake of MoS₂ with deposited nanoporous gold. d) HAADF inset of the 4D STEM scan area. e-f) Deformation maps generated through a careful py4DSTEM analysis of the Au diffraction disks in the 4D STEM dataset. Blackout areas are locations where the MoS₂ is corrugated, thus changing the zone axis in those areas. e) Au strain map oriented such that the MoS₂ is corrugated, thus changing the zone axis oriented such that the y-axis is perpendicular to the scan direction. f) Au strain map oriented such that the y-axis is perpendicular to the scan direction. g) Map of the shear component of the Au deformation tensor. h) Rotation of the nanoporous Au with respect to the median rotation. A sweep of $\pm 2^\circ$ is reported.

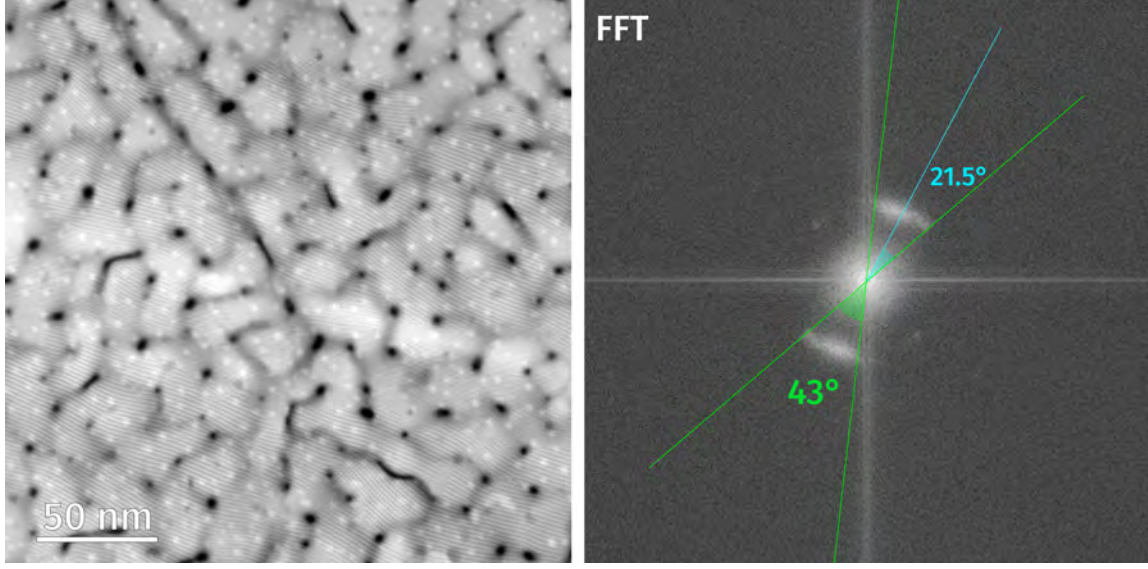


Figure 4.16: FFT analysis of high-resolution STEM imaging data (left) reveal a twist variation of $\pm 2^\circ$ from the expected epitaxial alignment.

The FFT in 4.16 (right) of the HAADF image (left) shows an angular sweep of 43° , corresponding to a variation of $\pm 21.5^\circ$. When divided by the Moiré magnification factor, 10.8, this yields a real-space angular variation of $\pm 1.99^\circ$, or approximately 2° . A 2° -sweep has been reported in a few earlier studies for metal-on-TMDC epitaxial systems[3, 18]. Equation 3.2 can then be used to find the spacing of the Au lattice. Assuming the MoS_2 lattice is unstrained, as diffraction data suggest, then the interplanar spacing of the $\text{MoS}_2(11\bar{2}0)$ plane, 1.58 \AA , can be used to find the interplanar spacing of the $\text{Au}(2\bar{2}0)$ plane:

$$L = \frac{d_{\text{MoS}_2(11\bar{2}0)}d_{\text{Au}(2\bar{2}0)}}{|d_{\text{Au}(2\bar{2}0)} - d_{\text{MoS}_2(11\bar{2}0)}|}$$

$$17.1 \text{ \AA} = \frac{(1.58 \text{ \AA})d_{\text{Au}(2\bar{2}0)}}{|d_{\text{Au}(2\bar{2}0)} - 1.58 \text{ \AA}|}$$

$$d_{\text{Au}(2\bar{2}0)} = 1.446 \text{ \AA}$$

which corresponds to an Au lattice parameter of 4.09 \AA , within the experimental tolerance of the literature-reported value of 4.078 \AA .

Figure 4.17 shows a sampling of phenomena observed in atomic-resolution real-space imaging of Au on MoS₂, such as the propensity of Au nanoparticles to nucleate along step edges of MoS₂ layers. These Au nanoparticles decorating the edge and defect sites of MoS₂ may in fact be p-doping the MoS₂[19]. Fig. 4.17 also shows that freely-suspended MoS₂ tends to curve and ripple, which is unsurprising given its high compliance. The fact that bilayer MoS₂ can exhibit noticeable curvature over such a short distance as 5 nm indicates that selected-area diffraction methods are likely missing a high degree of structural detail in the examination of mono- and few-layer TMDCs. The use of a converged probe and the collection of 4D STEM data will be able to track this rippling across the sample, which will be instructive in future attempts to design nanoscale devices based on these materials. In HR-STEM imaging, in-plane bending with an observed radius of curvature of approximately 50 nm is observed (cyan curves and red tangent lines in Fig. 4.17c). If the out-of-plane bending is of the same order, then the sulfur atoms on the surface layers (top and bottom) of the bilayer MoS₂ would experience a maximum strain of about 1%:

$$\epsilon_x = \frac{\pm y}{\rho} \quad (4.1)$$

$$\epsilon_x = \frac{0.456 \text{ nm}}{50.0 \text{ nm}} = 0.91\% \quad (4.2)$$

where ϵ_x is the x-strain, y is the distance from the neutral axis (the midpoint of the bending medium), ρ is the radius of curvature, and the sign depends on the particular surface under consideration; one surface will be compressed (negative sign convention) and the other stretched (positive sign). This is an equivalent expression to $\epsilon_x = \frac{\pm t}{2\rho}$, where t is the distance between the two surfaces of the bent medium (the MoS₂ layer)[16].

It is expected that bending stiffness will increase with layer thickness. Simply, mono- and bilayer regions will bend more than regions with many layers. The majority of the 4D STEM data collected examined areas thicker than two layers, and accordingly, smaller strains were reported, if they registered above the sensitivity threshold for a given measurement. Changes in the electronic structure of MoS₂ are predicted to occur under strains as small as 1%, including switching back to an indirect band gap, suggesting that tight control of this bending is desirable in order to maintain control of the these properties in monolayer material.

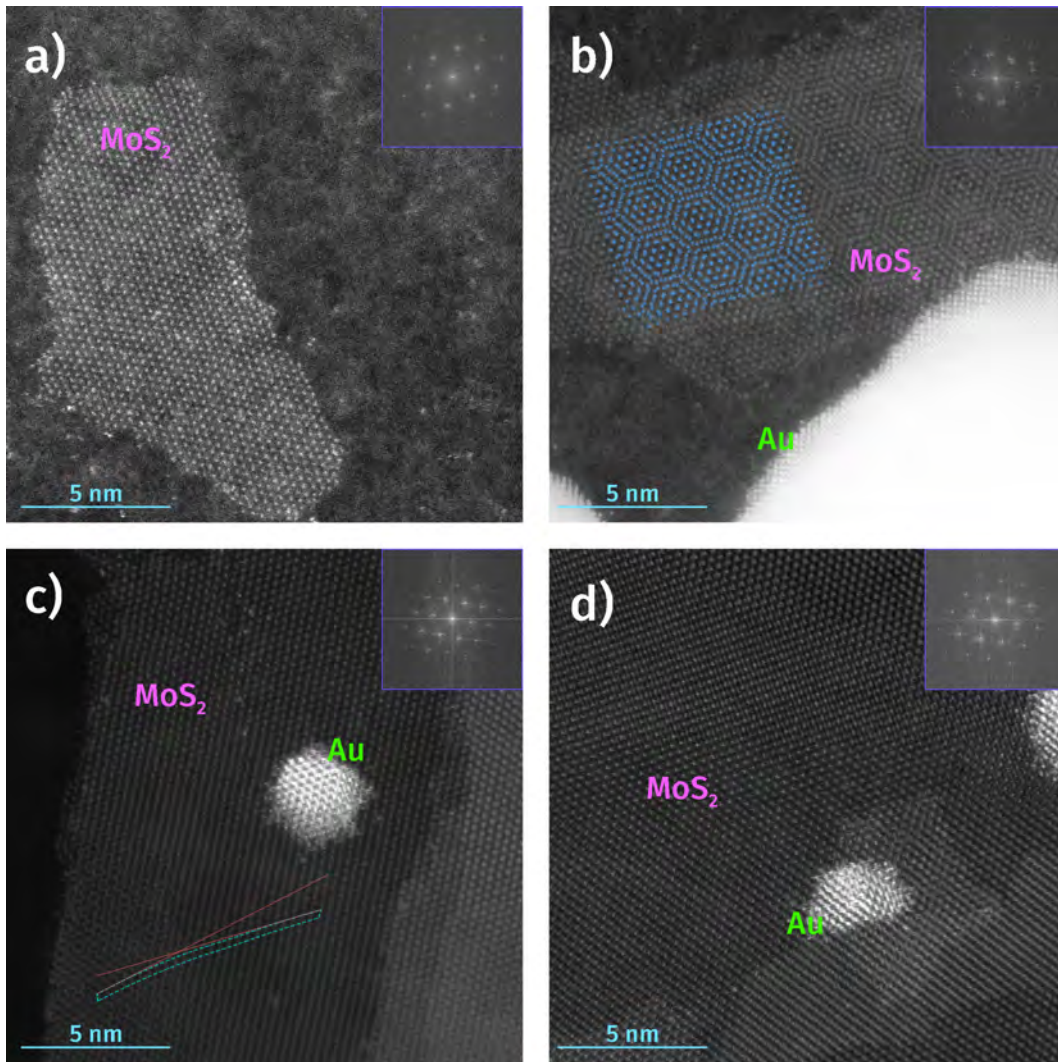


Figure 4.17: Atomic-resolution STEM images of Au nanoparticles grown on few-layer MoS₂, with FFTs shown as insets. a) A monolayer of hexagonal MoS₂ suspended on an ultrathin carbon support. b) A twisted bilayer of MoS₂, exhibiting a twist Moiré pattern corresponding to an interplanar rotation of about 8.4°. The bright region at the bottom of the image is a large Au grain. c) An epitaxially-aligned nanoparticle of Au on bilayer 2H-MoS₂. MoS₂ is shown to bend with a radius of curvature of about 50 nm. Individual gold atoms appear as bright points moving across the MoS₂ surface due to beam irradiation. d) Au nanoparticles on few-layer MoS₂. One nanoparticle is co-located with a small piece (6-nm diameter) of MoS₂ monolayer which is rotated by 8.4° relative to the MoS₂ underneath.

4.6 Chapter 4 Summary

This chapter contains a discussion of the STEM study of MoS₂ and epitaxial Au on MoS₂. Gold was typically found to be oriented with the (111) plane parallel to the (0001) basal plane of MoS₂, with the [1 $\bar{1}$ 0] direction of Au usually parallel to the [11 $\bar{2}$ 0] direction of MoS₂. Epitaxial Au can be misaligned to the underlying MoS₂ by up to $0 \pm 2\%$, and perhaps by up to 3%; this is shown using both diffraction and Moiré analysis of HR-STEM HAADF images.

In a majority of diffraction data collected, Au $1/3\{422\}$ spots are observable, indicating that the Au present is exceptionally thin, likely thinner than 10 nm, despite a supposed deposited thickness of 15 nm. It is shown here that Au can grow on MoS₂ with a triangular and truncated triangular morphology, with facets consistent with the $\{\bar{1}11\}$ and $\{100\}$ planes[20]. It is found that when the Au islands begin to coalesce in areas of the sample with presumably higher Au flux, these facets may be preserved as the gold avoids forming a continuous film, instead forming a nanoporous layer.

Measurements from diffraction data suggest that the MoS₂ is not additionally strained in the presence of gold, at least not beyond the sensitivity threshold of about 0.1% with the microscope parameters utilized in this study. Irrespective of the presence of epitaxial gold, exfoliated MoS₂ is measured to occasionally exhibit latent in-plane strains with a typical magnitude of 0.10-0.15%, and may in places be as high as 0.25%.

Bibliography

- [1] Signe G. Sørensen, Henrik G. Füchtbauer, Anders K. Tuxen, Alex S. Walton, and Jeppe V. Lauritsen. “Structure and electronic properties of in situ synthesized single-layer MoS₂ on a gold surface”. In: *ACS Nano* 8.7 (2014), pp. 6788–6796. ISSN: 1936086X. DOI: 10.1021/nn502812n.
- [2] Signe S. Grønborg, Søren Ulstrup, Marco Bianchi, Maciej Dendzik, Charlotte E. Sanders, Jeppe V. Lauritsen, Philip Hofmann, and Jill A. Miwa. “Synthesis of Epitaxial Single-Layer MoS₂ on Au(111)”. In: *Langmuir* 31.35 (2015), pp. 9700–9706. ISSN: 15205827. DOI: 10.1021/acs.langmuir.5b02533. arXiv: 1509.06864.
- [3] Yinghui Sun, Haofei Zhao, Dan Zhou, Yuchen Zhu, Huanyu Ye, Yan Aung Moe, and Rongming Wang. “Direct observation of epitaxial alignment of Au on MoS₂ at atomic resolution”. In: *Nano Research* 12.4 (2019), pp. 947–954. ISSN: 19980000. DOI: 10.1007/s12274-019-2329-4.
- [4] Kate Reidy, Georgios Varnavides, Joachim Dahl Thomsen, Abinash Kumar, Thang Pham, Arthur M. Blackburn, Polina Anikeeva, Prineha Narang, James M. LeBeau, and Frances M. Ross. “Direct imaging and electronic structure modulation of moiré superlattices at the 2D/3D interface”. In: *Nature Communications* 12.1 (2021), pp. 1–9. ISSN: 20411723. DOI: 10.1038/s41467-021-21363-5. arXiv: 2008.12215.
- [5] C. Ataca, H. Şahin, E. Aktuörk, and S. Ciraci. “Mechanical and electronic properties of MoS₂ nanoribbons and their defects”. In: *Journal of Physical Chemistry C* 115.10 (2011), pp. 3934–3941. ISSN: 19327447. DOI: 10.1021/jp1115146. arXiv: 1009.5488.
- [6] Zahabul Islam and Aman Haque. “Defects and grain boundary effects in MoS₂: A molecular dynamics study”. In: *Journal of Physics and Chemistry of Solids* 148. April 2020 (2021), p. 109669. ISSN: 00223697. DOI: 10.1016/j.jpcs.2020.109669.

- [7] Andres Castellanos-Gomez, Menno Poot, Gary A. Steele, Herre S.J. Van Der Zant, Nicolás Agrait, and Gabino Rubio-Bollinger. “Elastic properties of freely suspended MoS₂ nanosheets”. In: *Advanced Materials* 24.6 (2012), pp. 772–775. ISSN: 15214095. DOI: 10.1002/adma.201103965.
- [8] Qu Yue, Jun Kang, Zhengzheng Shao, Xueao Zhang, Shengli Chang, Guang Wang, Shiqiao Qin, and Jingbo Li. “Mechanical and electronic properties of monolayer MoS₂ under elastic strain”. In: *Physics Letters, Section A: General, Atomic and Solid State Physics* 376.12-13 (2012), pp. 1166–1170. ISSN: 03759601. DOI: 10.1016/j.physleta.2012.02.029.
- [9] Emmanuel Okogbue, Jung Han Kim, Tae Jun Ko, Hee Suk Chung, Adithi Krishnaprasad, Jean Calderon Flores, Shraddha Nehate, Md Golam Kaium, Jong Bae Park, Sei Jin Lee, Kalpathy B. Sundaram, Lei Zhai, Tania Roy, and Yeonwoong Jung. “Centimeter-Scale Periodically Corrugated Few-Layer 2D MoS₂ with Tensile Stretch-Driven Tunable Multifunctionalities”. In: *ACS Applied Materials and Interfaces* 10.36 (2018), pp. 30623–30630. ISSN: 19448252. DOI: 10.1021/acsmi.8b08178.
- [10] Daniel J. Trainer, Yuan Zhang, Fabrizio Bobba, Xiaoxing Xi, Saw Wai Hla, and Maria Iavarone. “The Effects of Atomic-Scale Strain Relaxation on the Electronic Properties of Monolayer MoS₂”. In: *ACS Nano* 13.7 (2019), pp. 8284–8291. ISSN: 1936086X. DOI: 10.1021/acsnano.9b03652.
- [11] Peng Wang, Wei Gao, and Rui Huang. “Entropic effects of thermal rippling on van der Waals interactions between monolayer graphene and a rigid substrate”. In: *Journal of Applied Physics* 119.7 (2016), pp. 1–12. ISSN: 10897550. DOI: 10.1063/1.4941987. arXiv: 1511.02914.
- [12] Fatemeh Ahmadpoor and Pradeep Sharma. “A perspective on the statistical mechanics of 2D materials”. In: *Extreme Mechanics Letters* 14 (2017), pp. 38–43. ISSN: 23524316. DOI: 10.1016/j.eml.2016.12.007.
- [13] Colin Ophus. “A fast image simulation algorithm for scanning transmission electron microscopy”. In: *Advanced Structural and Chemical Imaging* 3.1 (2017). ISSN: 21980926. DOI: 10.1186/s40679-017-0046-1. arXiv: 1702.01904.
- [14] J. Reyes-Gasga, A. Gómez-Rodríguez, Xiaoxia Gao, and M. José-Yacamán. “On the interpretation of the forbidden spots observed in the electron diffraction patterns of flat Au triangular nanoparticles”. In: *Ultramicroscopy* 108.9 (2008), pp. 929–936. ISSN: 03043991. DOI: 10.1016/j.ultramicro.2008.03.005.

- [15] Yuzhi Zhou, Daisuke Kiriya, E. E. Haller, Joel W. Ager, Ali Javey, and D. C. Chrzan. “Compliant substrate epitaxy: Au on MoS₂”. In: *Physical Review B* 93.5 (Feb. 2016), p. 054106. DOI: 10.1103/PhysRevB.93.054106. arXiv: 1505.07505.
- [16] Shuze Zhu and Harley T. Johnson. “Moiré-templated strain patterning in transition-metal dichalcogenides and application in twisted bilayer MoS₂”. In: *Nanoscale* 10.44 (2018), pp. 20689–20701. ISSN: 20403372. DOI: 10.1039/c8nr06269b.
- [17] Shuze Zhu, Pascal Pochet, and Harley T. Johnson. “Controlling Rotation of Two-Dimensional Material Flakes”. In: *ACS Nano* 13.6 (2019), pp. 6925–6931. ISSN: 1936086X. DOI: 10.1021/acsnano.9b01794.
- [18] Anna C. Domask, Kayla A. Cooley, Bernd Kabius, Michael Abraham, and Suzanne E. Mohny. “Room Temperature van der Waals Epitaxy of Metal Thin Films on Molybdenum Disulfide”. In: *Crystal Growth and Design* 18.6 (2018), pp. 3494–3501. ISSN: 15287505. DOI: 10.1021/acs.cgd.8b00257.
- [19] Yumeng Shi, Jing Kai Huang, Limin Jin, Yu Te Hsu, Siu Fung Yu, Lain Jong Li, and Hui Ying Yang. “Selective decoration of Au nanoparticles on monolayer MoS₂ single crystals”. In: *Scientific Reports* 3.1839 (2013), pp. 1–7. ISSN: 20452322. DOI: 10.1038/srep01839.
- [20] Peiyu Chen, Krishnan Murugappan, and Martin R. Castell. “Shapes of epitaxial gold nanocrystals on SrTiO₃ substrates”. In: *Physical Chemistry Chemical Physics* 22.8 (2020), pp. 4416–4428. ISSN: 14639076. DOI: 10.1039/c9cp06801e.

Chapter 5

Photoluminescence Characterization of MoS₂ and WS₂ Prepared by Gold-Assisted Exfoliation

In this chapter, I show empirical evidence of the successful selective exfoliation of large single layers of MoS₂ and WS₂ using epitaxial Au as a compliant handle layer. This study inspired the TEM investigations into the Au-MoS₂ relationship which were detailed in the preceding chapters. Here, exfoliated monolayers as well as smaller bi- and multi-layer areas are evaluated using photoluminescence microscopy (PL). MoS₂ and WS₂ monolayers notably exhibit a direct band gap at the K and K' points of the first Brillouin zone, and this gives rise to circular dichroism and intensifies their interaction with visible light to allow significant photoluminescence. As such, PL spectroscopy and imaging are straightforward methods of identifying and evaluating the presence and quality of exfoliated TMDC monolayers. Along with optical reflectance spectroscopy, PL imaging can assess the size of the continuous flakes of monolayer material, and it was used to affirm the use of gold in the exfoliation process to greatly enhance monolayer yield.

In 2015, Gábor Zsolt Magda *et al.* reported the use of evaporated gold to exfoliate large areas of TMDC monolayers, up to hundreds of microns in diameter[1]. When compared to previous tape-exfoliated methods which usually produce monolayer flakes smaller than 10 microns[2–5], this represents an improvement of a couple orders of magnitude (1-2 orders in length and 2-4 orders in area). We and others have replicated and then iterated upon this gold-assisted exfoliation process to yield large exfoliated areas[6, 7] as well as deterministic arrays of large-area monolayer MoS₂ and WS₂[8, 9]. The samples prepared and evaluated using PL in this chapter had a typical lithographically-defined shape that was hundreds of micrometers in length,

providing further evidence of the success of this technique.

5.1 Applicability of photoluminescence spectroscopy (PL) for MoS₂ and WS₂ layer characterization

Photoluminescence spectroscopy (PL) can easily confirm the successful isolation of a transition metal dichalcogenide monolayer. When directly compared, a monolayer and a bilayer of the same material, e.g. MoS₂, was found to differ in luminescence intensity by about two orders of magnitude, with little shift in exciton peak location. In this section, a progression of monolayer selectivity improvements is confirmed via PL spectroscopy and visualized across the samples with PL imaging.

Photoluminescence spectroscopy non-destructively probes a sample's atomic and chemical composition by analyzing the characteristic wavelengths of light emitted after its electrons are excited by an incident laser. So-called 'micro-PL' spectroscopy has a typical excitation probe diameter (FWHM) of several micrometers. This method yields 1-dimensional data in the form of photoluminescence intensity ('signal', or counts) versus the wavelength (or, equivalently, photon energy). The method can be expanded to a 2D or 3D domain through PL imaging or PL mapping, respectively.

In imaging mode, a camera captures light intensity from the 2D sample area. Using filters in the laser setup, such as high-pass or low-pass filters, the wavelength range that is accepted into the camera can be narrowed to an energy band of interest. In the case of monolayer MoS₂, this range was chosen to be 550 nm to about 828 nm, designed to isolate the signals between 1.5 eV and 2.25 eV, including the exciton peaks at 1.85-1.88 eV (A-exciton) and 1.98-2.04 eV (B-exciton) for MoS₂[10–12]. When measuring monolayer WS₂, a 500 nm long-pass filter was used instead of a 550 nm filter, in order to capture the exciton peaks at 2.03-2.07 eV (A-exciton) and 2.36 eV (B-exciton) for WS₂[13]. In the monolayer case, only the A-exciton of WS₂ is involved in photoluminescence.

It is always necessary to measure detailed photoluminescence spectra to complement imaging data to ensure that any unintended peaks are addressed and not mistaken for the target peak. In imaging mode, the camera does not discern between wavelengths of light. However, for the purpose of confirming the presence or yield of a monolayer of a TMDC across a millimeter-centimeter size sample, PL imaging

proves a relatively fast and effective tool. Essentially, the signal-to-noise ratio and the ratio of the A-exciton peak to the B-exciton peak provide a rough measure of the quality of the monolayer, and thus the success of the transfer process. Isolation from the substrate can also result in an improved A-exciton photoluminescence peak[14].

5.2 Discussion of photoluminescence spectroscopy characterization

Due to quantum confinement effects, as discussed in ref. [10], photoluminescence is enhanced in layered d-electron materials such as MoS₂ and WS₂ in the monolayer case. The enhanced photoluminescence peak resonance exactly corresponds to the direct excitonic transitions in the MoS₂ electronic structure. Figure 5.1 shows an optical image of an exfoliated flake of MoS₂ and a corresponding photoluminescence spectrum from the region indicated in the optical image. Both the A- and B-exciton characteristic energies of MoS₂ are visible, with the A-exciton energy defined as the optical band gap of MoS₂. It is this peak which is enhanced in a high-quality TMDC monolayer.

In the PL spectrum shown in Fig. 5.1, the peak intensity for the A-exciton excitation occurs at 1.88 eV, and the deconvolved peak intensity for B-exciton occurs at 2.03 eV.

Figure 5.2 shows the result of an improved exfoliation process compared to that which produced the flake shown in Fig. 5.1. Accordingly, the A-excitonic peak is further enhanced, and the optical image shows an improved macroscopic uniformity in the exfoliated monolayer. It is known that defects can trap excited electrons and prevent their radiative relaxation. Photoluminescence spectroscopy is therefore a highly sensitive method for detecting TMDC monolayer quality. In literature, the ratio of the A-exciton peak to the B-exciton peak is commonly used as a figure of merit for TMDC monolayer quality, and it was used to guide the development of the patterning and exfoliation processes reported in my co-authored references [8, 9].

In order to enhance the photoluminescence quantum yield, exfoliated monolayer MoS₂ and WS₂ samples were treated with the bis(trifluoromethane) sulfonimide (TFSI) superacid. TFSI treatment has previously been shown to improve the quantum yield in exfoliated transition metal dichalcogenide monolayers[15, 16]. In our samples, I found that the superacid treatment resulted in an increase in the quantum

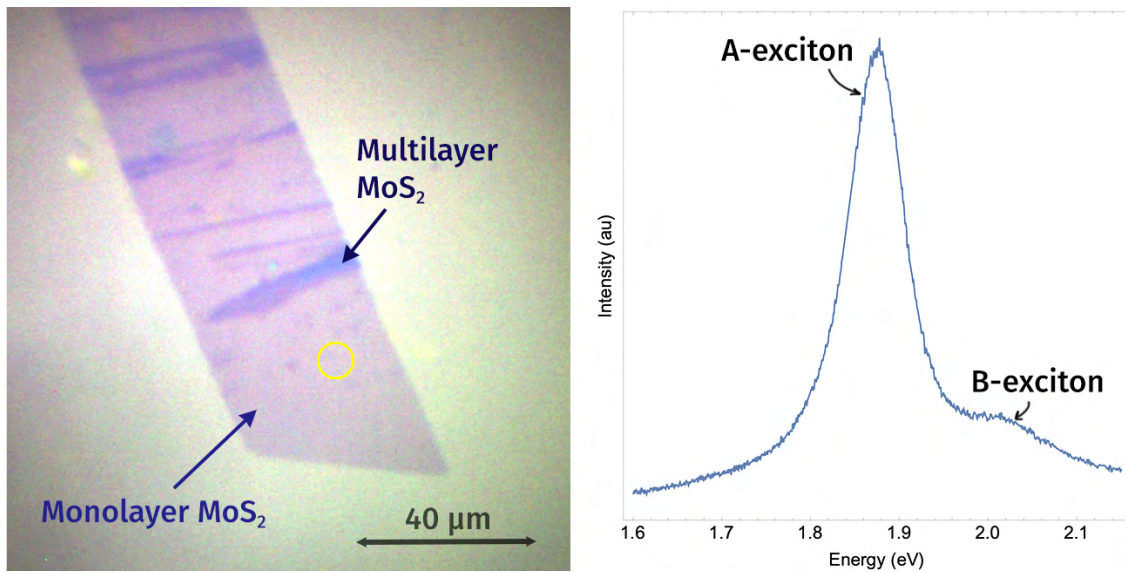


Figure 5.1: Optical image and corresponding photoluminescence spectrum of an exfoliated MoS₂ flake, consisting mostly of monolayer material. Left: Optical white-light image of an exfoliated flake of MoS₂ on 260 nm thermal SiO₂ on Si. Right: Photoluminescence spectrum collected from the area circled in yellow in the optical image. The peaks corresponding to the A- and B-excitons of MoS₂ are labeled.

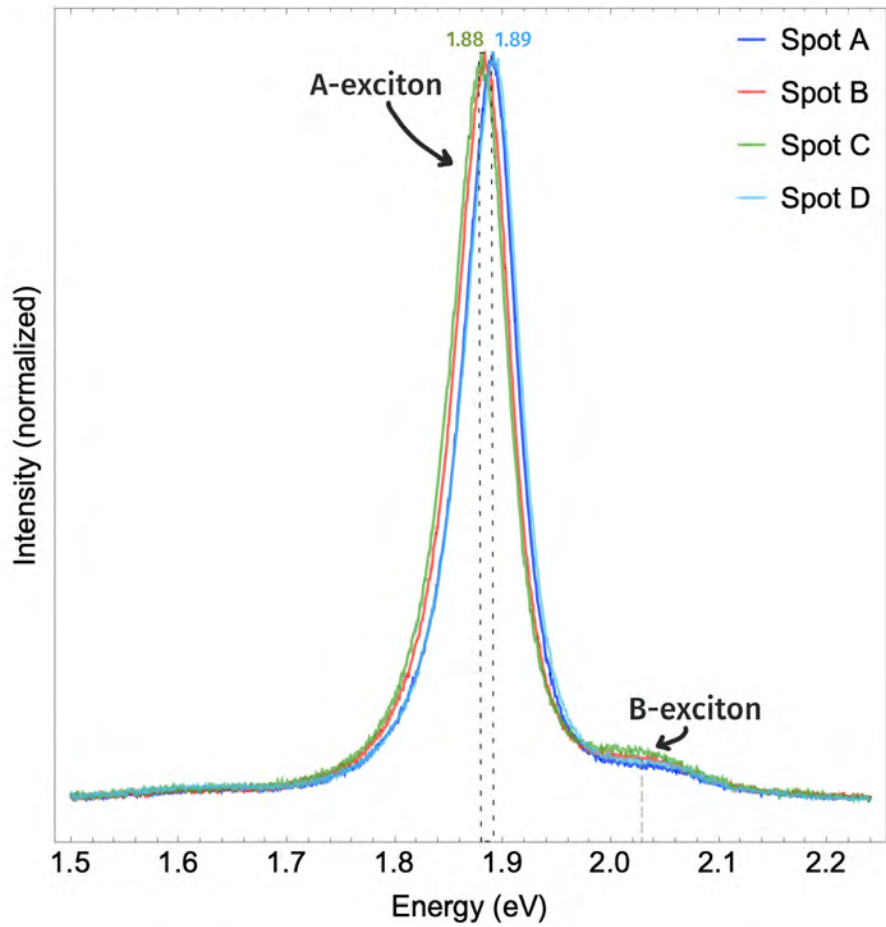
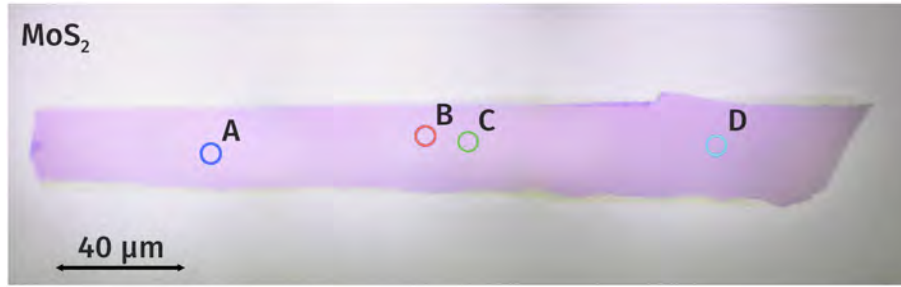


Figure 5.2: Optical image and corresponding photoluminescence spectra of an exfoliated MoS₂ monolayer flake. Top: Combination of four optical white-light images of an exfoliated flake of MoS₂ on SiO₂. Bottom: Photoluminescence spectra collected from the areas indicated in the optical image. The A-exciton and B-exciton peaks are labeled.

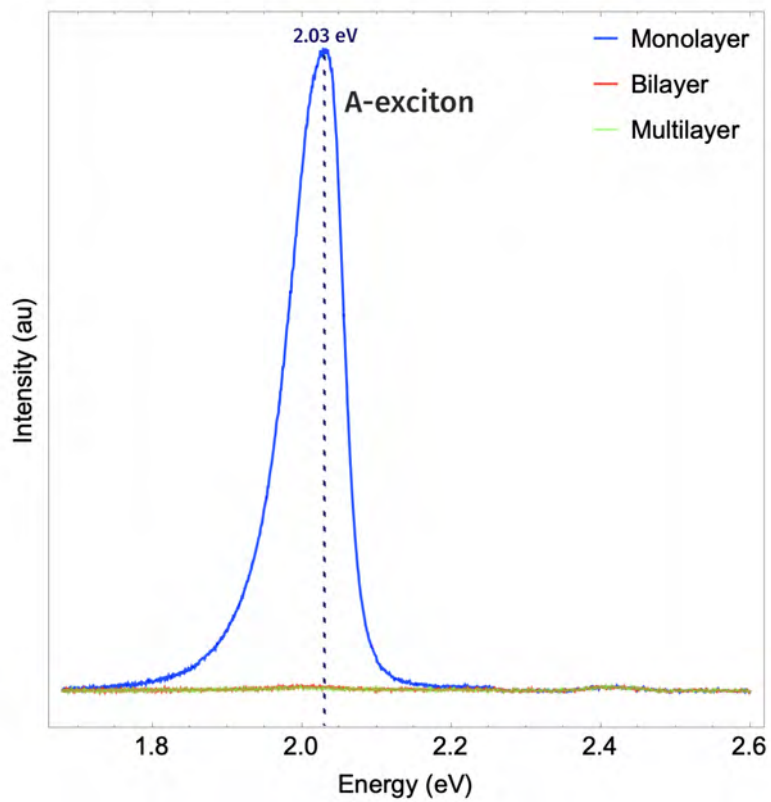
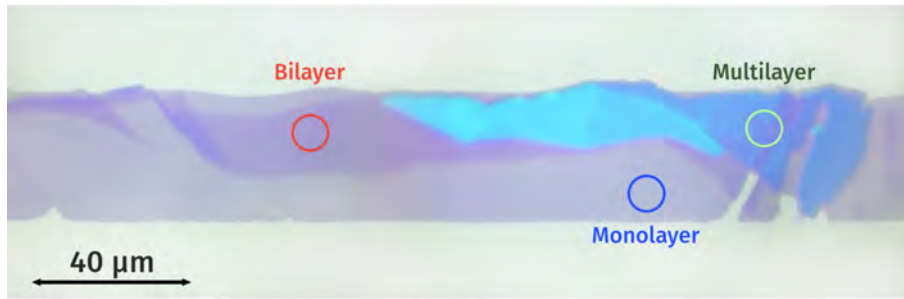


Figure 5.3: Optical image and corresponding photoluminescence spectra of an exfoliated WS_2 flake, consisting of monolayer, bilayer, and multilayer areas. Top: optical white-light image of an exfoliated flake of WS_2 on SiO_2 . Bottom: Photoluminescence spectra collected from the areas indicated in the optical image.

yield of WS₂ by at least 25x (Figure 5.5d), and an increase in that of MoS₂ by more than 100x(Figure 5.4d). This was demonstrated by measuring exfoliated samples before and after the superacid treatment, and measuring the large increases in photoluminescence intensities, with all experimental parameters (such as illumination intensity) held constant.

The mechanism by which TFSI is thought to improve the photoluminescence intensity to such a degree is thought to be the repairing of defects on the TMDC surface, namely, sulfur vacancies [15, 16]. These vacancies would otherwise trap the electrons in the bound excitons and trions, which then decay through nonradiative recombination rather than through luminescence. Through treatment with TFSI, a sulfonated anion, these sulfur vacancies can be chemically passivated. The experimental procedure for this treatment is briefly described in section 5.3.3.

5.3 Experimental methods

This section will explain the materials and experimental setup and parameters in order to carry out this photoluminescence study.

5.3.1 Sample preparation: Exfoliation using thermal release tape as adhesive layer

Photoluminescence spectroscopy (PL) was performed on exfoliated MoS₂, WS₂, and WS₂-MoS₂ samples. Thermal release tape, kapton tape, SiO₂ substrates, and gold were also examined for photoluminescence to assess the presence of contamination or background spectra.

To prepare the MoS₂ samples, natural mined molybdenite bulk crystals were acquired (eBay) and split by hand, using either tweezers or razor blades to cleave the crystal and create macroscopically-flat surfaces on the order of millimeters in diameter. The sample was delaminated and thinned to a sub-millimeter thickness, and the flattest sections were chosen for further sample preparation. These MoS₂ flakes were mounted to a glass microscope slide using double-sided Kapton tape. Additional MoS₂ samples with a thickness of 0.2 – 0.3 mm were obtained from HQ Graphene (Groningen, Netherlands), which were made using chemical vapor transport (CVT)

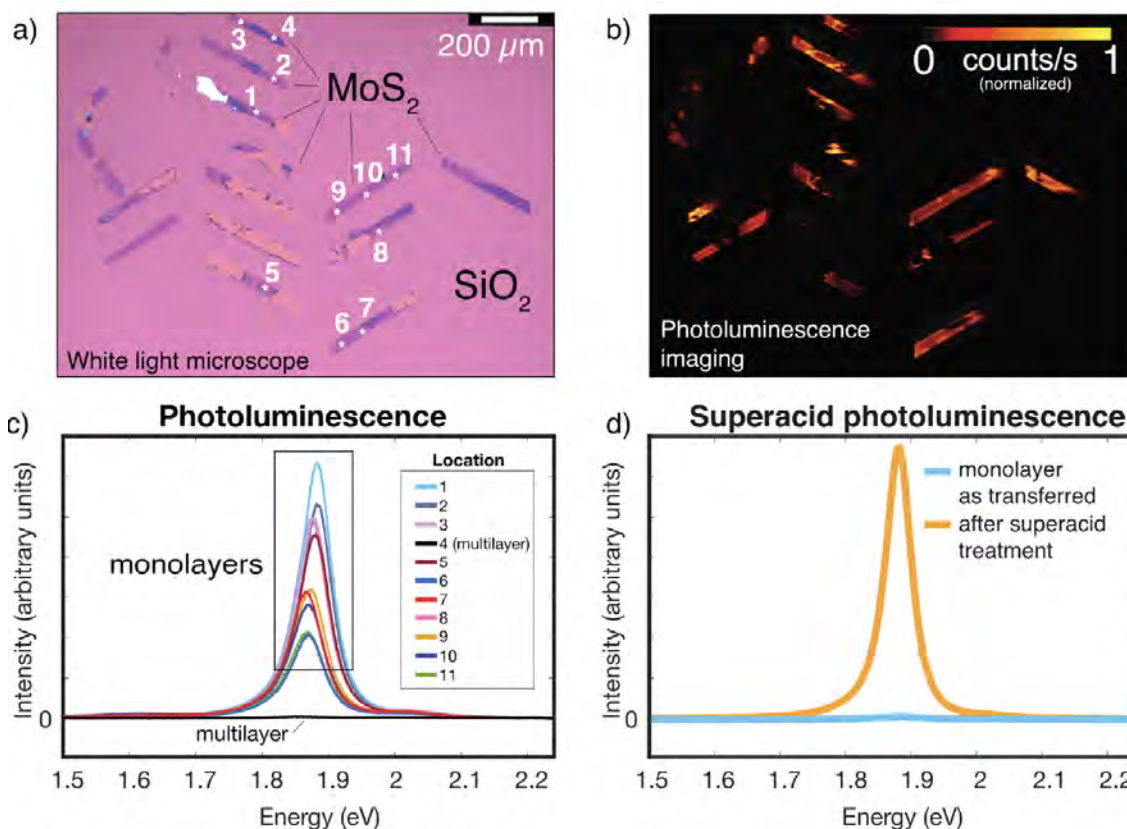


Figure 5.4: Optoelectronic MoS₂ monolayer characterization. (a) White-light reflectance image of a set of transferred MoS₂ features on 260 nm thermal SiO₂ on Si; (b) photoluminescence image of the region; (c) photoluminescence spectra associated with the numbered locations in (a), confirming that monolayer MoS₂ has been transferred to the substrate; (d) the results of treating MoS₂ monolayers with a superacid, showing more than a one hundred-fold increase in quantum efficiency. *Reprinted with permission from* Hannah M. Gramling, Clarissa M. Towle, Sujay B. Desai, Haoye Sun, Evan C. Lewis, Vu D. Nguyen, Joel W. Ager, Daryl Chrzan, Eric M. Yeatman, Ali Javey, and Hayden Taylor. “Spatially Precise Transfer of Patterned Monolayer WS₂ and MoS₂ with Features Larger than 10⁴ μm² Directly from Multilayer Sources”. In: *ACS Applied Electronic Materials* 1 (2019), pp. 407–416. Copyright 2019 American Chemical Society.

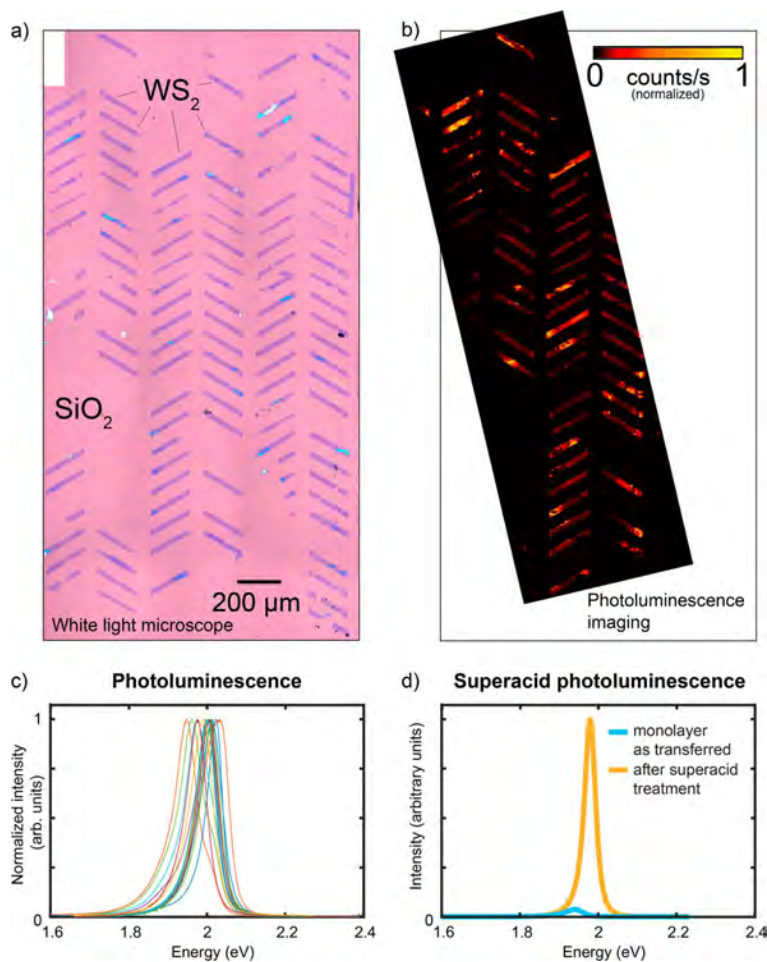


Figure 5.5: Optical and optoelectronic WS₂ monolayer characterization. (a) White-light reflectance image of a set of transferred WS₂ features on 260 nm thermal SiO₂ on Si. (b) Photoluminescence image of part of the same region as in (a): orientation is the same as (a), and the outline corresponds to that of the region imaged in (a). (c) Photoluminescence spectra from 13 regions of WS₂ on 260 nm thermal SiO₂ on Si, confirming that monolayer WS₂ has been transferred to the substrate. (d) Result of treating a WS₂ monolayer with TFSI superacid, showing more than a 25-fold increase in quantum efficiency. *Reprinted with permission from Hannah M. Gramling et al. “Spatially Precise Transfer of Patterned Monolayer WS₂ and MoS₂ with Features Larger than 10⁴ μm² Directly from Multilayer Sources”. In: ACS Applied Electronic Materials 1 (2019), pp. 407–416. Copyright 2019 American Chemical Society.*

and used as received.

Multilayer WS_2 samples fabricated by CVT were also obtained from HQ Graphene, also with a thickness of 0.2 – 0.3 mm, and used as received.

In order to prepare monolayers and heterostructures, a multi-step fabrication process was developed and improved upon, using the photoluminescence studies presented in this section as a key characterization step in that iterative design process. The detailed procedures for creating these samples and assessing their electronic performance can be found in references [8] and [9]. A summary of each methodology is included below.

The crux of this sample preparation method is the use of desposited gold as an epitaxial layer during MoS_2 or WS_2 exfoliation. For the samples examined in this section, 100 nm of Au was deposited by thermal evaporation (Torr International, Inc.). Then, an additional compliant handle layer is added on top of the gold layer by spin-coating a 15- μm -thick AZ 4620 photoresist (PR, MicroChemicals GmbH). This photoresist is patterned as described in the supplementary information with reference [8].

After the photoresist is patterned to expose certain gold areas, those areas of gold are etched by immersing the sample in an undiluted KI/I_2 solution for 1 minute (Gold Etchant TFA, Transene Company, Inc.) and then rinsing in deionized (DI) water. This is done in order to expose the negative pattern of MoS_2 or WS_2 to a plasma etch. The samples were exposed to a CF_4 plasma for 30 seconds at a flow rate of 20 sccm at a power of 100 W (Plasma Equipment Technical Services, Inc., Brentwood, CA)).

The top of the sample – that is, the positive pattern of photoresist – is contacted with thermal release tape (REVALPHA, Nitto), and rubber-tipped tweezers were brushed along the back of the tape, applying light manual pressure. The tape, together with the photoresist-gold-TMDC stack, is peeled by hand from the bulk TMDC flake. This stack is mounted to a thermally oxidized silicon wafer target that has been prepared according to reference [8], and the tape is released by heating the sample on a hot plate to 160 °C. The remaining photoresist is removed with an acetone bath, and the sample is then ashed in oxygen plasma for 3 minutes (20 sccm, 300 W, Plasma Equipment Technical Services, Inc.) to remove unwanted organic residue.

The remaining gold is stripped with a KI/I₂ etchant, revealing the patterned, majority-monolayer TMDC material underneath. The TMDC sample, on its SiO₂ substrate, is rinsed in DI water and dried.

5.3.2 Sample preparation: Exfoliation using unbaked photoresist as adhesive layer

Following examination of photoluminescence spectra, Raman spectra, and electronic properties of the exfoliated MoS₂ and WS₂ features exfoliated by the process described in subsection 5.3.1, this process was further refined to improve monolayer quality and yield. This iterated-upon process is described below.

CVT-fabricated WS₂ multilayer sources were obtained from HQ Graphene (Groningen, Netherlands) as before, and the MoS₂ sources used were natural, mined crystals from Crystal Age (Bristol, UK). The gold and photoresist handle layers were prepared as in subsection 5.3.1. A mask of 100μm by 100μm squares was used to lithographically define the microfeatures for these samples. The photoresist served two purposes: to define these features, and to provide a vertical offset (a buffer layer) between the adhesive and the TMDC layers, decreasing the chance of inadvertent contact and bulk exfoliation.

A one-minute SF₆ plasma etch was used to remove unwanted TMDC material in the negative patterned area (20 sccm, 200 W, Plasma Equipment Technical Services, Inc.). Without this step, monolayer yield decreased; thus, it is thought that etching the TMDC material around the intended microfeatures effectively creates crack initiation sites along the edges and enhances the chance of selective monolayer exfoliation.

A key difference in this second exfoliation method is a change in the adhesive used to grip the pattern and perform the exfoliation. Instead of a prefabricated thermal release tape from REVALPHA, a custom heat-releaseable adhesive film was made by spin-coating a low-crosslinked viscoelastic polymer onto a fluorinated ethylene propylene (FEP) film as described in reference [9] and the related supplementary material. One benefit of using the FEP film as an adhesive backing is its ability to mount onto a micromanipulator setup merely by electrostatic force.

In a cleanroom at ambient conditions, a photomask aligner (OAI Series 200 Aligner) comprised of a microscope and a manipulator setup is used to align the

exfoliated array with the desired location on the target substrate. The full details of this procedure are described in reference [9]. After mounting the exfoliated sample, together with the FEP-backed adhesive, to the SiO₂ substrate, the adhesive is melted using a hot plate at 90 °C for 90 seconds, encapsulating the transferred TMDC array. The FEP film is then peeled off manually, and the melted adhesive is removed with a 10-minute acetone bath. A relatively low-power (15 W) O₂ plasma cleaning step is performed to remove any polymer residues on the sample (15 seconds at 300 mTorr, Plasma Equipment Technical Services, Inc.). As before, the epitaxial Au layer was removed with a 2-minute immersion in a KI/I₂ etchant (Transene Gold Etchant Type TFA), followed by rinsing with DI water.

5.3.3 TFSI superacid treatment steps

Bistriflimide, systematically known as bis(trifluoromethane)sulfonimide (TFSI), is a non-coordinating anion with the chemical formula $[(CF_3SO_2)_2N]^-$. The exfoliated monolayer MoS₂ flakes, mounted to a SiO₂/Si substrate, was treated in a 0.2 mg/mL solution of TFSI (Sigma-Aldrich), in a solvent composed of a 10:9 ratio of 1,2-dichloroethane (DCE, Sigma-Aldrich) and 1,2-dichlorobenzene (DCB, Sigma-Aldrich). The chip was submerged in this solution for 10 minutes in a sealed vial in an inert argon environment at room temperature and 1 atm of pressure, then removed and dried with N₂ gas without rinsing.

5.3.4 Photoluminescence spectroscopy instrumentation and analysis methods

The photoluminescence (PL) spectroscopy setup used to characterize the transferred MoS₂, WS₂, and heterostructures thereof was a custom micro-PL system comprised of a Lexel 95 second harmonic generation (SHG) argon-ion laser, with a wavelength of λ : 514.5 nm and a maximum output power of 2.4 Watts. For the above analysis, the laser was operated at a power of 300 mW and filtered to 0.35 – 0.37 mW. The laser was focused onto the sample through a 50x objective lens with a numerical aperture (NA) of 0.8 and resulting in an incident spot size (at FWHM) of 1.1 μm^2 and an incident laser power of 25 – 27 μW . This incident power was calibrated at high illumination intensity using a S120C standard photo-diode power meter from ThorLabs. A ‘dark’ spectrum was subtracted from each measurement by first collecting a measurement of equal integration time without any laser illumination.

In order to collect PL imaging data, the samples were illuminated with a GaInN LED with a wavelength, λ , of 450 nm at an incident power of 170 μW , corresponding to a power density of 65 $\mu\text{W}/\text{mm}^2$. The illuminated area had a diameter of 1.8 mm. A 10x objective lens was used, which had a numerical aperture of 0.3. Returning photoluminescence signal passed through this same objective and then through a 500-nm long-pass filter to remove specular reflections from the excitation laser beam. Photon counts were dispersed by an $f = 340$ mm spectrometer with a 150 g/mm grating. An iDus BEX2-DD Si CCD camera from Andor was used to record the PL imaging data.

Photoluminescence spectral data were analyzed in Wolfram Mathematica in order to find local maxima (peaks), assess relative intensities across different samples, and perform calculations. Imaging data from overlapping sample areas were overlaid, merged, and colorized in Adobe Photoshop.

5.4 Chapter 5 Summary

In this chapter, the detailed experimental procedures for two iterations of a monolayer-selective, patterned exfoliation process are described, the results of which were characterized using photoluminescence (PL) spectroscopy. PL spectroscopy is confirmed as a straightforward way to test the monolayer character of a given MoS_2 or WS_2 sample. It is also shown to serve as a relative indicator of the quality of a monolayer of MoS_2 or WS_2 , given by the ratio of the A-exciton peak to the B-exciton peak, as well as by the presence of small peak shifts from the theoretical peak energies. A TFSI superacid treatment is performed to successfully passivate sulfur vacancies in the transition metal disulfides and thereby enhance the quantum yield, illustrated by the 25-100x improvement in luminescence intensity.

Bibliography

- [1] Gábor Zsolt Magda, János Petó, Gergely Dobrik, Chanyong Hwang, László P. Biró, and Levente Tapasztó. “Exfoliation of large-area transition metal chalcogenide single layers”. In: *Scientific Reports* 5.1 (2015), p. 14714. ISSN: 2045-2322. DOI: 10.1038/srep14714.
- [2] Kin Fai Mak, Changgu Lee, James Hone, Jie Shan, and Tony F. Heinz. “Atomically thin MoS₂: A new direct-gap semiconductor”. In: *Physical Review Letters* 105.13 (2010), pp. 2–5. ISSN: 00319007. DOI: 10.1103/PhysRevLett.105.136805. eprint: 1004.0546.
- [3] Oriol Lopez-Sanchez, Dominik Lembke, Metin Kayci, Aleksandra Radenovic, and Andras Kis. “Ultrasensitive photodetectors based on monolayer MoS₂”. In: *Nature Nanotechnology* 8.7 (2013), pp. 497–501. ISSN: 1748-3387. DOI: 10.1038/nnano.2013.100.
- [4] Qing Hua Wang, Kouros Kalantar-Zadeh, Andras Kis, Jonathan N Coleman, and Michael S Strano. “Electronics and optoelectronics of two-dimensional transition metal dichalcogenides”. In: *Nature Nanotechnology* 7.11 (2012), pp. 699–712. ISSN: 1748-3387. DOI: 10.1038/nnano.2012.193. eprint: 1205.1822.
- [5] Hai Li, Jumiati Wu, Zongyou Yin, and Hua Zhang. “Preparation and applications of mechanically exfoliated single-layer and multilayer MoS₂ and WSe₂ nanosheets”. In: *Accounts of Chemical Research* 47.4 (2014), pp. 1067–1075. ISSN: 15204898. DOI: 10.1021/ar4002312.
- [6] Sujay B. Desai, Surabhi R. Madhvapathy, Matin Amani, Daisuke Kiriya, Mark Hettick, Mahmut Tosun, Yuzhi Zhou, Madan Dubey, Joel W. Ager, Daryl Chrzan, and Ali Javey. “Gold-Mediated Exfoliation of Ultralarge Optoelectronically-Perfect Monolayers”. In: *Advanced Materials* 28.21 (2016), pp. 4053–4058. ISSN: 15214095. DOI: 10.1002/adma.201506171.
- [7] Matěj Velický, Gavin E. Donnelly, William R. Hendren, Stephen McFarland, Declan Scullion, William J. I. DeBenedetti, Gabriela Calinao Correa, Yimo Han, Andrew J. Wain, Melissa A. Hines, David A. Muller, Kostya S. Novoselov, Héctor D. Abruña, Robert M. Bowman, Elton J. G. Santos, and Fumin Huang.

- “Mechanism of Gold-Assisted Exfoliation of Centimeter-Sized Transition-Metal Dichalcogenide Monolayers”. In: *ACS Nano* 12.10 (Oct. 2018), pp. 10463–10472. ISSN: 1936-0851. DOI: 10.1021/acsnano.8b06101.
- [8] Hannah M. Gramling, Clarissa M. Towle, Sujay B. Desai, Haoye Sun, Evan C. Lewis, Vu D. Nguyen, Joel W. Ager, Daryl Chrzan, Eric M. Yeatman, Ali Javey, and Hayden Taylor. “Spatially Precise Transfer of Patterned Monolayer WS₂ and MoS₂ with Features Larger than 10⁴ μm² Directly from Multilayer Sources”. In: *ACS Applied Electronic Materials* 1 (2019), pp. 407–416. ISSN: 2637-6113. DOI: 10.1021/acsaelm.8b00128.
- [9] Vu Nguyen, Hannah Gramling, Clarissa Towle, Wan Li, Der-Hsien Lien, Hyungjin Kim, Daryl C. Chrzan, Ali Javey, Ke Xu, Joel Ager, and Hayden Taylor. “Deterministic Assembly of Arrays of Lithographically Defined WS₂ and MoS₂ Monolayer Features Directly From Multilayer Sources Into Van Der Waals Heterostructures”. In: *Journal of Micro and Nano-Manufacturing* 7.4 (2019), pp. 1–8. ISSN: 2166-0468. DOI: 10.1115/1.4045259.
- [10] Andrea Splendiani, Liang Sun, Yuanbo Zhang, Tianshu Li, Jonghwan Kim, Chi Yung Chim, Giulia Galli, and Feng Wang. “Emerging photoluminescence in monolayer MoS₂”. In: *Nano Letters* 10.4 (2010), pp. 1271–1275. ISSN: 15306984. DOI: 10.1021/nl903868w.
- [11] M. Amani, D.-H. Lien, Daisuke Kiriya, J. Xiao, A. Azcatl, J. Noh, Surabhi R Madhvapathy, R. Addou, S. Kc, M. Dubey, K. Cho, R. M. Wallace, S.-C. Lee, J.-H. He, J. W. Ager, X. Zhang, E. Yablonovitch, and A. Javey. “Near-unity photoluminescence quantum yield in MoS₂”. In: *Science* 350.6264 (2015), pp. 1065–1068. ISSN: 0036-8075. DOI: 10.1126/science.aad2114.
- [12] Cindy S. Merida, Duy Le, Elena M. Echeverria, Ariana E. Nguyen, Takat B. Rawal, Sahar Naghibi Alvillar, Viktor Kandyba, Abdullah Al-Mahboob, Yaroslav Losovyj, Khabiboulakh Katsiev, Michael D. Valentin, Chun Yu Huang, Michael J. Gomez, I. Hsi Lu, Alison Guan, Alexei Barinov, Talat S. Rahman, Peter A. Dowben, and Ludwig Bartels. “Gold Dispersion and Activation on the Basal Plane of Single-Layer MoS₂”. In: *Journal of Physical Chemistry C* 122.1 (2018), pp. 267–273. ISSN: 19327455. DOI: 10.1021/acs.jpcc.7b07632.
- [13] Humberto R. Gutiérrez, Nestor Perea-López, Ana Laura Elías, Ayse Berkdemir, Bei Wang, Ruitao Lv, Florentino López-Urías, Vincent H. Crespi, Humberto Terrones, and Mauricio Terrones. “Extraordinary Room-Temperature Photoluminescence in Triangular WS₂ Monolayers”. In: *Nano Letters* 13.8 (2013), pp. 3447–3454. ISSN: 1530-6984. DOI: 10.1021/nl3026357.

- [14] Hyungjin Kim, Geun Ho Ahn, Joy Cho, Matin Amani, James P. Mastandrea, Catherine K. Groschner, Der Hsien Lien, Yingbo Zhao, Joel W. Ager, Mary C. Scott, Daryl C. Chrzan, and Ali Javey. “Synthetic WSe₂ monolayers with high photoluminescence quantum yield”. In: *Science Advances* 5.1 (2019), pp. 1–8. ISSN: 23752548. DOI: 10.1126/sciadv.aau4728.
- [15] Matin Amani, Peyman Taheri, Rafik Addou, Geun Ho Ahn, Daisuke Kiriya, Der Hsien Lien, Joel W. Ager, Robert M. Wallace, and Ali Javey. “Recombination Kinetics and Effects of Superacid Treatment in Sulfur- and Selenium-Based Transition Metal Dichalcogenides”. In: *Nano Letters* 16.4 (2016), pp. 2786–2791. ISSN: 15306992. DOI: 10.1021/acs.nanolett.6b00536.
- [16] Yi Zeng, Weibing Chen, Bin Tang, Jianhui Liao, Jun Lou, and Qing Chen. “Synergetic photoluminescence enhancement of monolayer MoS₂ via surface plasmon resonance and defect repair”. In: *RSC Advances* 8.42 (2018), pp. 23591–23598. ISSN: 2046-2069. DOI: 10.1039/C8RA03779E.

Chapter 6

Summary: the Complex Au-MoS₂ landscape

6.1 Current opportunities and pitfalls in 4D STEM

There is tremendous opportunity in 4D STEM as a method for analyzing large areas of materials with a nanoscale characterization tool. In recent years, microscope software giant Gatan has starting offering 4D STEM capability as a small, add-on piece of hardware, with a built-in tool in their ubiquitous DigitalMicrograph software package, working directly with my collaborators at the National Center for Electron Microscopy[1]. This is to say that high-throughput data collection and analysis in electron microscopy is still in its early days. Soon, it will be the default mode of operation for ‘workhorse’ diffraction experiments due to the unprecedented level of detail that can be recorded in a single session. The wide adoption of 4D STEM as a technique is especially useful to the majority of microscopists who share instrument time with others, as 4D STEM allows a greater share of analysis to be performed *ex post facto*, and decreasing the likelihood of returning to the same sample multiple times for additional measurements.

At present, 4D STEM remains a method primarily useful for analysis of single crystals, or of heterostructures with sharp borders that lie perpendicular to the beam direction (as opposed to along the beam direction). Analysis efforts are significantly hampered by the overlapping or co-location of diffraction disks corresponding to different materials. Overlapping can be reduced or avoided by using a more parallel probe, thus reducing the diameter of the diffraction disks and increasing the measurement precision, but this necessarily increases the interaction cross-section of the sample and reduces the spatial resolution of the measurement.

It is tempting to think of crystal domains as uniform or as following a general rule, but often, real systems exhibit defects and symmetry-breaking deformations. There were many areas of the prepared Au-MoS₂ samples where both materials were confirmed to be present using EDS, yet the diffraction patterns from those regions were so confused as to be inscrutable. The reality is that there are numerous factors which could make it difficult for trained microscopists to fully interpret a given diffraction pattern, let alone many tens of thousands, with confidence. Principal among these are the uncertain or high thickness of the sample, the presence of contamination, and the lack of alignment along or near a known zone axis, followed in relevance by having multiple materials present, a lower degree of crystallinity, and non-uniformities in the sample. Each of these factors present an additional challenge for the automated analysis of large diffraction datasets. As detector speeds continue to increase and researchers increase scan sizes, leading to a likely avalanche of 4D STEM datasets, considerable effort should be directed to the identification and resolution of these factors. Without such an effort, a majority of 4D STEM data may end up woefully under-analyzed, and hidden insights left buried in TB-sized troves of pixel values.

6.2 Synopsis of discoveries

The following sections will summarize several takeaways from the studies included in this dissertation. First, in section 6.2.1, it is stated that data from nanobeam electron diffraction and both moderate and atomic-resolution dark-field STEM imaging support the hypothesis that gold grows on MoS₂(0001) with its [111] vector normal to the heteroepitaxial interface. However, an axial rotation about this vector direction on the order of 1-3° can occasionally arise in Au domains ranging from 5-15 nm in diameter. The occurrence and semi-continuous nature of this azimuthal rotation is reported. Gold is found to exhibit growth morphologies on natural mined MoS₂ surfaces ranging from triangular and truncated triangular crystallites to a semi-coalesced, nanoporous matrix.

6.2.1 Au-MoS₂ epitaxy and rotation

The first aim of this study was to determine the lattice relationship between a deposited Au thin film and single-crystal MoS₂, both as a free-standing monolayer and as a few-layer material. The conceivable possibilities were A) non-epitaxy, B)

incommensurate epitaxy, C) commensurate epitaxy, or D) a novel interfacial reconstruction. Both incommensurate epitaxy and a rotated interfacial reconstruction were found.

Where an epitaxial alignment could be determined in HR-STEM or nanobeam electron diffraction, Au was typically oriented such that the (111) plane was the interfacial layer on top of the $\text{MoS}_2(0001)$ surface, and such that the Au $[01\bar{1}]$ direction was parallel or nearly parallel to the $[11\bar{2}0]$ direction of MoS_2 . In some samples examined, there is convincing evidence that azimuthal rotations of several degrees from the expected $\text{MoS}_2(0001)\parallel\text{Au}(111)$; $\text{MoS}_2[11\bar{2}0]\parallel\text{Au}[01\bar{1}]$ alignment were observed.

Experimental data appearing to show an interplanar rotation between two epitaxial species may suffer from a key ambiguity: whether the diffraction spot placement truly indicates rotation, or whether that spot is one of a set of superstructure peaks that form satellite disks around the dominant diffraction disks. Figure 6.1 shows several simulated diffraction patterns for an Au crystallite on MoS_2 , illustrating how two distinct scenarios could produce similar diffraction patterns, but subtle differences can aid in their disambiguation.

Any consistent atomic arrangement lay at a local minimum in the free energy of the crystal. It must be the case, then, that a slight azimuthal rotation between Au and MoS_2 reduces the strain energy of the system. It is possible that this epitaxial misalignment is a result of the growth behavior of Au on MoS_2 . Others have suggested that Au crystal nuclei smaller than the equilibrium dislocation defect density (about 3-4 nm in diameter) may be strained in tension according to the MoS_2 substrate lattice[2]. A combination of misfit dislocations may result in a rotation of the Au crystal as it continues to coarsen. When the Au islands begin to coalesce with one another, their lattices may also rearrange with a certain curvature in order to decrease the interfacial energy between the grains.

This idea that rotations will arise in Au islands during non-equilibrium growth, satisfying a local energy minimum rather than a global minimum, agrees with previous reports of ‘correcting’ epitaxial misalignment through annealing[3]. In this dissertation, a small proportion of samples were annealed (Fig. D.4), and in those samples, no rotation was observed between the Au and the MoS_2 . It would be an interesting avenue for future studies to investigate the temperature conditions required to recrystallize or relax the twisted gold grains.

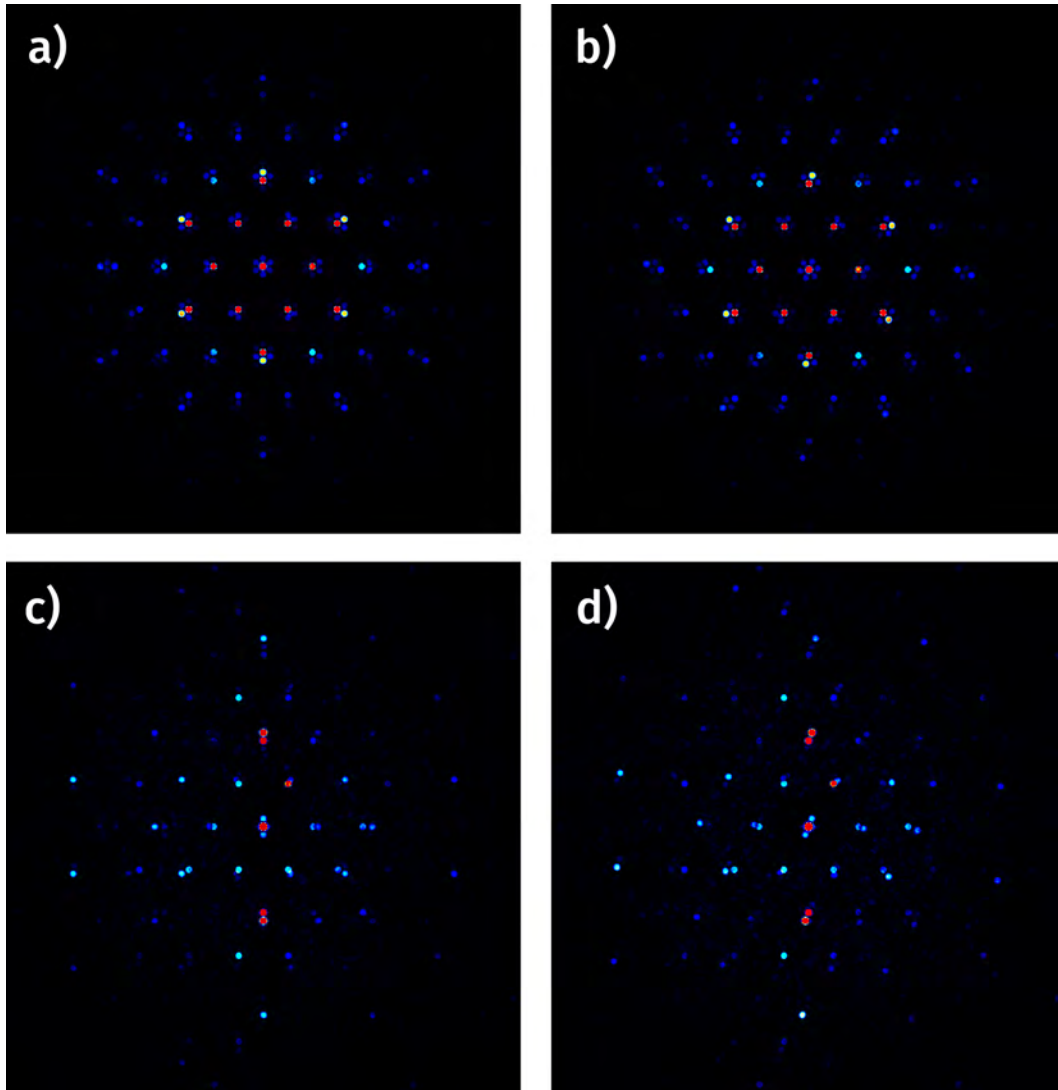


Figure 6.1: Color-scaled simulated diffraction patterns for a virtual sample comprised of 10 planes of Au(111), forming a faceted truncated triangular crystallite, epitaxially aligned on top of 10-layer MoS₂. a) Diffraction disks from each crystal species are clearly visible, as well as the hexagonal superstructure diffraction disks. b) Diffraction pattern where the Au crystallite was rotated azimuthally by 2° relative to the MoS₂ substrate. c) Diffraction pattern where the entire sample was tilted by 6° about the x-axis (as an off-zone measurement). d) Diffraction pattern where the Au crystallite was rotated about the z-axis by 2° relative to the underlying MoS₂ and the entire sample was also tilted by 6° about the x-axis.

6.2.2 On searching for Au-MoS₂ epitaxial strain in a TEM

An open question during these investigations was whether or not the epitaxial relationship between gold and molybdenum disulfide would also form a coherent or semi-coherent interface, termed ‘coherent epitaxy’. Due to the weak van der Waals bonds between layers of multilayer MoS₂ that enable its use in industry as a dry lubricant, it is unlikely that any coherent interface would significantly constrain the layers beneath the contact layer. The question, then, is how and whether it can be determined if there are strains present in the surface layer of MoS₂ that are not present in the layers below.

In theory, these three possible lattices – the bulk MoS₂, the surface monolayer of MoS₂, and the Au – could be distinguished by using a converged electron probe with the spatial resolution to isolate the materials stack underneath a gold crystallite grown on a multilayer MoS₂ substrate. Since a diffraction pattern of several materials incident on one another can usually be approximated as the superposition of those materials’ individual diffraction patterns, then it may be possible to determine whether *two* reciprocal lattices are distinguishable (typical epitaxy) – or *three* (indicating a decoupled coherent epitaxial condition).

In practice, however, difficulties in sample preparation made finding this ‘Goldilocks’ sample a challenge unto its own, separate from the optimization problem of determining the ideal microscope parameters to resolve three possible lattices in close vicinity. The density of the deposited gold, and the heavier atomic weight of Au compared to Mo and S, meant that even a few unit cell thicknesses of gold would overwhelm the STEM contrast from the MoS₂ lattice underneath, let alone that from a possible decoupled interfacial monolayer.

In diffraction mode, too, the weak signal of such a decoupled layer may be imperceptible among the strongly-diffracted Au peaks, particularly the forbidden reflections which appear in the pattern when Au is very thin. Naturally, if the Au were thicker, these forbidden reflections may disappear, but the dominant Au peaks would further wash out the intensity from a single layer of MoS₂. We find ourselves, then, between a rock and a hard place. The diffraction signal could be concentrated and the signal-to-noise ratio improved by using a more parallel beam; however, then the illuminated area would necessarily be larger than the Au features observed, and effects of rippling may impede the analysis of that data as well.

6.3 Looking to the future

The Au-MoS₂ system continues to draw significant attention as a model for understanding the interaction of two-dimensional (2D) semiconductors and metals. A specific area of interest is the epitaxy of one on the other, which is highly relevant to the design of effective metal contacts in thin-film electronics, and which has been credited for significant advances in the size and quality of exfoliated 2D materials. Namely, Au epitaxy on MoS₂ and WS₂ has been shown empirically to enhance the yield of exfoliated monolayers from a bulk crystal.

The presence of nanoscale features in deposited Au thin films on MoS₂ suggests that a characterization method with high spatial resolution is required to probe highly localized strain environments. The presence of localized strains in MoS₂ would affect bulk material properties and, separately, create the opportunity for nanoscale devices based on the spatial modulation of strain-sensitive properties (such as the band gap). Currently, only a handful of techniques offer the spatial resolution necessary to probe structural differences on the scale of a nanometer or less. One of these is TEM, which offers a suite of methods for investigating a wide array of materials and properties. Nanobeam electron diffraction, employed in this work, was chosen in order to search for potential high-magnitude strains (> 1%) with the advantages of high spatial resolution and high precision. However, to reliably measure nano-localized strains which may have a magnitude below 0.1%, and especially in a heteroepitaxial system such as Au-MoS₂, distinct TEM-based methods which incorporate 3D information such as converged beam electron diffraction (CBED)[4, 5] or precession electron diffraction (PED)[6, 7] may yield more conclusive results.

In situ growth of Au on MoS₂ performed in a TEM would provide a fascinating view into the evolution of the islands and nanoporous Au reported in Section 3.7[8]. The same area, and the same diffraction pattern, could be monitored in real-time during Au growth in order to characterize the sample's epitaxial orientation, interfacial coherence or incoherence, lattice alignment or misalignment, faceting, and ripening. Of specific interest is testing the hypothesis that Au nuclei under a certain critical size may match the atomic spacing of the substrate lattice[2]. *In situ* characterization would be better understood if coupled with computational efforts, such as by utilizing continuum linear elasticity theory and/or density functionary theory, provided that appropriate parameters and potentials can be determined[8–10].

Separate from TEM methods, other characterization techniques capable of nanoscale

resolution may hold the key to measuring epitaxial strain in the Au-MoS₂ system. Scanning probe microscopy, particularly scanning tunneling microscopy, has been used to measure Moiré patterns in TMDC-TMDC and metal-2D material systems, magnifying any differences in lattice spacings and orientations[11, 12]. In addition, photoluminescence spectroscopy, not ordinarily a nanoscale technique, can achieve sub-wavelength, nanoscale resolution by scanning the sample with a specialized 10-nm near-field probe at the tip of an optical fiber[13, 14]. As PL intensity from MoS₂ would be quenched in the presence of even a few Å of Au[9], nano-PL could prove to be useful in verifying whether or not any Au is present in-between deposited epitaxial islands or within the pores of nanoporous Au networks. As a point of comparison, EDS, which was used for chemical identification in this work, is susceptible to low levels of noise across any measured region, resulting in expected ‘false positive’ signals where a given target material is not, in fact, present.

In this work, STEM was chosen for its atomic resolution, analytical depth, and ready interpretation, despite the challenging sample preparation. If a sample can be prepared which is completely ideal, then some further insights may lie in STEM diffraction data. This experiment is most straightforward with a sample that consists of an isolated flake of monolayer MoS₂ upon which Au has been evaporated. Such monolayer flakes are rare in samples prepared using stochastic exfoliation, such as those used for the STEM studies in this work. It would therefore be judicious for a future researcher to either use a monolayer-selective exfoliation method, taking care not to damage the TEM grid, or to transfer onto a TEM grid a monolayer of MoS₂ that was grown by chemical vapor deposition (CVD), for which recipes have been well-calibrated. Alternatively, some studies have successfully grown MoS₂ directly onto TEM-compatible substrates, avoiding the need for a transfer method[15]. Au could then be deposited onto these MoS₂ surfaces and analyzed via TEM.

HR-STEM imaging offers readily-interpretable measurement of atomic positions in real space. Provided that an appropriate monolayer MoS₂ sample with evaporated gold is prepared, with thin enough islands of Au so as to retain a sufficient signal-to-noise ratio to resolve the underlying MoS₂ layer, then the MoS₂ lattice can be observed under both free-standing and thin film epitaxial conditions. I would recommend the use of a well-calibrated tomography stage in order to more easily align the sample along a high-symmetry direction, without translating the sample too drastically during stage rotation. The most significant drawback of measuring strain using HR-STEM is the limited field of view afforded by the high magnification. Of course, this one again points to 4D STEM as a means of collecting highly detailed

data over unconventionally large length scales.

Indeed, the biggest opportunity I see in the TEM space is in the high-throughput analysis of 4D STEM diffraction data. The microscopy community is rapidly embracing emerging techniques from data science and machine learning, and the ability to both collect and analyze unprecedented amounts of finely detailed data about the materials we study will surely unlock our ability to control the nano-scale world. In this era, where the fastest 4D STEM detector can count individual electrons as they hit the detector, scanning across micron-sized areas of samples and collecting terabytes of data in minutes, the computational memory and bandwidth will become our only limitations.

Bibliography

- [1] Gatan Inc. www.gatan.com/techniques/4d-stem. *4D STEM*. 2021.
- [2] Yuzhi Zhou, Daisuke Kiriya, E. E. Haller, Joel W. Ager, Ali Javey, and D. C. Chrzan. “Compliant substrate epitaxy: Au on MoS₂”. In: *Physical Review B* 93.5 (Feb. 2016), p. 054106. DOI: 10.1103/PhysRevB.93.054106. arXiv: 1505.07505.
- [3] Anna C. Domask, Kayla A. Cooley, Bernd Kabius, Michael Abraham, and Suzanne E. Mohny. “Room Temperature van der Waals Epitaxy of Metal Thin Films on Molybdenum Disulfide”. In: *Crystal Growth and Design* 18.6 (2018), pp. 3494–3501. ISSN: 15287505. DOI: 10.1021/acs.cgd.8b00257.
- [4] A. Béché, J. L. Rouvière, J. P. Barnes, and D. Cooper. “Strain measurement at the nanoscale: Comparison between convergent beam electron diffraction, nano-beam electron diffraction, high resolution imaging and dark field electron holography”. In: *Ultramicroscopy* 131.2013 (2013), pp. 10–23. ISSN: 03043991. DOI: 10.1016/j.ultramicro.2013.03.014.
- [5] W. Zhao, G. Duscher, G. Rozgonyi, M. A. Zikry, S. Chopra, and M. C. Ozturk. “Quantitative nanoscale local strain profiling in embedded SiGe metal-oxide-semiconductor structures”. In: *Applied Physics Letters* 90.19 (2007), pp. 1–3. ISSN: 00036951. DOI: 10.1063/1.2738188.
- [6] Jean Luc Rouviere, Armand Béché, Yannick Martin, Thibaud Denneulin, and David Cooper. “Improved strain precision with high spatial resolution using nanobeam precession electron diffraction”. In: *Applied Physics Letters* 103.24 (2013), pp. 1–4. ISSN: 00036951. DOI: 10.1063/1.4829154.
- [7] M. P. Vigouroux, V. Delaye, N. Bernier, R. Cipro, D. Lafond, G. Audoit, T. Baron, J. L. Rouvière, M. Martin, B. Chenevier, and F. Bertin. “Strain mapping at the nanoscale using precession electron diffraction in transmission electron microscope with off axis camera”. In: *Applied Physics Letters* 105.19 (2014), pp. 8–11. ISSN: 00036951. DOI: 10.1063/1.4901435.

- [8] Boao Song, Kun He, Yifei Yuan, Soroosh Sharifi-Asl, Meng Cheng, Jun Lu, Wissam A. Saidi, and Reza Shahbazian-Yassar. “In situ study of nucleation and growth dynamics of Au nanoparticles on MoS₂ nanoflakes”. In: *Nanoscale* 10.33 (2018), pp. 15809–15818. ISSN: 20403372. DOI: 10.1039/c8nr03519a.
- [9] Cindy S. Merida, Duy Le, Elena M. Echeverria, Ariana E. Nguyen, Takat B. Rawal, Sahar Naghibi Alwillar, Viktor Kandyba, Abdullah Al-Mahboob, Yaroslav Losovyj, Khabiboulakh Katsiev, Michael D. Valentin, Chun Yu Huang, Michael J. Gomez, I. Hsi Lu, Alison Guan, Alexei Barinov, Talat S. Rahman, Peter A. Dowben, and Ludwig Bartels. “Gold Dispersion and Activation on the Basal Plane of Single-Layer MoS₂”. In: *Journal of Physical Chemistry C* 122.1 (2018), pp. 267–273. ISSN: 19327455. DOI: 10.1021/acs.jpcc.7b07632.
- [10] Peng Shao, Li Ping Ding, and Feng Ding. “Mechanism of MoS₂ Growth on a Au(111) Surface: An Ab Initio Molecular Dynamics Study”. In: *Chemistry of Materials* 33.9 (2021), pp. 3241–3248. ISSN: 15205002. DOI: 10.1021/acs.chemmater.1c00116.
- [11] Chendong Zhang, Chih Piao Chuu, Xibiao Ren, Ming Yang Li, Lain Jong Li, Chuanhong Jin, Mei Yin Chou, and Chih Kang Shih. “Interlayer couplings, Moiré patterns, and 2D electronic superlattices in MoS₂/WSe₂ heterobilayers”. In: *Science Advances* 3.1 (2017), pp. 1–8. ISSN: 23752548. DOI: 10.1126/sciadv.1601459.
- [12] Zhiyu Zou, Laerte L. Patera, Giovanni Comelli, and Cristina Africh. “Strain release at the graphene-Ni(100) interface investigated by in-situ and operando scanning tunnelling microscopy”. In: *Carbon* 172 (2021), pp. 296–301. ISSN: 00086223. DOI: 10.1016/j.carbon.2020.10.019.
- [13] Wei Bao, Nicholas J. Borys, Changhyun Ko, Joonki Suh, Wen Fan, Andrew Thron, Yingjie Zhang, Alexander Buyanin, Jie Zhang, Stefano Cabrini, Paul D. Ashby, Alexander Weber-Bargioni, Sefaattin Tongay, Shaul Aloni, D. Frank Ogletree, Junqiao Wu, Miquel B. Salmeron, and P. James Schuck. “Visualizing nanoscale excitonic relaxation properties of disordered edges and grain boundaries in monolayer molybdenum disulfide”. In: *Nature Communications* 6.May (2015), pp. 1–7. ISSN: 20411723. DOI: 10.1038/ncomms8993.
- [14] D. Frank Ogletree, P. James Schuck, Alexander F. Weber-Bargioni, Nicholas J. Borys, Shaul Aloni, Wei Bao, Sara Barja, Jiye Lee, Mauro Melli, Keiko Munechika, Stephan Whitelam, and Sebastian Wickenburg. “Revealing Optical Properties of Reduced-Dimensionality Materials at Relevant Length Scales”.

In: *Advanced Materials* 27.38 (2015), pp. 5693–5719. ISSN: 15214095. DOI: 10.1002/adma.201500930.

- [15] Neha P. Kondekar, Matthew G. Boebinger, Eric V. Woods, and Matthew T. McDowell. “In Situ XPS Investigation of Transformations at Crystallographically Oriented MoS₂ Interfaces”. In: *ACS Applied Materials and Interfaces* 9.37 (2017), pp. 32394–32404. ISSN: 19448252. DOI: 10.1021/acsami.7b10230.

Appendices

The following pages contain additional information regarding the preceding studies, including a proof of concept for using convolutional neural networks in diffraction pattern classification, the microscope parameters for HR-STEM images, the deposition parameters for electron beam evaporation of gold, and additional figures describing a number of MoS₂ and Au-MoS₂ samples and simulations. Raw EDS, HAADF-STEM, and 4D STEM data as well as analysis scripts can be found at the repositories specified in section 2.4.

A. Computer vision for 4D STEM data analysis

In the course of the investigations in this dissertation, artificial intelligence was considered as an avenue to characterize large sample areas through analysis of 4D STEM datasets. Looking towards the future of ‘Big Data’ microscopy, where detailed multimodal datasets will contain terabytes of information, the scientific community will need to avail itself of intelligent, automated, and high-throughput analysis methods beyond that which a single researcher could ever perform.

One interesting direction is the use of machine learning for predictive tasks, such as addressing the backwards/forwards problem in accessing a full set of 3D information from 2D electron diffraction patterns. In order to accomplish high-throughput analysis, I investigated using a machine learning approach to 4D STEM analysis utilizing a convolutional neural network (CNN). A CNN was selected over other types of neural networks because raw images could be used as model inputs, whereas more traditional machine learning algorithms would require feature engineering, or significant pre-processing, in order to extract insights. Rather than essentially hand-coding domain knowledge, by using a CNN, I was able to use arrays of raw pixel values directly from the diffraction camera.

Given high-dimensional input data, the CNN must learn a large number of parameters, or weights, and in order to set those weights, a large amount of labeled data is required. Hand-labeling thousands of experimental images is cumbersome (not to mention the very problem we are trying to avoid), so instead, the CNN was

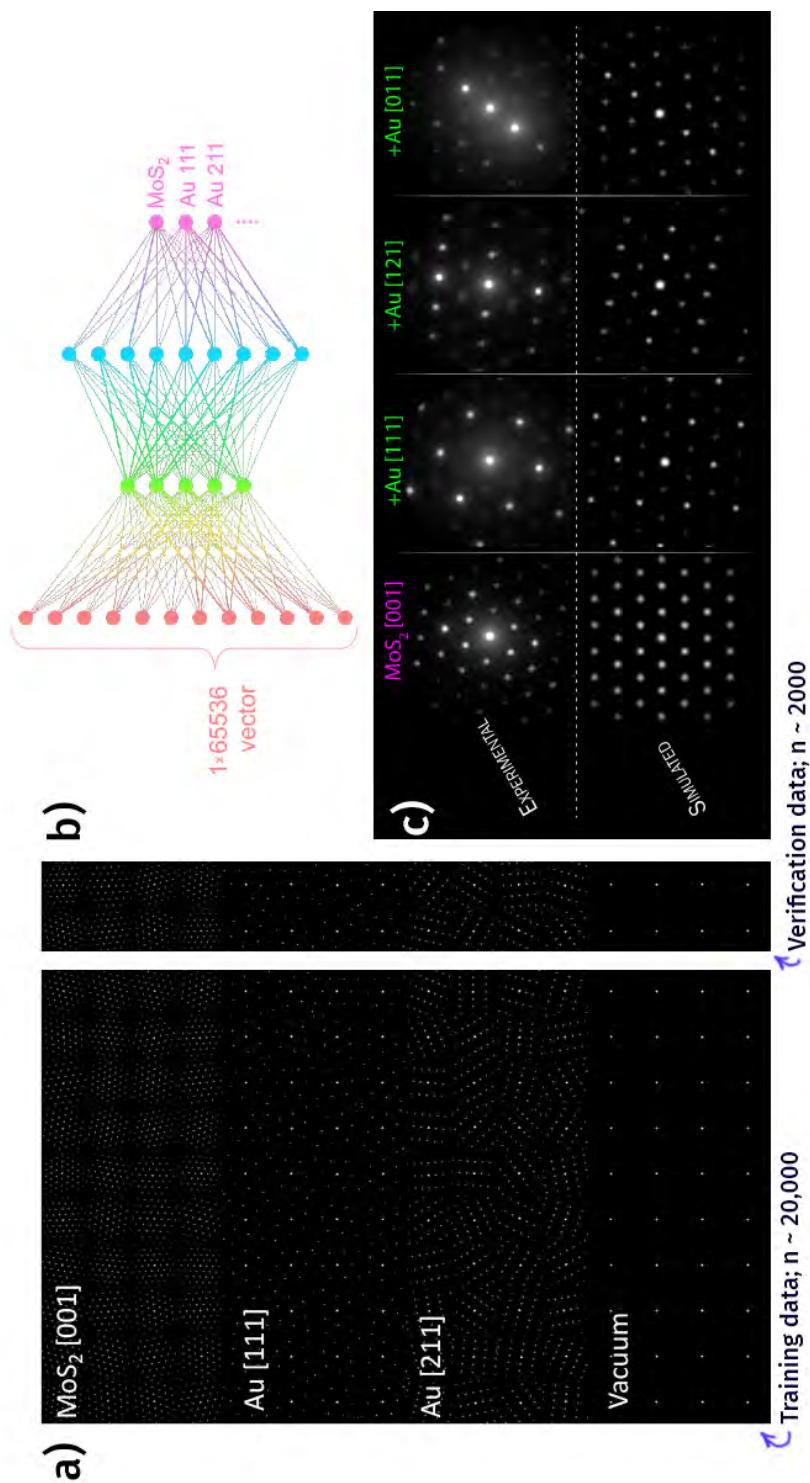


Figure A.1: Training a convolutional neural network (CNN) to classify NBED-STEM electron diffraction patterns. A training set of simulated diffraction patterns were generated for MoS₂[0001], Au[111], Au[211], and the direct probe (without a sample, or 'over vacuum'). a) A subset of the training and verification data used to train the CNN. b) A schematic of the neural network architecture model, with the 65536 pixels in a binned, 256x256 pixel diffraction pattern serving as the input vector, and the crystal classifications as the output vector. c) A comparison of the experimental data to simulated data.

trained on tens of thousands of simulated NBED diffraction patterns of MoS₂ and Au, a subset of which is shown in Figure A.. These simulated patterns had the same dimensions and dynamic range of the experimental diffraction patterns from the TITANX microscope used for a majority of STEM data included in this dissertation.

Since the sample identity is known to be Au-MoS₂ in this case, simulated diffraction patterns were created based on hexagonal and FCC crystal symmetries, using diffraction disks with Gaussian-smoothed edges and a FWHM calibrated using real data. The training data was generalized to account for different microscope parameters such as camera length, STEM rotation, and exposure time, which manifest in a diffraction pattern as magnification, rotation, and intensity (respectively). A degree of randomness was also introduced in the simulated patterns by varying the intensities of symmetric sets of diffraction disks about a Gaussian distribution. To increase the similarity of the simulated patterns to real data, the innermost disks were brightest, with the central spot (the simulated undiffracted beam) retaining the majority of the signal. All simulated diffraction patterns for this mini-project were custom-coded in Wolfram Mathematica.

The CNN was trained to recognize and classify diffraction data based on the presence of different crystal species and orientations (eg., MoS₂ [0001], Au [111], and Au [211]), as shown in Figure A.. An attempt was made to train the model to recognize the co-location of each of these crystals, but this was not optimized. A first step in expanding this study would be to expand the training data to include diffraction patterns from a much wider range of zone axes, and from alternative phases of the materials, such as the 1T phase of MoS₂.

Further expansion of this project could involve training a CNN to characterize the strain state of identified crystals. Ultimately, a robust machine learning model would readily produce at least two deliverables: 1) classification maps of the crystal species and epitaxial relationships across any sample area, and 2) strain maps illustrating the type (e.g., uniaxial, biaxial, isotropic, anisotropic) and degree of strain in MoS₂ across any sample area. Currently, there is no similar work of which I am aware.

B. Atomic-resolution STEM microscope instrumentation

High and atomic-resolution high-angle annular dark field STEM images were collected on the TEAM 0.5 microscope at the National Center for Electron Microscopy

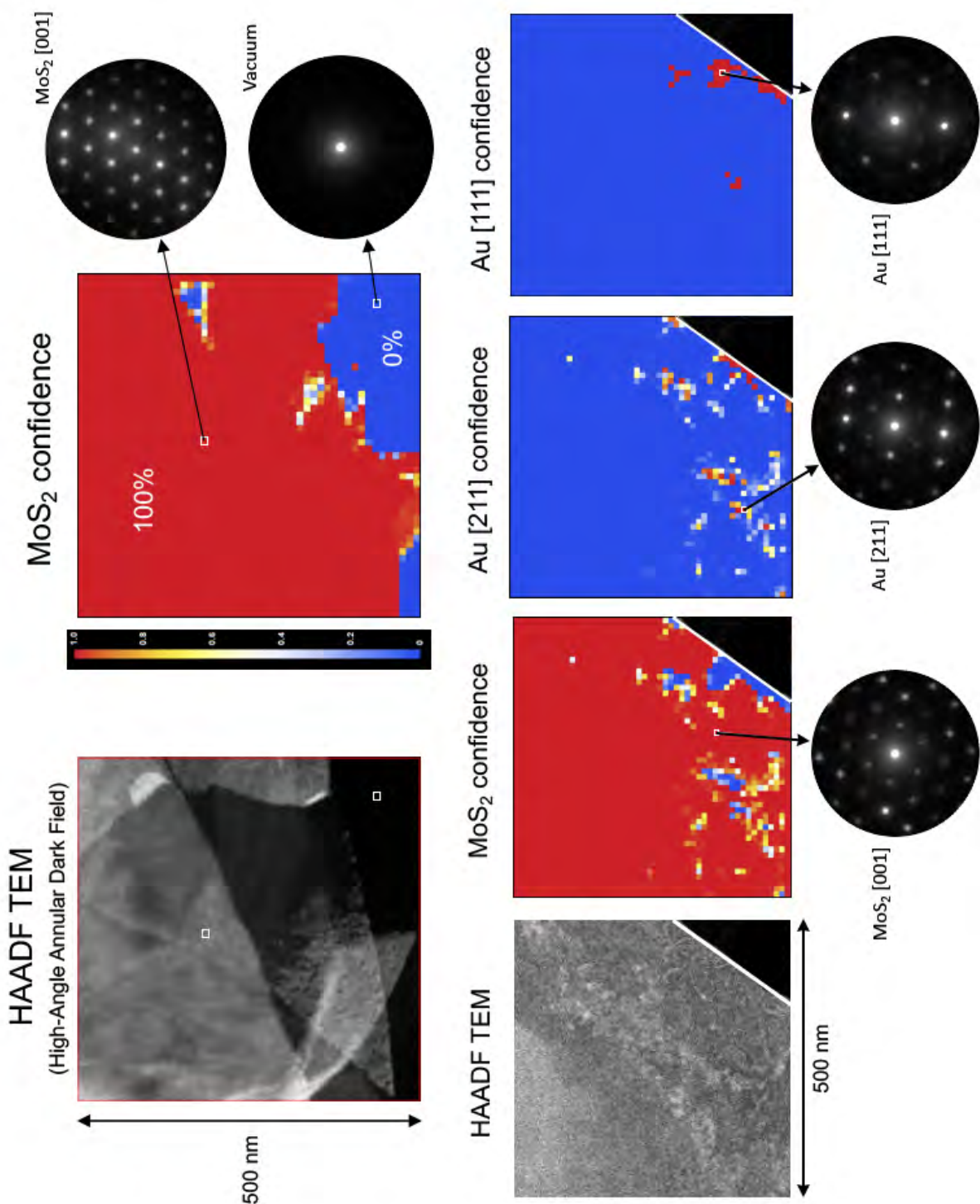


Figure A.2: Output of the CNN classification model. Top row: The HAADF reference image for the 4D STEM dataset and the corresponding confidence map of a model trained only to recognize the presence or absence of MoS₂. Bottom row: The HAADF reference image for the 4D STEM dataset and the corresponding confidence maps of a model trained to classify each image as containing MoS₂, Au[111], or Au[211]. The model was not allowed to select two crystals, so areas of low confidence exist on the borders of the segmented domains.

(NCEM), a facility of the Molecular Foundry at Lawrence Berkeley National Laboratory.

Specifications for this microscope can be found on the NCEM website here:

<https://foundry.lbl.gov/instrumentation/team-0-5/>

The TEAM 0.5 is a double-aberration-corrected transmission electron microscope, aligned first in TEM mode and then aligned and operated in scanning mode for these experiments. The microscope itself is a customized Titan 80-300 microscope (FEI, ThermoFisher Scientific, Pleasanton, CA, USA). The electron source is a high-brightness Schottky-field emission “X-FEG” gun, and the probe is correct using a DCOR spherical-aberration probe corrector from Corrected Electron Optical Systems GmbH (CEOR GmbH, Heidelberg, Germany) and a CETCOR spherical-aberration image corrector (CEOR GmbH, Heidelberg, Germany).

The probe corrector corrects coherent axial aberrations up to the 4th order, spherical aberration up to the 5th order, and six-fold astigmatism. Coherent axial aberrations up to the 3rd order are fully corrected by the image aberration corrector, and 4th and 5th order aberrations are diminished. As such, the TEAM 0.5 is capable of a spatial resolution of 50 pm in both TEM and STEM modes at 300 kV. Operated at 80 kV, some spatial resolution is lost, but is still a very fine 1.4 Å. Images in this dissertation were collected on the TEAM 0.5 at 200 kV and 80 kV.

An important feature of the TEAM 0.5 microscope is the custom all-piezoelectric stage, which has a very stable stage, drifting at only 2 pm/s, to enable atomic resolution imaging.

The electron detector used for high-resolution HAADF-STEM imaging is a Gatan OneView camera, with 4k x 4k pixels.

C. E-beam evaporation deposition parameters

sample	thickness	pressure	current	rate
1	12 nm	1.48 e^{-6} torr	150 mA	1.8 Å/s
2	30 nm	2.00 e^{-6} torr	86 mA	1.6 Å/s
3	15 nm	4.8 e^{-6} torr	46 mA	0.6 Å/s
4	15 nm	2.97 e^{-6} torr	44 mA	0.6 Å/s
5	10 nm	4.83 e^{-6} torr	43.6 mA	0.6 Å/s

Table 1: E-beam evaporation parameters for depositing Au onto MoS₂.

Over the course of the TEM studies in this investigation, only five separate depositions were used to prepare Au-MoS₂ samples. This was to ensure consistency in the data, and to allow me to adjust microscope parameters while controlling for Au evaporation parameters.

For the samples prepared as part of the mechanical exfoliation studies (discussed in 5), depositions of 100 nm and 120 nm of Au were performed.

D. Additional figures

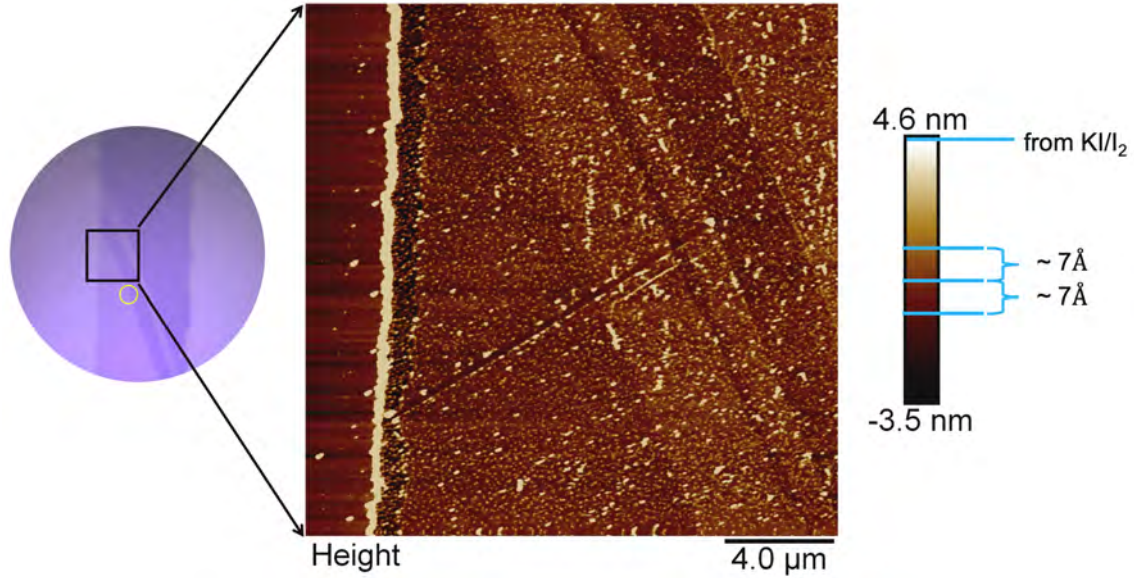


Figure D.3: White light optical microscope image (left) and atomic force microscopy (AFM) height map (right) of a bilayer and monolayer region of a gold-assisted exfoliated MoS₂ flake. Compared to the SiO₂ substrate, one layer of MoS₂ has a height of about 7 Å. An additional step of 7 Å is observed to the bilayer regions. Au nanoparticles about 5 nm in height remain following the KI/I₂ Au etch; their chemical identity was confirmed using x-ray photoelectron spectroscopy (XPS) analysis as discussed in the supplementary information with reference [1].

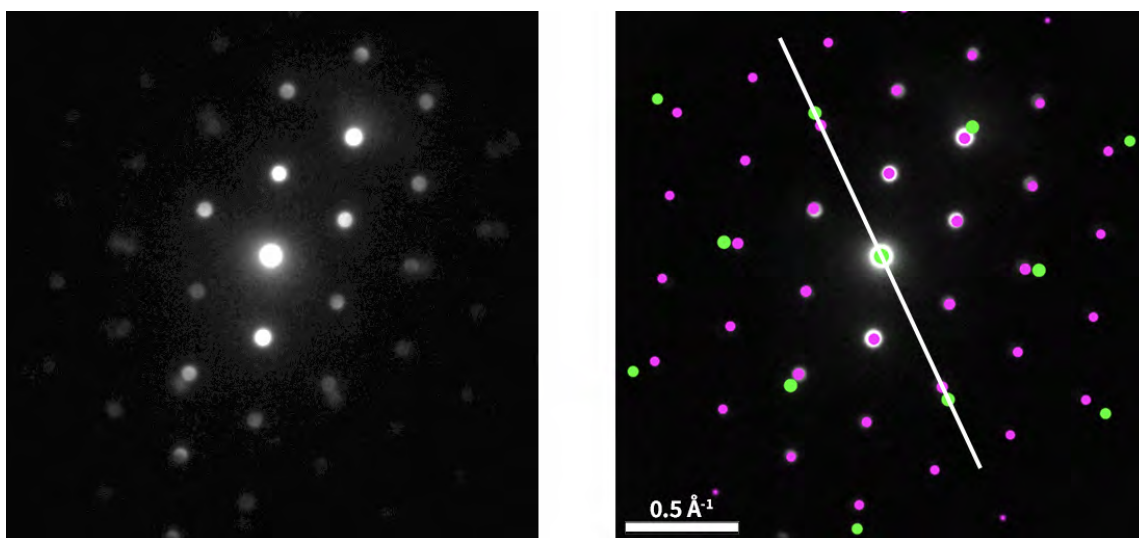


Figure D.4: Single diffraction pattern from a 4D STEM scan of an Au-MoS₂ sample which had been briefly annealed at 120°C for 1 minute. Left: Au(111)-MoS₂(0001) diffraction pattern. Right: Simulated diffraction patterns of Au (green) and MoS₂ (magenta) overlaid on the same experimental diffraction pattern as (Left). No rotational misalignment is identified between the Au and the MoS₂.

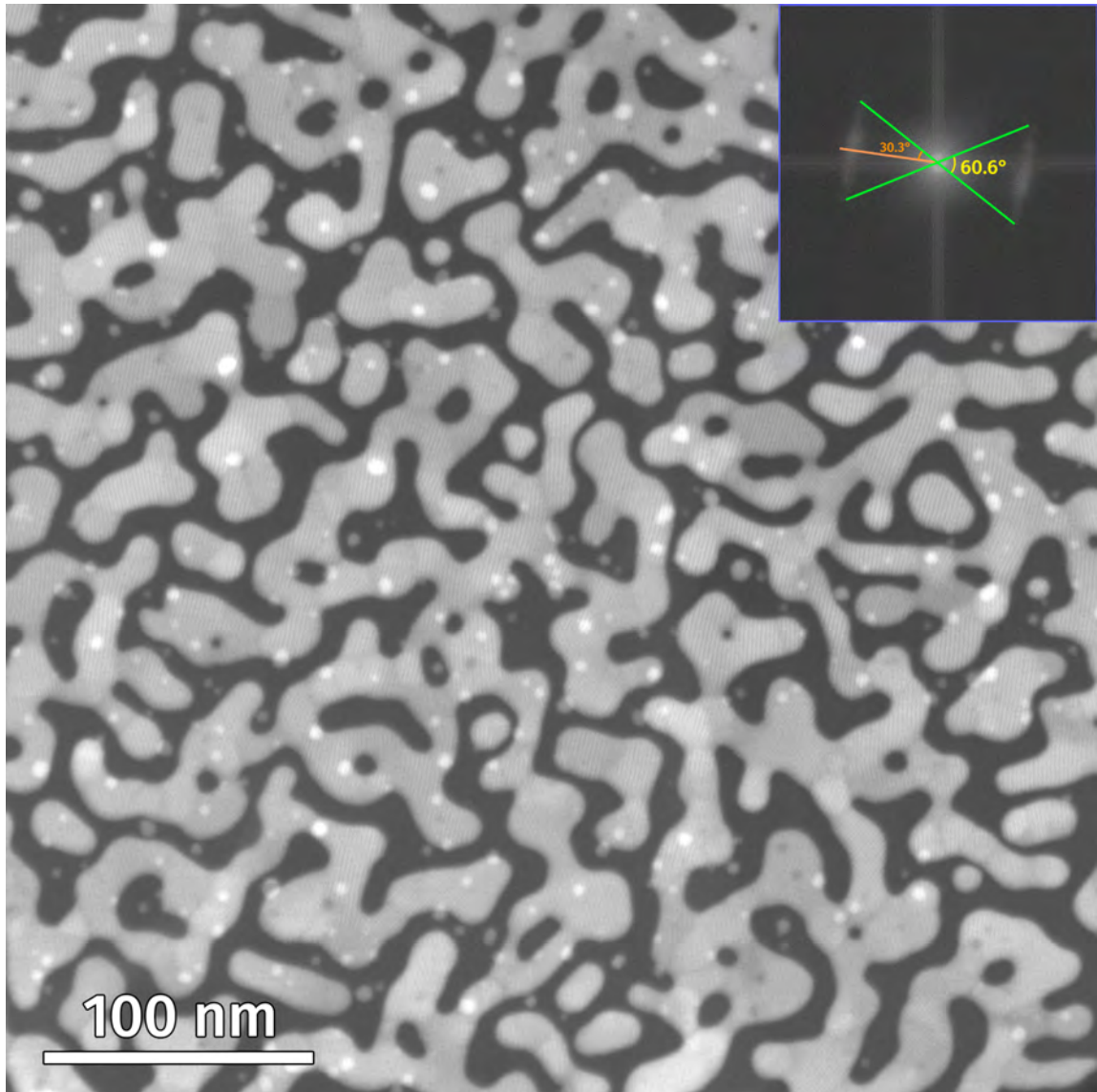


Figure D.5: The FFT (inset) of a HAADF image of nanoporous Au on MoS₂ shows an angular sweep of 60.6°, corresponding to a variation of $\pm 30.3^\circ$. When divided by the Moiré magnification factor for this image, $15.8 \text{ \AA}/1.58 \text{ \AA} = 10$, this yields a real-space angular variation of $\pm 3^\circ$ over the 400-nm Au-MoS₂ sample area above.

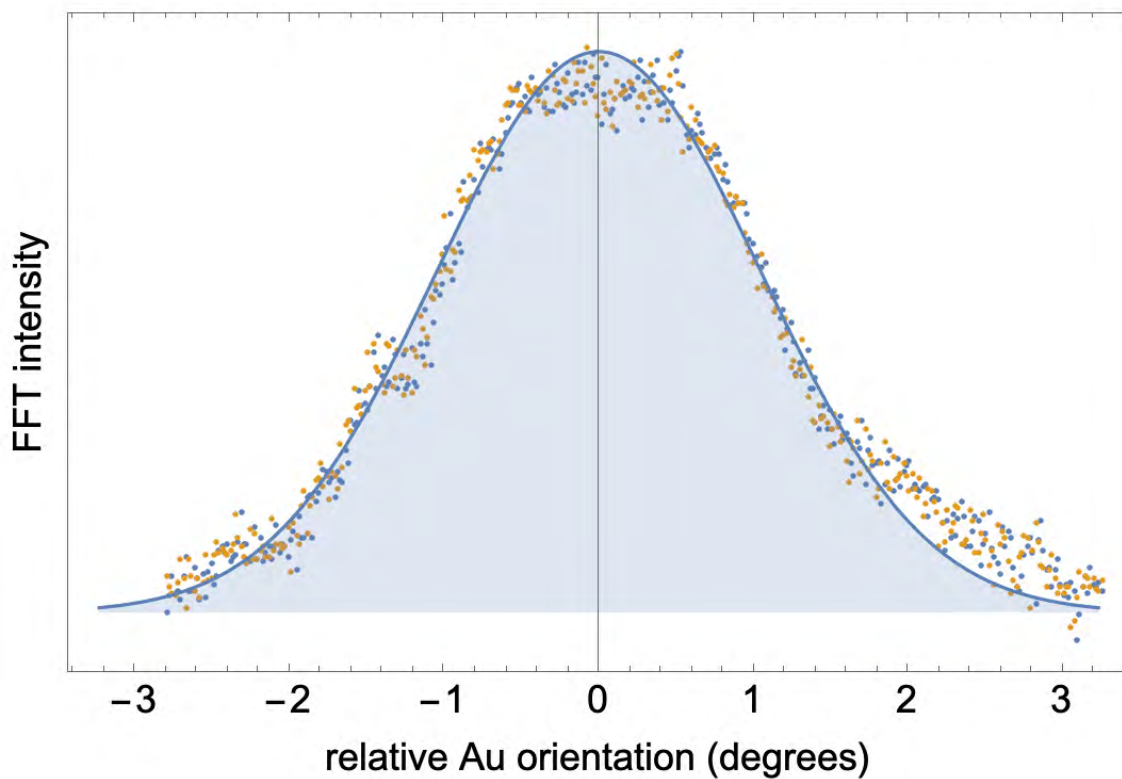


Figure D.6: The angular distribution of Au grains in Fig. D.5. The pixel intensities of the elliptical streaks in the FFT (inset of Fig. D.5) were summed along their minor axes and plotted along their major axes (essentially summing their length-wise line profiles across their widths). The pixel ranges were reassigned values in degrees corresponding to the interior angle of the streak divided by the Moiré magnification factor measured for this sample. The histogram of both reflections is shown alongside a fitted Gaussian distribution with a standard deviation of 1.05° .

Bibliography

- [1] Hannah M. Gramling, Clarissa M. Towle, Sujay B. Desai, Haoye Sun, Evan C. Lewis, Vu D. Nguyen, Joel W. Ager, Daryl Chrzan, Eric M. Yeatman, Ali Javey, and Hayden Taylor. “Spatially Precise Transfer of Patterned Monolayer WS₂ and MoS₂ with Features Larger than 10⁴ μm² Directly from Multilayer Sources”. In: *ACS Applied Electronic Materials* 1 (2019), pp. 407–416. ISSN: 2637-6113. DOI: 10.1021/acsaelm.8b00128.

Acronym Index

4D STEM four-dimensional scanning transmission electron microscopy 1, 24–27, 30–33, 35, 37, 42–44, 54, 67, 72, 75, 78, 80, 89, 92, 114, 115, 120, 121, 125, *Glossary: 4D STEM*

ACOM automated crystal orientation mapping 31

AFM atomic force microscopy 80

APS active pixel sensor 25, 30

CBED convergent beam electron diffraction 12, 27, 119

CCD charge-coupled device 30, 110

CNN convolutional neural network xvi, 125–128

CVT chemical vapor transport 40, 104, 107, 108

EDS energy dispersive X-ray spectroscopy 1, 12, 27, 37, 42–44, 47, 49, 67, 115, 120, 125, *Glossary: EDS*

EELS electron energy loss spectroscopy 12, 27, 43, 47

FCC face-centered cubic 4, 7, 50, 52, 54, 61, 83, 127

FFT fast Fourier transform 64, 91

FWHM full-width at half-maximum 42, 72, 99, 109, 127, *Glossary: FWHM*

GUI graphical user interface 31

HAADF high-angle annular dark field 1, 9, 12, 31, 37, 42–44, 46, 47, 49, 59, 60, 64, 67, 72, 80, 83, 89, 91, 94, 125, 129, *Glossary: HAADF*

NBED nanobeam electron diffraction xvi, 27, 54, 75, 126, 127, *Glossary*: NBED

PAD pixel array detector

PL photoluminescence spectroscopy 98

SAED selected area electron diffraction 27

STEM scanning transmission electron microscopy 8, 9, 24, 27, 30, 33–35, 37, 42–44, 46–50, 52, 59, 60, 64, 66, 67, 72, 75, 80, 83, 92, 94, 115, 116, 118, 120

STM scanning tunneling microscopy 47, 80

TEM transmission electron microscopy

Glossary

4D STEM Four-dimensional scanning transmission electron microscopy (4D STEM) is a method of recording a set of 2D diffraction patterns at each point over a 2D sample area, resulting in a “four-dimensional” dataset.

EDS Energy dispersive X-ray spectroscopy (EDS) is an analysis technique that uses characteristic x-rays emitted following inelastic electron scattering to identify the elements present in a sample. EDS is most accurate for heavier atoms, and cannot reliably detect low-atomic weight elements.

epilayer Shortened term for “epitaxial layer”, referring to a thin crystalline film grown on top of an existing substrate and adopting an energy-minimizing crystal orientation with respect to that substrate.

epitaxy Epitaxy describes a type of crystal growth or material deposition in which new crystalline layers adopt one or more well-defined orientations with respect to the crystalline substrate. The deposited crystalline film is called an epitaxial film or epitaxial layer.

FWHM The full-width at half-maximum of a signal peak is defined as the width, or diameter, of a distribution at 1/2 the maximum signal intensity. This shorthand is used for signals including EDS peaks, the line profile of electron beam cross-sections, and so on. In a normal distribution, the FWHM is related to the standard deviation, σ , via the following: $\text{FWHM} = 2\sqrt{2 \ln 2} \sigma$

HAADF High-angle annular dark field scanning transmission electron microscopy (HAADF-STEM) is a real-space TEM imaging technique that uses an annular dark-field (ADF) detector to detect electrons inelastically-scattered at higher angles, from about 50 mrad to about 200 mrad. Scattered electron counts (or signal) at a each probe position is integrated and displayed as pixel brightness.

NBED Nanobeam electron diffraction is a convergent beam electron diffraction technique using a very small convergence angle, such that the electron beam

is nearly parallel as it intersects the sample. The full-width half-maximum (FWHM) of the incident beam is on the order of 1 – 2 nm.